Development of sensitive fluorescent and spectroscopic assays to study tau assemblies implicated in neurodegenerative diseases

Dissertation
zur Erlangung des Grades
„Doktorin der Naturwissenschaften“
im Promotionsfach Chemie
am Fachbereich Chemie, Pharmazie,
Geographie und Geowissenschaften
der Johannes Gutenberg-Universität Mainz

Lacey Chunilal
geb. in Trinidad, WI

Mainz, 2023

1st Reviewer [redacted]
2nd Reviewer

Declaration of Authorship

I, Lacey Chunilal, declare that this thesis titled, “Development of sensitive fluorescent and spectroscopic assays to study tau assemblies implicated in neurodegenerative diseases” and the work presented in it are my own. I hereby certify, according to § 10 Abs. 3d of the doctoral regulations of 24.07.2007:, that:

- the submitted scientific work has not yet been submitted to any other German or foreign university or comparable institution for the purpose of obtaining an academic degree.
- I have not yet completed a doctorate or a comparable graduation procedure in the doctoral subject without success.
- I have not yet successfully completed a doctoral examination or a comparable graduation procedure in the subject of the doctorate.
- The scientific work has been written independently and only the indicated sources and aids have been used

Signed:

Date:

Abstract

Protein misfolding and fibrillization are core pathological hallmarks of neurodegenerative diseases. Abherrent forms of the tau protein are implicated in the pathology of diseases including Alzheimer's disease, Pick's disease, and Frontotemporal dementia; where it assembles into filamentous inclusions within cells in the form of neurofibrillary tangles. In the last twenty years, tauopathy research has had several pivotal findings, including the identification of the neurotoxic effects of the small oligomeric forms of the tau protein, the structural heterogeneity of fibrillar tau, and the capability of tau to form biomolecular condensates. These new insights have highlighted the need for more sensitive methods to characterize the early stages of the fibrillization process, observing initial protein conformational changes, and subsequent events.

The main aim of this work is to develop methods that report on processes implicated near the nucleation and elongation phases, by 1.) characterizing the liquid-liquid phase separation processes of the protein and 2.) developing affinity-based detection assays to provide kinetic data for the oligomerization process. In the first objective, intrinsic and extrinsic fluorescence-based methods are introduced as techniques to determine temperature-dependent phase transitions of proteins and labeled biomolecules. These methods allow low volume and low concentration measurements of LLPS as an alternative to absorbance turbidity measurements. Furthermore, supplementary methods of data analysis using dimension reduction techniques such as principal component analysis greatly improve the scope of the technique by allowing trends in high throughput screens to be easily identified.

The second part of this work focuses on the development of aptamer-based fluorescence spectral shift assays which quantify the change in the tau monomer concentration in solution. This assay is optimized to perform measurements at pathologically relevant concentrations to produce real-time information on the formation of small oligomers - a process missed by Thioflavin T assays. Finally, signal amplification is explored in the development of spectral shift in-solution plasmonic assays. The oligonucleotide - gold nanorod conjugates described in the work produce a highly sensitive detection tool, with improved signal-to-noise ratios. As such, each of the methods developed in this thesis aims to challenge the state of the art of biophysical characterization of the various assembly states of tau.

Zussamenfassung

Proteinfehlfaltung und Fibrillierung sind zentrale pathologische Merkmale neurodegenerativer Erkrankungen. Anomale Formen des Tau-Proteins sind an der Pathogenese von Krankheiten wie der Alzheimer-Krankheit, der Pick-Krankheit und der Frontotemporalen Demenz beteiligt. Bei all diesen Krankheiten bildet das Tau-Protein neurofibrilläre Knäuel, die sich zu fadenförmigen Einschlüssen in den Zellen ansammeln. In den letzten zwanzig Jahren hat die Tauopathie-Forschung mehrere entscheidende Erkenntnisse gewonnen, darunter die Identifizierung der neurotoxischen Wirkungen der kleinen oligomeren Formen des Tau-Proteins, die strukturelle Heterogenität von fibrillärem Tau-Protein und die Fähigkeit von Tau-Protein, biomolekulare Kondensate zu bilden. Diese neuen Erkenntnisse haben den Bedarf an empfindlicheren Methoden zur Charakterisierung der frühen Stadien des Fibrillierungsprozesses, zur Beobachtung der anfänglichen Konformationsänderungen des Proteins und der nachfolgenden Ereignisse deutlich gemacht.

Das Hauptziel dieser Arbeit ist die Entwicklung von Methoden, die Aufschluss über Prozesse im Bereich der Nukleations- und Elongationsphase geben. Dazu werden 1.) die Flüssig-Flüssig-Phasentrennungsprozesse des Proteins charakterisiert und 2.) Affinitätsbasierte Detektionsassays entwickelt, um kinetische Daten für den Oligomerisierungsprozess zu liefern. Für die Flüssig-Flüssig-Phasentrennung (engl. liquid-liquid phase separation, kurz LLPS) werden im ersten Teil der Arbeit Methoden zur Bestimmung temperaturabhängiger Phasenübergänge von Proteinen und markierten Biomolekülen vorgestellt, die auf intrinsischer und extrinsischer Fluoreszenz basieren. Diese Methoden ermöglichen Messungen von LLPS mit geringem Volumen und niedriger Konzentration als Alternative zu Absorptions- und Trübungsmessungen. Darüber hinaus wird der Anwendungsbereich der Technik durch ergänzende Methoden der Datenanalyse maßgeblich erweitert. So ermöglicht der Einsatz von Techniken zur Dimensionsreduktion wie z. B. der Hauptkomponentenanalyse eine einfache Identifizierung von Trends in Hochdurchsatz-Screens.

Der zweite Teil dieser Arbeit konzentriert sich auf die Entwicklung von Aptamer basierten Fluoreszenz-Spektralverschiebungstests, die die Veränderung der Tau Monomerkonzentration in Lösung quantifizieren. Dieser Assay wird so optimiert, dass Messungen bei pathologisch relevanten Konzentrationen durchgeführt werden können, um Echtzeitinformationen über die Bildung kleiner Oligomere zu erhalten - ein Prozess, der von Thioflavin-T-Assays nicht erfasst wird. Schließlich wird die Signalverstärkung bei der Entwicklung von plasmonischen Assays mit Spektralverschiebung in Lösung untersucht. Die in dieser Arbeit beschriebenen Oligonukleotid-Goldnanorod-Konjugate ergeben ein hochempfindliches Nachweisinstrument mit verbessertem Signal-Rausch-Verhältnis. Gemessen am aktuellen Stand der Technik, soll jede der in dieser Arbeit entwickelten Methoden eine Verbesserung für die biophysikalische Charakterisierung der verschiedenen Aggregatzustände des Tau-Proteins bringen.

Acknowledgements

The completion of this thesis would not be possible without the support of many people. Firstly, this project is funded by the EU Horizon 2020 research and innovation program under the Marie Skłodowska-Curie grant agreement no. 812868 as part of the Innovative Training Network - Chemical Reaction Networks (CReaNet). I thank all of my CReaNet colleagues for their collaboration in this multidisciplinary network. I would also like to thank both [redacted] and [redacted] for selecting me for this program, and the life-changing opportunities it has bestowed to me.

The majority of my work was conducted at NanoTemper Technologies, a place where I have made meaningful life-long connections. I would like to thank all of my colleagues including [redacted] and [redacted] for your support during my thesis writing. Your positivity and friendships kept me constantly motivated.

There are also several colleagues whose collaborations were imperative to the success of some of my projects. I want to thank [redacted] who contributed tremendous support in the development of the Principal Component Analysis analyses. I would also like to thank both [redacted] and [redacted] for their expertise providing in reviewing the data analysis chapter, to ensure its mathematical integrity. The work on spectral shift would not be possible without the developments and improvements made to Monolith by [redacted] [redacted], [redacted] also greatly assisted in the development of the automated spectral shift setup, and contributed to data analyses for kinetic measurements. I would also like to thank [redacted] and [redacted] for their feedback in the early stages of this project. At JGU, I want to thank [redacted] for the many hours she lent to me, to help establish the protocols for confocal microscopy.

For their guidance throughout this project, I would like to thank all of my project supervisors. Firstly, to [redacted] who helped establish the direction of the project, and provided excellent leadership of the research group. Secondly, [redacted], my main project advisor, not only provided academic support but also helped me develop my skills in presenting scientific data. Finally, thank you to [redacted] for your excellent feedback which helped improve the quality of my work. I have learned a great deal from all of you, which I will carry with me throughout the rest of my academic career.

And finally, I would like to thank my family for their support. I would not be able to achieve this great milestone without all of the many sacrifices made by my parents and siblings. [redacted] you are a constant inspiration to me. To [redacted], the hardest moments were made bearable by your tireless support. I dedicate this thesis to all of those who have held my hand throughout this challenging and rewarding journey.

Contents

List of Abbreviations

AD	Alzheimer′s Disease
ATPZ	Aminothienpyridazine
AuNR	Gold Nanorod
BSA	Bovine Serum Albumin
CD	Circular Dichroism
CSF	Cerebrospinal Fluid
CTAB	Cetyltrimethylammonium bromide
DLS	Dynamic Light Scattering
FRAP	Fluorescence Recovery After Photobleaching
GAG	Glycosaminoglycan
IFR	Intrinsic Fluorescence Ratio
LLPS	Liquid Liquid Phase Separation
LSPR	Localized Surface Plasmon Resonance
MST	Microscale Thermophoresis
MTBD	Microtubule Binding Domain
nanoDSF	Nano-Differential Scanning Fluorometry
ND	Neurodegenerative Disease
NFT	Neurofibrillary Tangles
PCA	Principal Component Analysis
PEG	Polyethylene glycol
PHF	Paired Helical Filaments
SpS	Spectral Shift
TRIC	Temperature Related Intensity Change
dsDNA	Double Stranded DNA
ssDNA	Single Stranded DNA

Dedicated to my family.

Chapter 1

Introduction

1.1 Protein Misfolding in Neurodegenerative Diseases.

The occurrence of protein misfolding and aggregation has served as a pathological hallmark for several neurodegenerative diseases (ND). Misfolded protein aggregates form highly ordered fibrillar structures and accumulate as intra- or extra-neuronal inclusions in diseases such as Alzheimer's disease, Parkinson's disease, amyotrophic lateral sclerosis, Huntington's disease, frontotemporal dementia, and chronic traumatic encephalopathy [1]. These diseases account for more than 55 million cases of dementia occurring worldwide, as of 2022. The economic cost of patient care, treatment, and related societal burdens has been estimated to be over 320 billion dollars per year, with the socioeconomic impact of neurodegenerative diseases being projected to increase over the next decade, driving the need for further research into therapies for these cases [2].

The functional landscape of these proteinopathies is complex, sometimes with more than one protein family identified in the disease. For example, proteins such as tau, amyloid beta, alpha-synuclein, and fused in sarcoma (FUS) can be present in multiple neurodegenerative diseases, often with crosstalk and associations with one protein and another [3, 4]. For example, the aggregation of tau and amyloid beta present in the pathogenesis of Alzheimer's disease, with associations between tau and amyloid beta protein widely documented, in the form of interactions with potential cross-seeding mechanisms [5–8].

Tau is a protein that aids in the regulation of the dynamic stability of the microtubules. However, this typically soluble protein, in its pathogenesis, is detached from the surface of the microtubule and undergoes a transition to insoluble fibrils (Fig. 1.1). The assembly of tau into filamentous inclusions can proceed through pathologically specific pathways, either into straight, or paired helical filaments (PHFs), and occur as intracellular deposits [9]. These fibrillar proteins become the main components of neurofibrillary tangles (NFTs), a major pathological hallmark of a class of neurodegenerative diseases called tauopathies. These diseases include Alzheimer's disease [10], Pick's disease [11], frontotemporal dementia [12], and chronic traumatic encephalopathy [13]. These pathologies highlight the relevance of studying and developing therapeutic strategies for each of the proteins that distinguish a certain kind of pathology. ND research is centered on two main areas: exploring the mechanism underlying the fibrillization behavior of the protein in question and therapeutic strategies to mitigate the deleterious cognitive effects associated with disease.

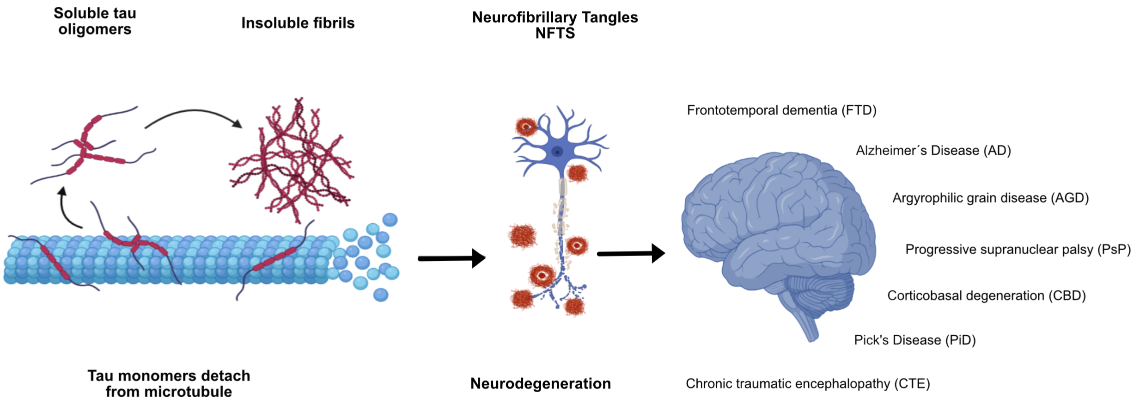

Figure 1.1: Tau undergoes a process in which it transitions from a soluble monomer to oligomeric forms that mature into insoluble fibrils. Tau filamentous inclusions are the main component of NFTs found as intracellular deposits which lead to neurodegeneration.

During the past 20 years, several pivotal advances have shaped the direction of tauopathy research. The first was experimental evidence that soluble oligomeric protein species such as tau and amyloid beta are responsible for neurotoxicity and neuronal degradation [14, 15]. This information was crucial as many therapeutic approaches aim to destabilize or degrade mature neurofibrillary tangles and amyloid plaques. The need for strategies targeting small oligomers provided entirely new urgency in elucidating the early fibrillization mechanisms for tauopathies. The second advancement was the availability of higher resolution structural techniques such as cryo-electron microscopy to study fibrillar structures [16]. This has revealed a great deal of heterogeneity in the morphology of tau fibrils, which correlates with the different pathologies. This has led to a greater focus on the complexity of the molecular structures of the various proteins involved in the pathology. As a result, therapeutic approaches now consider the impact of conformational heterogeneity on drug efficacy and specificity. The recent discovery that several proteins, such as tau, FUS, and α -synuclein, involved in neurodegenerative diseases are capable of liquid-liquid phase separation has led to a newly proposed mechanism for protein aggregation [17]. Here a key question is, could much higher concentrations within a droplet phase promote protein self-association and provide a pathway for oligomerization?

Given recent advances in tauopathy research, there is a need for high-resolution biophysical techniques capable of reporting on the early stages of the fibrillization mechanism. Methods that provide insight into protein conformational changes, oligomerization state, aggregation initiation mechanisms, and screening inhibitors are necessary to provide an effective therapeutic paradigm. Characterization of the tau protein has proven difficult because it adopts a variety of conformations, not only in fibril form but also in its monomeric, intrinsically disordered state. Therefore, the high-resolution structural information that can be obtained for such a protein is limited, so nonstructural biophysical methods that report on its interaction and oligomerization behavior serve as a valuable window for discovering important, pathologically relevant information.

1.2 The structures of tau

Tau is classified as an intrinsically disordered protein (IDP); which can undergo an ordered assembly to form highly structured filaments. The amino acid sequence of tau informs its primary and secondary structure and the role of its structure in its pathogenesis.

1.2.1 The primary amino acid sequence and post-translational modification of tau

The tau protein is encoded by the MAPT gene [18], which produces six different isoforms that range in length from 352 to 441 residues. The overall sequence of the protein can be divided into four major regions: The N-terminal projection domain, the proline-rich domain, the microtubule-binding region, and the C-terminal domain as seen in Fig. 1.2. The isoforms can be classified by the number of insertions near the N- terminal (0N, 1N, or 2N) and by the number of repeats in the microtubule-binding region (MTBR) with three or four domains (3R or 4R) consisting of 31 and 32 residues.

The tau sequence is defined as low complexity, as it is composed of only a limited and unbalanced number of the 20 possible amino acids [19]. For example, the MTBR is a low-complexity domain, containing two hexapeptide motifs designated PHF6* (275VQIINK280) and PHF6 (306VQIVYK311). These motifs, in the second and third repeats of the MTBR, form the core of the paired helical filaments and are imperative for the aggregation properties of the protein. Tau isoforms that do not include them show no propensity for fibrillization [20]. The local repetitive nature of the amino acid composition in the main domains of full-length tau results in charge segregation with modular charged units. Tau has negatively charged domains near the N and C terminals and positively charged domains in the proline-rich and MTBR. This charge separation has a great impact on the structure and dynamics of tau, possibly allowing transient short-range interactions [21].

The amino acid sequence determines the degree of post-translation modifications that can alter the behavior of the protein. Within tau, there is the potential for several abnormal modifications that greatly alter its structural and functional properties. The main component of NFTs is hyperphosphorylated tau, but it is not certain if it may just be a consequence of pathology, as no causal relationship has yet been established between phosphorylation and filament formation. Phosphorylation is the addition of a phosphoryl group to a hydroxyl group of the polar groups of serine, threonine, or tyrosine [23]. With 45 serine residues, 35 threonine residues, and 5 tyrosine residues, tau has 85 possible phosphorylation sites [24]. Phosphorylation results in a change in the electrostatic properties of the protein by the introduction of the negatively charged hydrophilic group, which also alters the conformation of the protein. Since the MTBR has 20 phosphorylatable sites, the corresponding electrostatic and conformational changes upon modification

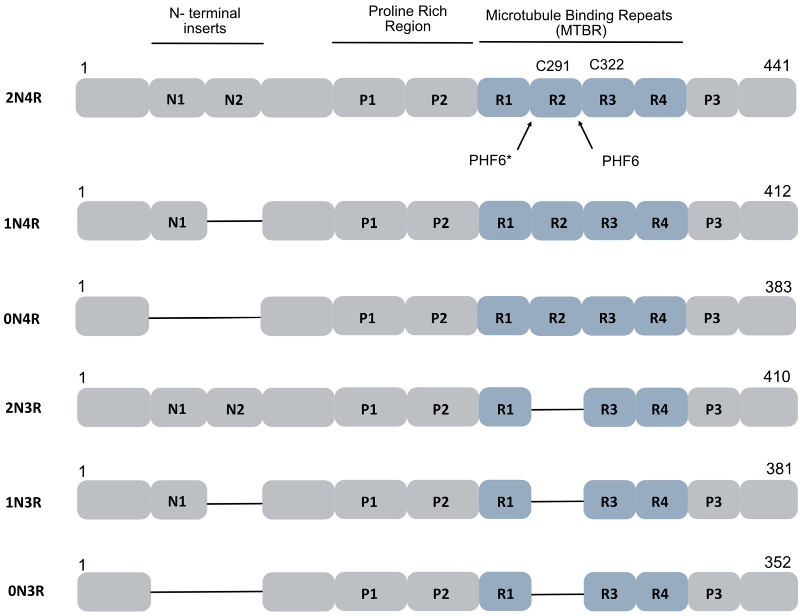

Figure 1.2: Amino acid composition of tau, showing each of the six possible isoforms. Adapted from [22]. The sequence was obtained with UNIPROT Accession Number: P10636.

result in reduced binding affinity of negatively charged microtubes that leads to detachment [25].

In addition to phosphorylation, tau is also subject to both methylation and acetylation at lysine residues, of which 20 are capable of being modified. While this action changes the overall charge of the protein by neutralizing positively charged lysines, it may also play a secondary role in the promotion of aggregation through the impairment of the binding of tau to microtubules and through the competition for ubiquitination sites for the triggered degradation of unbound tau [26, 27]. Several studies have shown acetylated tau present in human and mouse tauopathies, and recent studies also show the appearance of methylated tau in patients with Alzheimer's disease [28, 29].

In addition, elevated levels of glycosylated tau have previously been reported in the brains of AD patients [30, 31]. Glycosylation refers to the covalent attachment of oligosaccharides to a protein, whereas the non-enzymatic process, glycation, is the reaction between a carbohydrate and a lysine of a protein [32]. Although there is no exact causative mechanism between glycosylation/glycation and aggregation, some suggest that glycated lysines may not be as easily degraded and promote tau accumulation [33].

Finally, the role of ubiquitination in tau aggregation has been highly debated, with divergent opinions on the presence of ubiquitinated tau in PHFs [34, 35]. While covalent modification of lysine residues is very common, 17 of the 44 lysine residues have been shown to be sites of ubiquitination in patients with AD [36]. Although some propose that ubiquitination is a response to tau accumulation and occurs after phosphorylation [37], others have even proposed that it promotes the formation of solid aggregates. As such, the interaction between each post-translational modification is complex and widely studied [38, 39].

1.2.2 Secondary and tertiary structure

As tau is an intrinsically disordered protein, it does not retain a fixed tertiary conformation in solution. Evidence from several biophysical methods such as circular dichroism (CD) [40], NMR [41], and small-angle X-ray scattering (SAXS) [42] shows that tau exists as a flexible and mobile polymer with a small amount of transient secondary structures. However, despite the lack of local order, tau preferentially adopts a global fold in the form of a "paperclip" conformation in which opposite termini fold toward each other [43].

Early characterization of tau secondary structures using circular dichroism showed that tau exists in a largely unstructured state, displaying the characteristic spectra of a random coil [40]. In this study, the existence of some degree of secondary structure was proposed with CD showing hints of the minimal α-helix structure.

Small angle X-ray diffraction provided evidence that α-helix structures existed alongside β-sheets [41, 42], but the most definitive studies were performed by Mukrasch *et al.* with solution-state NMR, which further elucidated the location and populations of these transient structures [44, 45].

This study provided information on the location and populations of transient secondary structures. It was confirmed that tau exists as a highly dynamic, flexible protein with 343 of the 441 amino acids being disordered, as shown in Fig. 1.3 **a)**, where grey lines are disordered, the red arrows are β-sheets, and the blue blocks α-helix structures. The highest β structure content was found for residues 274KVQIINKKLDL284 and 305SVQIVYKPVDL-315 in repeats R2 and R3, comprising the two aggregation-prone hexapeptides 275VQI-INK280 and 306VQIVYK311. The presence of these β sheet conformations is transient, resulting in only temporary secondary structure, since the β-sheets exist only 22 % of the time in the R2 region and 25 % of the time in the R3 region. The α-helices were found to be predominantly in residues 114-123 and 428-437, near the N and C-termini, respectively, with a 12 % likelihood. Spin relaxation rates and residual coupling measurements also reflect the flexibility of the backbone of the protein, which is highest in the C-terminal, with the proline-rich domain and MTBR showing slightly higher rigidity.

Small angle x-ray measurements performed by Mylonas *et al.* confirmed NMR results showing a similar radius of gyration, more akin to β-strands than α-helix structures, and that the propensity for β-strand formation was exclusively in the microtubule-binding domain [14]. The residual structure that appears in the MTBR in tau has been proposed to lead to the eventual β-sheet-rich structures in the PHFs as is discussed in Section 1.3. The average radius of gyration of the ensemble of calculated structures was approximately 65 Å, in agreement with the average value obtained for tau 2N4R from NMR [44]. Furthermore, experiments with FRET and electron paramagnetic resonance by Jeganathan *et al.* showed that tau exhibits a conformation that brings the N-terminal closer to the C-terminal, and the C-terminal and the repeat domain closer as shown in Figure 1.3b [43]. This data revealed that global folding was present in combination with the flexibility of chains. The average radius of gyration measured by FRET is around 5 nm, which is in agreement with the SAXS and NMR data [46]. The global fold was proposed

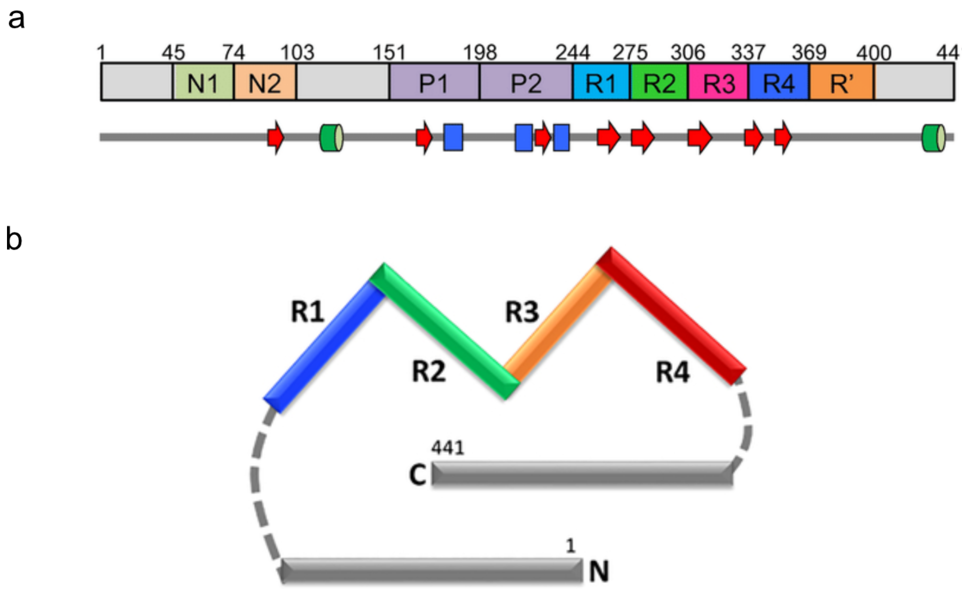

Figure 1.3: a) Transient secondary structure elements in 2N4R tau identified from NMR characterization: β-structure (red arrow), α-helical (green cylinder), polyproline II (blue rectangle), adapted from Mukrasch *et al.* 2009 **b)** The proposed global paperclip fold of full-length tau 2N4R, adapted with permission from ref. [43].

to be a paperclip or hairpin fold, which tau adopts as its preferred state in solution. This conformation differs from a fully extended conformation, which is necessary for microtubule interactions, and it is proposed that this structure may inhibit tau self-association, increasing its stability [47].

The transient secondary structures observed for monomeric tau in solution have provided insight into how tau transitions into small oligomeric structures and highly structured filaments. Following the paradigm that tau in solution adopts a thermodynamically stable state in the form of a paperclip fold, further studies have explored the origins of filament formation via a larger population shift from this state to an extended aggregation conformation as seen in PHFs [48]. This early misfolded intermediate was proposed to be the result of a population shift to the extended solution state, which marks the beginning of the fibril formation process that precedes the monomer to the dimer transition [49].

1.3 Polymeric assemblies of tau

1.3.1 Oligomerization of tau

As oligomeric tau has been identified as the major neurotoxic species, and not the long filamentous tau found in NFT, more attention has been placed on early oligomer formation [50]. Several oligomeric forms of tau have been shown to have neurotoxic effects, ranging from trimers [51], smaller soluble aggregates ranging from 200-300 kDa, and granular oligomers composed of high molecular weight multimers [15]. Several animal models have so far demonstrated that deleterious effects, such as memory loss and neuronal degradation, are correlated with the presence of small oligomers of tau, even in the absence of insoluble filamentous tau [52] [53]. Therefore, a therapeutic strategy for the suppression of filamentous tau does not improve cognitive activity, Wittmann *et al.*, reporting that NFT accumulation alone cannot fully account for neuronal death [54]. In fact, cognitive decline was shown to precede the emergence of NFT pathology in mouse models [55]. Further investigation into tau oligomers concentrations in cerebrospinal fluid (CSF) and brain samples from AD patients in humans was higher than in control samples of persons not afflicted with NDs [47, 56].

The oligomerization of tau into short flexible fibrils (protofibrils), and then further into mature fibrillar structures, has long been considered to occur in a nucleation-dependent polymerization process [57] that comprises a lag phase where nucleation occurs, an elongation phase, and saturation phase (Fig. 1.4) [58]. The polymerization process is typically governed by rate constants for nucleation and elongation, a simplified approach that can be broadened to consider off-pathway (non-aggregation-prone) species and secondary interactions such as fragmentation and annealing, as was described by Ramachandran *et. al.* [59].

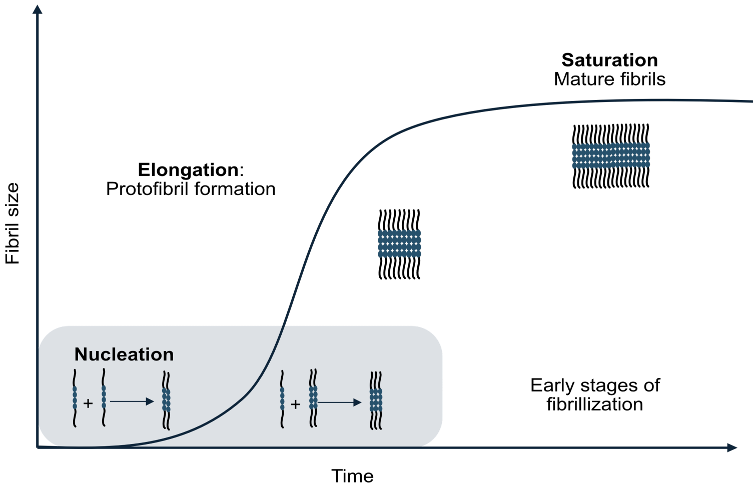

Figure 1.4: A time-course of the typical stages of tau oligomerization, starting with the formation of a nucleation competent monomer, followed by an elongation and saturation phase.

Potential mechanisms of tau oligomerization

The early work of Friedhoff and coworkers in 1998 attributed dimers as the necessary nucleation points upon which further monomer addition can occur [57]. Several studies have since tried to propose mechanisms by which this nucleation site capable of aggregation can be created [41, 60]. The formation of the tau-tau dimer has been largely thought to happen through MTBR-mediated interactions. However, the type of interactions that occur varies greatly depending on which tau-isoform is considered. For instance, it has been proposed that intermolecular disulfide bonds between cysteines of different tau molecules allow the formation of a covalently linked tau dimer. Barghorn and co-workers indicated that although isoforms that contain only one cysteine (3R isoforms) are likely to form intermolecular linkages, isoforms such as full-length tau (2N4R) which contain two cysteines and thus also have the propensity for intramolecular disulfide bonds, by which they can dimerize. Fibrillization under reducing conditions was seen to slow oligomerization rates for 3R isoforms, and promoted under oxidizing conditions [41]. However, it was also observed that the 2N4R isoform fibrillizes under oxidizing and reducing conditions in the presence of an inducer. Barghorn proposed a noncovalent dimerization between isoforms, possibly mediated by the MTBR region [41]. Several further studies had similar conclusions, which demonstrated that fibrillization can occur in both a cysteine-dependent and independent manner [61, 62]. Sahara *et al.* isolated non-covalent dimers for a cysteine-free variant of full-length 2N4R, while Al-Hilaly *et al.* demonstrated that dGAE fragments (291-391) actually exhibited enhanced fibril growth not only under reducing conditions but also with mutants without cysteines [61]. Therefore, it is evident that there are several fibrillization pathways mediated by both covalent and non-covalent interactions in the MTBR. Whilst these non-covalent mechanisms are still unknown, several have been proposed. Rosenberg *et al.* proposed that dimerization can proceed via electrostatic interaction of the positively charged MTBR of the protein with its N-terminal domain[63], while Feinstein *et al.*, proposed a mechanism of dimerization via an electrostatic zipper, which forms between two N-terminal tails of the protein aligned in an antiparallel manner [64].

Regardless of the role of cysteines in dimerization, groups such as Kuret *et al.* have proposed that dimerization itself may not be the rate-limiting step in the formation of higher-order oligomers. Kuret *et. al* instead proposed that the formation of a soluble aggregation-competent monomer, in the form of a partially unfolded intermediate in an extended conformation, triggers the fibrillization process [65].

An alternative pathway for fibrillization is via inducer molecules, usually polyanionic cofactors. Justification for the use of polyanions such as heparin, RNA, or arachidonic acid was the presence of cofactors in neurofibrillary tangles in patients with AD, originally reported by Goedert in 1996 [12], which provided physiological relevance. The mechanisms behind cofactor-induced aggregation will be discussed in more detail in Section 1.5.1.

1.3.2 The formation of tau filaments

The pathological hallmark of several neurodegenerative diseases is the presence of intracellular neurofibrillary tangles composed of tau filaments [66]. Recently, the structure of these NFTs has been explored. Structural studies of tau NFTs generally use tau filamentous inclusions derived from the brain of Alzheimer's patients as performed by Goedert *et al.* [16]. Recently, the Goedert, Scheres, and Fitzpatrick laboratories began a large-scale study aimed at characterizing several proteins, including tau, in a variety of pathological conditions, using cryo-electron microscopy (CryoEM) [16, 66, 67]. This study provided high-resolution structures of filaments from which a structure-based classification system for tauopathies is being developed. It was shown that different neurodegenerative diseases had distinct tau isoform compositions and morphologies.

The tau lesions in Alzheimer's disease are comprised of straight or paired helical filaments (SFs or PHFs) which have been termed 'ultrastructural polymorphs' of each other,

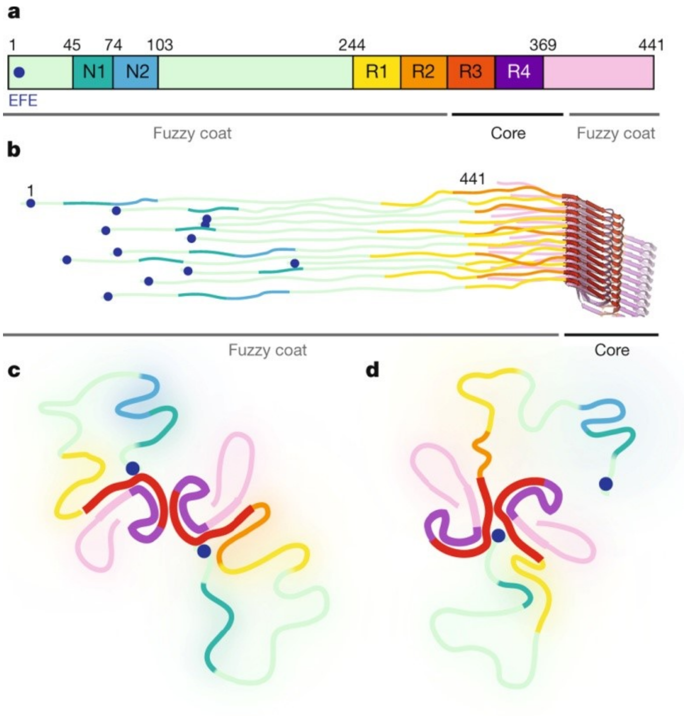

Figure 1.5: **a)-b)** shows the amino acid sequence of tau and the structure of paired helical filaments. **c)** Straight and **d)** Paired helical fragments are shown to be ultrastructural polymorphs. Reproduced with permission from ref. [66].

as both polymorphs have a core made of two C-shaped filaments but differ in the location of the interfaces (Fig.1.5 **c) - d)**). This confirmed the previously held view that SFs and PHFs shared a common structural unit [68]. The filamentous core serves as a seeding-competent nucleus for the formation of longer fibrillar structures. The core of the filament lies between residues 306-378, in the MTBR, which forms cross-β / β- helix structures that line the length of the filament, while the unstructured C and N-termini are described as a fuzzy coat protruding from the core (Fig. 1.5 **b)**) [69].

Fig. 1.5 **c) - d)** shows the simplified morphology for tau PHFs and SFs seen in Alzheimer's disease, derived from CryoEM performed by the Goedert group. However, the morphology of filaments seen in Pick's disease, chronic traumatic encephalopathy, corticobasal degeneration, and progressive supranuclear palsy all differ with respect to the topology of folds, the shape of the core, and the number and type of isoforms present in each disease. With a structural understanding of the topology of the filament, fibril studies performed *in vitro* can be compared with clinically derived fibrils. Since the mechanism by which different cofactors induce fibrillization is unknown, several studies have focused on determining if and where the cofactors colocalize on filaments, and the corresponding conformal changes that this may cause prior to fibril assembly [70]. Studies conducted by Fichou *et al.* showed that heparin-induced tau fibrils are conformationally different from the paired helical filaments found in patient-derived NFTs [71]. Zhang showed that tau fibrils appeared to be coated with heparin and was suggested to play a stabilizing role [72].

It is also important to note the limitations of the CryoEM-derived structures, which up to recently have only allowed a small number of patient-derived samples to be studied. Furthermore, fibrils must undergo a significant amount of purification steps and the imaged filaments are those that are necessarily insoluble in detergents [73]. Thus, it is important to be critical of all structural information reported, whether from *in vivo* or *in vitro* derived fibrils.

1.3.3 Tau Condensates

Tau is among the proteins identified as capable of liquid-liquid phase separation (LLPS). This process involves the separation of a biomolecule in a dense aqueous phase, with a distinct phase boundary from its surrounding solution. Phase separation has been observed extensively in eukaryotic systems, with membraneless organelles serving a variety of cellular functions. However, aberrant phase separation of IDPs involved in neurodegenerative diseases has led to research to elucidate the pathological relevance of the process.

LLPS is governed by the presence of a variety of multivalent interactions, which promote the self-association of molecules, rather than interaction with the solvating medium. LLPS of intrinsically disordered proteins can be driven by a variety of different interactions, ranging from electrostatic charge-charge interactions to hydrophobic interactions. LLPS is seen as a mechanism that allows tau to increase its availability to participate in multiple forms of transient intermolecular interactions, because of its flexible and heterogeneously charged monomeric form [74]. However, phase separation of tau can occur by self-association or by the interaction of tau with highly charged anionic cofactors such as RNA, DNA, or heparin.

Several studies are thus dedicated to investigating the type and strengths of interactions that are responsible for different LLPS systems [75]. For example, Bokyo *et al.*, demonstrated that although hydrophobic interactions may be a major contributor to coacervates formed by heterogeneous nuclear RNA (hnRNA) and TDP-43, electrostatic interactions are more dominant in tau systems in low salt systems. This was shown by the addition of 1,6-hexanediol, which disrupts hydrophobic interactions, dissolving droplets that depend on these forces [76]. However, the compound was only seen to affect tau under high salt conditions where hydrophobic forces were dominant [75].

The implication of phase separation in neurodegenerative diseases is now being explored at several levels. The key question is the relationship between the structure of tau within the droplet phase and its subsequent aggregated conformation. Recent work by Wen *et al.* showed that there is indeed a transition into an extended conformation after droplet formation, which lends itself to defining a new paradigm that describes the formation of a tau conformation prone to aggregation as the defining step of pathogenesis [77]. However, Zhang *et al.* have shown that though there is a shift in tau population to an extended form in the condensed phase, there is no evidence that this serves as a precursor to PHFs, nor that it is a seeding-competent conformation [78]. There have also been studies that have indicated an increase in the β-sheet species in the droplet phase, as shown by ThT assays. However, not all coacervating conditions coincide with an increase in β-sheet structures and subsequent aggregation of tau. Several studies have instead indicated that, although tau droplet formation and aggregation may occur under concurrent conditions, there is not enough evidence to define a cause-effect relationship between the two [79]. Lin *et al.* showed that there is a clear cause-effect relationship between LLPS and tau aggregation, but only when LLPS is driven by hydrophobic association, with electrostatically driven processes that only overlap with aggregation when a cofactor is used [79].

Although there is a debate in the literature as to whether the formation of condensates directly leads to the aggregation of tau, it is undeniable that the increased intracellular concentration within the condensates will promote tau-tau association. This concentration mediating effect of LLPS is less clear and is the main factor driving more studies to clarify the role of LLPS in tau other tau assembly systems.

1.4 Biochemical and biophysical methods for characterization of tau.

The aim of the work presented in this thesis is to advance the state-of-the-art biophysical characterization of tau. The methods currently used to measure the interactions and biochemical properties of tau in all of its assembly states require precision to allow a full mechanistic understanding of fibrillization.

1.4.1 Methods to study tau interactions

Within the area of biophysical characterization in neurodegenerative disease research, methods that identify and measure interactions between proteins and interaction partners (either proteins or small molecules) must be able to detect high-affinity interactions (e.g. nanomolar K_d) and preferably in a high-throughput manner. As such, most studies have relied on Isothermal Calorimetry (ITC) and surface plasmon resonance (SPR), since these methods produce either in-solution measurements of affinity in the case of ITC or a platform for efficient screening of compounds in the case of SPR.

ITC has been used to characterize protein-protein and protein-ligand interactions. The method relies on measuring the heat absorbed or released upon binding of a target to a ligand. The approach involves the incremental injection of one binding partner into a calorimetric cell containing the other, typically at high micromolar concentrations, to detect a measurable amount of heat upon binding [80]. Evaluation of both the interaction affinity (K_d) and thermodynamic parameters, such as the change in enthalpy (ΔH) and entropy (ΔS) can then be performed by analyzing the reaction heat as a function of reagent concentration [81].

ITC has been used to measure the binding of small ionic inducers to tau such as Zn^{2+} Al^{2+}, Mg^{2+}, Fe^{2+} and Cu^{2+} [82, 83]. While the technique can provide interaction parameters such as the dissociation constant and thermodynamic information on the interaction, it requires a high volume of sample, in addition to its concentration requirements. Furthermore, when probing inducer interactions with tau, the data are convoluted with subsequent fibrillization [84]. Inducer interactions result in a time-dependent increased aggregation of the protein, and it can be difficult to distinguish between the thermodynamics of aggregation and the binary interaction. This is a major caveat that limits the accuracy of the technique, as it also does not allow accurate thermodynamic measurements.

Surface Plasmon Resonance is a technique widely used to screen possible inhibitors of the aggregation process. SPR is an optical technique that relies on the change in the refractive index of a thin gold biosensor platform upon binding of the ligand [85]. Typically, a protein is immobilized onto the metal surface within a flow cell through which the interaction partner or analyte is then injected. The binding of the ligand to the target results in a change of mass, and the corresponding change in the refractive index is quantified as resonance units. The change in resonance units over the association, equilibrium, and dissociation phases can then be used to quantify the strength of the binding interaction. However, the need for immobilization of the protein presents a unique problem for studying IDPS. Typically, a folded protein is expected to maintain the rigidity of its tertiary folded state upon immobilization, however, the unfolded dynamic state of an IDP is instead disrupted. As such, the conformation the protein must adopt upon immobilization may not necessarily be physiologically relevant or ideal for its interaction partner [86]. This can also lead to artifacts in the measurement, which can only be distinguished by checking with orthogonal techniques. This is seen in a study by Dunning *et al.*, where surface plasmon resonance produced an overestimated value for the dissociation constant for the binding between β42 and a glycogen synthase kinase GSK3α [87]. This highlights the advantage of in-solution methods for interaction analysis, especially in the case of high-affinity interactions. SPR measurements also have the caveat that signals vary with pH, ionic strength, and conformation of the immobilized protein [88, 89].

With the limitations presented by ITC and SPR, there is a need for biophysical methods that allow for high-throughput, real-time characterization of proteins interactions at pathologically relevant concentrations, which has been addressed with several studies using microscale thermophoresis (MST) and temperature-related intensity changes (TRIC). Microscale thermophoresis is a fluorescence-based method to characterize the strength of biomolecular interactions. In order to perform a measurement between a ligand and target, the intrinsic fluorescence of the tryptophan and tyrosine residues within the target molecule is measured, or it is labeled with an extrinsic temperature-sensitive fluorophore [90]. The target is titrated against a dilution series of the ligand and then loaded into a series of capillaries. The capillaries are placed on a temperature-controlled stage, within the device, after which an Infrared (IR) laser is used to locally heat a small volume within the capillaries. This introduces a thermal gradient, along which molecules migrate. The extent to which a target molecule moves across the thermal gradient depends on whether it is bound or unbound. The fluorescence of the target is detected before and after the IR laser is turned on, and a fluorescence signal called an MST trace is measured. An MST signal is comprised of two main components, the first of which is due to thermophoresis of bound and unbound target molecules moving along a thermal gradient, and the second being due to temperature-related intensity changes (TRIC), which are dependent on the chemical microenvironment of the fluorophore. The measured fluorescence can be used to produce a dose-response curve that can be used to determine the dissociation constant of the binding interaction.

The first study demonstrating ligand binding to amyloid-fibrils using MST was carried out by Wolff *et al.*, showing the potential to measure the interactions of fibrillar species with an in-solution method. The study showed the viability of a compound derived from green tea extract to bind monomeric and oligomeric α-synuclein [91]. MST was also used to characterize the interaction of methylene blue with tau [92]. Here Kiss *et al.* looked at the effects of methylene blue on various labeled tau isoforms, and later Vagrys used a label-free system to look at the interaction of the compound with K18 fragments [86]. MST was also recently used for the detection of small molecule binders to α - synuclein and tau fibrils, reporting that the technique was sensitive to different fibril lengths and morphologies, which other fluorescence-based techniques, such as ThT competition assays, could not discern [93]. This inspired a wide range of fibril inhibition studies, leading to the discovery of several new inhibitors, such as dual binders for tau and α - synuclein, by compound MG-2119 which hinders the fibril formation process [94], or PDD005 by inhibition also reduces neuro-inflammation [95].

1.4.2 Methods to study larger tau assemblies

For many amyloid-forming proteins, the state-of-the-art for measuring the kinetics of the process uses fluorescent dyes such as Thioflavin T (ThT), Thioflavin S (ThS), or Congo Red, which bind to β - sheet structures [96]. Thioflavin T is a benzothiazole-based dye (Fig. 1.6 **a)** which exhibits enhanced fluorescence upon binding to amyloid structures; the dye binds to tau across the beta-sheet structures (Fig. 1.6 **c)**). Upon excitation at 450 nm, the emission maximum blueshifts from 510 nm to 480 nm (Fig. 1.6 **b)**).

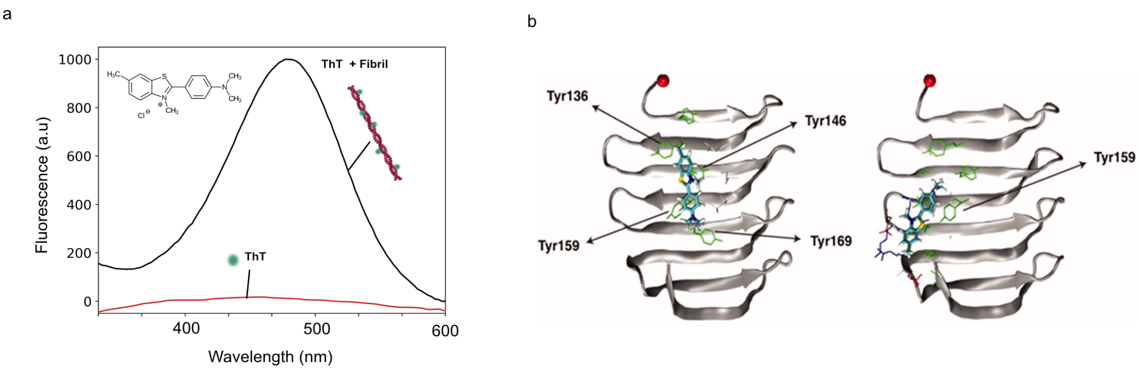

Figure 1.6: a) Structure and **b)** emission structure of Thioflavin T dye. Adapted from Malmos et. al [96]

A significant limitation to these methods is that these dyes bind strongly only to mature fibrils, allowing little to no insight into the formation of initial oligomeric structures. Smaller initial oligomeric structures have been shown to not strongly bind to ThT or Congo Red, despite their rich β-sheet content [97]. A popular alternative dye, bis-ANS dye, can bind to such oligomeric structures, but this dye works by binding to hydrophobic patches and can only indicate more surface exposure of hydrophobic groups for oligomers compared to monomers [98].

Fluorescence assays utilizing Thioflavin S and T have been used to detect both inducers and inhibitors of tau fibrilization. The increase in fluorescence emission indicates either an increased propensity for aggregation, but the caveat in using such methods to perform medium-throughput screening assays is that these methods do not provide a signal for early events in the aggregation mechanism, e.g. protofibril formation, which is a key target for therapeutic approaches. Furthermore, the reproducibility of ThT and ThS assays is often questioned, and it is not a quantitative technique [96]. False positives can also be a limitation for such a technique since compounds that auto fluoresce near the ThT or ThS emissions maximum must be excluded. This limits any fluorescence technique that only uses a small wavelength range in a high-throughput assay [99]. Fluorescence-based assays, such as ThT, that do not incorporate specific labeling techniques must consider that another molecule can displace the fluorescence indicator. The loss of signal due to detachment and not through decreased presence of amyloid structures cannot be inferred by this indirect method of analysis.

Sedimentation assays are frequently used to monitor and segregate larger aggregates from smaller species [100]. Typically, this method requires end-point measurements along the fibrillization pathway, in which the sample is centrifuged and aggregated species are collected and analyzed using an SDS-PAGE. Again this method suffers from not providing fully quantitative reaction kinetics, lack of identification of oligomeric species, and differentiation of amorphous from filamentous aggregates. Samples are also typically at high micromolar concentrations of tau, losing the ability to monitor concentration-dependent behavior under different conditions [101].

To avoid issues related to extrinsic fluorescence techniques and specifically examine the early formation of fibrils, tryptophan, and tyrosine fluorescence assays have been used to study various amyloid-forming proteins such as α-synuclein, amyloid-β, and tau [102]. The fluorescence of each of these amino acids is easily detectable, with emission spectra being sensitive to its local chemical environment. As such, conformational changes in the protein that may occur during the fibrillization process can be monitored as a function of its intrinsic fluorescence [103]. Several studies including Dusa *et al.* [104] and van Rooijen [105] have introduced tryptophan at sequence-specific sites to monitor oligomer formation and growth, since none of the aforementioned IDPs have intrinsic tryptophans. Only a few studies have relied solely on tyrosine spectral measurements over time, allowing proteins to be studied in their native state through the fibril-forming pathway [106]. A major limitation in these studies is the use of high micromolar concentrations for detectable signals, often requiring a large sample volume. There is significant potential in improving the sensitivity of this technique, especially when looking at intrinsically disordered proteins such as tau.

The idea of monitoring the intrinsic fluorescence of a protein for determining conformational changes holds great promise for measuring parameters for smaller tau assemblies, for example in the case of liquid-liquid phase separation. The current state of the art in detecting bulk droplet formation *in vitro* is to determine cloud point temperatures using absorbance measurements as a proxy for light scattering [17]. This reveals macroscopic changes in the turbidity of the sample at a transition temperature at which phase separation occurs. This method is usually supplemented with fluorescence imaging of phase-separated coacervates.

1.5 Inducer and inhibitor interactions with tau

1.5.1 Inducing tau fibrillization

Inducing fibrillization of tau *in vitro* has often been achieved using highly charged polyanionic cofactors, fatty acids, coordinated metal complexes, or through seeded aggregation by the addition of aggregation-competent oligomers. While the mechanism that promotes fibrillization may differ from inducer to inducer, the relevance of each method of inducing aggregation has been widely researched.

One of the most used polyanionic cofactors is heparin, a glycosaminoglycan (GAG) similar to heparan sulfate, which are negatively charged polysaccharide chains and a component of the extracellular matrix [107]. However, many studies have identified the presence of GAGs to be present not only in neurofibrillary tangles in tauopathies [12, 108] but also in amyloid deposits of other proteins [107] and was shown by [12] to induce fibrillization of amyloid-forming proteins. However, studies indicate that the heterogeneous nature of heparin-induced fibrils is different from those found in the brains of ND patients [71, 72]. This has called into question its use in fibrillation studies, but it is still widely used due to its ease of implementation for both *in vitro* and *in vivo* measurements.

The interaction between tau and heparin has been proposed to be largely mediated by electrostatic interaction with sulfate groups, and not through short-range Van der Waals or strong covalent interactions [65]. Charge neutralization of tau lysines and histidines by heparin was proposed to facilitate the formation of stacked MTBR units, as seen in Fig. 1.7 **a)**. Another mechanism of heparin was presented in a study by Ramachandran *et al.* who proposed that heparin is involved primarily in the nucleation step in the formation of heparin-bridged tau dimers. [109]. Although the incorporation of heparin into the fibrils of tau has been widely debated, there have also been several studies that instead monitor the conformational changes that occur upon the addition of heparin to tau in solution. Double electron-electron resonance measurements of PHF6 and PHF6* revealed that tau undergoes a transition to a more extended form within minutes of the addition of heparin (Fig. 1.7 **b)**). The distances recorded by this measurement were concurrent with the formation of β-strand structures [49]. A further study by Elbaum-Garfinkle and co-workers used single-molecule FRET to provide evidence that heparin binding also produces a conformational change, this time in the form of loss of structure in the N-terminal, away from the MTBR (Fig. 1.7 **c)**) [110]. Regardless of the precise mechanism through which heparin associates with tau, it is believed that the reduction of the thermodynamic barrier to self-association of tau must be achieved, first at a conformational level [65, 110].

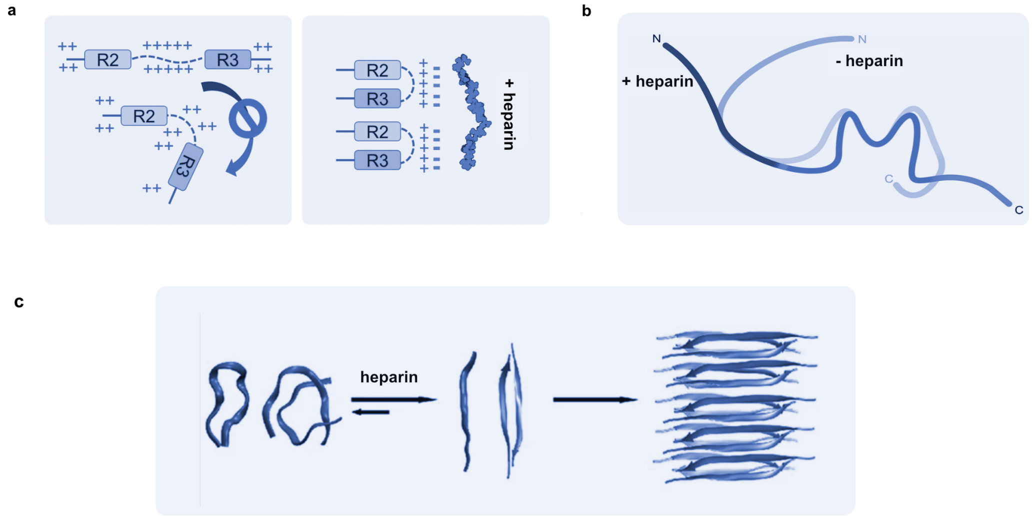

Figure 1.7: The main proposed mechanisms of heparin-induced tau fibrillization. **a)** Heparin neutralizes the charges in the R2- and R3-regions to promote the stacking of MTBR regions. **b)** Heparin binding to tau results in the formation of an extended conformation which is more aggregation-prone. **c)** Heparin causes the MTBR region to become more exposed, following a shift in population to a more extended conformation. Figures adapted with permission from references [49, 65, 110].

Another commonly used class of cofactors is fatty acids such as arachidonic acid. As phospholipids are the components of the cellular membrane, the use of fatty acids is used to study their possible role in tau fibrillization. It was proposed that the micellar structures formed by these amphiphilic molecules allow them to form anionic surfaces, in the form of the protruding carboxyl groups. Although fatty acids were first reported to induce fibrils above the critical micelle concentration of the acid [41], Chirita *et al.* showed that the process was also possible even below this limit [111]. Since micelle theory supported the role of charge neutralization in this process of tau-tau association, the work by Chirita suggested that single molecules of the fatty acid are also capable of binding to the proteins.

Kinetic analyzes using cofactors have also been seen to follow nucleation-dependent polymerization models, with the stoichiometry of tau to heparin and arachidonic binding affecting the kinetics of nucleation and elongation [41, 112, 113]. However, there have been opposing reports, which instead report inducers acting as allosteric inhibitors, with the disappearance of a lag phase after the addition of an inducer [114]. Thus, it is important to note that the type and concentration of inhibitor, as well as the conditions under which fibrillization assays are performed, may result in different mechanistic understandings of a system.

Metal dyshomeostasis has long been considered a key pathological marker of neurodegenerative diseases. [115] The deleterious effects of metal ions such as Zn^{2+},Fe^{2+}, Al^{3+} have been documented, increased levels of some metal ions may be present in parts of the brain affected by certain neurodegenerative diseases [116, 117], while others have shown in certain cases enhanced neurotoxic effects [118–120]. Therefore, several investigations have focused on the effects of different metal ions binding to tau proteins and how it influences its fibrillization kinetics [83, 121].

Al^{3+} is the first metal found in NFTs of patients with Alzheimer's disease [122]. A study performed by Bader *et al.* found that aluminum ions not only increased the rate of fibrillization of tau but promotes the formation of higher-order oligomeric species [121]. Since Al^{3+} was found to form a metal complex with the protein, several chelators have been developed in an effort to destabilize these coordinated complexes. Similarly, attention has also been paid to the effect of Zn^{2+} on tau aggregation, as demonstrated in reports by Huang *et al.* [123]. Low micromolar concentrations of Zn^{2+} dramatically accelerate the rate of fibril formation through metal-coordinated complexes [124]. This is particularly important as Zn^{2+} and other metal ions are usually present in sub micromolar concentrations in the brain, and under pathological conditions, they can be found at micromolar concentrations [125]. Furthermore, Zn^{2+} ions not only increase the aggregation rate but also produce shorter oligomers, which are the far more neurotoxic species [126]. Therefore, it is very important to have *in vitro* assays capable of examining the effects of low micromolar concentrations of inducer while using pathologically relevant levels of protein.

1.5.2 Small molecule inhibiting tau fibrillization

Finding small molecules that are able to specifically bind and target the native conformation of tau is challenging due to the heterogeneous states that soluble tau can assume. For example, most high-throughput screens have resulted in nonspecific or reactive mechanisms [127–129]. Currently, the main methods of inhibiting tau fibrillization are small molecule inhibitors of oligomerization, the regulation of tau phosphorylation, or metal chelation.

Antiphosphorylation therapies involve the search for kinase inhibitors or phosphatase activators. One of the main kinases that phosphorylate serines/threonines is GSK -3β and has thus been labeled a potential therapeutic target for NDs [130]. The small molecule drug Tideglusib is an inhibitor to GSK-3β and was tested in preclinical trials since it was reported to show a reduction in cognitive defects in mouse models, but did not show further benefits in phase II trials [131]. Lithium chloride has also been studied as a potential phosphorylation inhibitor of GSK kinase, but also failed in phase II clinical trials to produce cognitive improvement [132]. Due to these failures, current efforts focus on finding inhibitors for the aggregation process, since phosphorylation control failed to show significant promise [70].

The first compound to be tested in a clinical trial as an inhibitor of tau aggregation was a derivative of the commonly known phenothiazine, methylthioninium chloride (MTC) (Fig. 1.8). Mediation of tau aggregation by MTC was first reported by Wishcik *et al.* in 1996 [133]. The molecule primarily exists in an equilibrium between its oxidized form MTC and reduced form leuco-methylthioninum (LMT). However, when the oxidized version of the molecule was first entered into a clinical trial under the name of Rember, there was no significant improvement in the cognitive abilities of patients. Later, it was discovered that the reduced version of the compound had greater inhibitory properties leading to the development of the drug LMTM (Fig. 1.8), which is a stable reduced version of MTC [61]. The second-generation LMTM drug is in clinical trials (Clinical Trial Identifier: LUCIDUTY, NCT03446001), reaching phase III which will be completed in the next year. It was previously believed that methylene blue derivatives inhibited fibrillization through the oxidation of cysteine residues in the MTBR, however, this was proven by research performed by Al-hilaly and coworkers demonstrating the drug having increased efficacy in reduced conditions [61]. Although the exact mechanism of inhibition is unknown, since *in vitro* assembly of dGAE is affected by LMTM, the authors propose that the MT moiety binds to the MTBR of the protein.

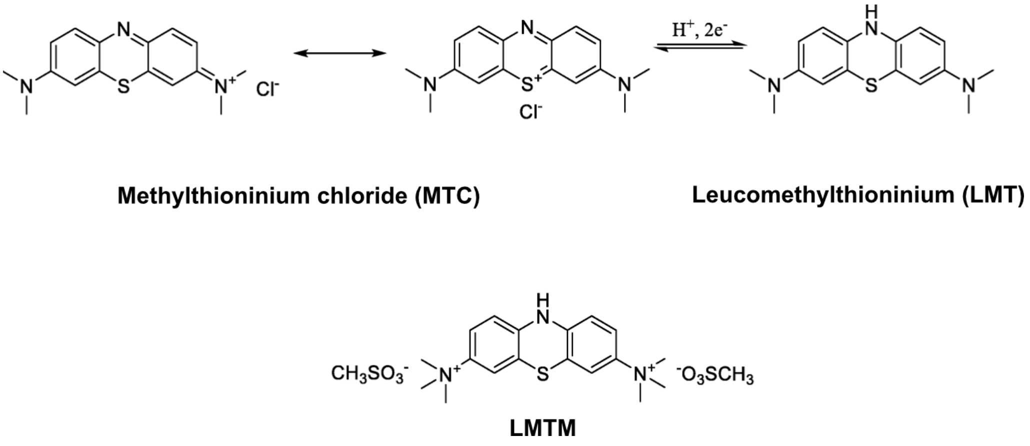

Figure 1.8: Name and chemical structure of the oxidized and reduced versions of methylthioninium chloride as well as its stable, reduced derivative LMTM.

Curcumin is a polyphenol derived from the turmeric plant (*Curcuma longa*) and has been shown in several studies to prevent tau aggregation, with several clinical trials being carried out to evaluate its efficacy [134]. While curcumin has demonstrated the ability to reduce the rate of oligomerization and both Aβ and tau pathology *in vitro* and animal studies, it has failed several clinical trials[135]. Only limited amounts have been reported to enter patient plasma, with limited effects on biomarkers in cerebrospinal fluid and on cognitive tests of patients [136]. Its poor pharmacokinetic properties have led to the study of curcumin derivatives. Two analogs were independently developed termed C1 [137] and PE859 [138] (Fig. 1.9 **a) - b)**) with each showing an effective reduction in the rate of progression of nerve dysfunction and cognitive decline in mouse models.

There are currently no other small molecule inhibitors in clinical trials, the two classes of compounds currently known for their inhibitory activity in fibrillization have been further explored, in addition to several as well as high-throughput *in vitro* screens that aim at identifying other classes of compounds capable of disrupting tau fibrillization.

For example, several naturally occurring polyphenols have also been explored to determine the mechanism by which they may inhibit tau fibrillization. An example is the compound derived from tea extracts, epigallocatechin-3-gallate (EGCG) (Fig. 1.9 **c)**). Studies have been performed to evaluate the interaction of EGCG with tau, as well as its impact on the oligomerization pathway [139, 140]. In a cell-based assay monitored by immunolabelling by Wobst *et al.*, the formation of oligomeric species decreased upon incubation with EGCG. The process was also monitored in a cell-free environment using ThT assays and showed no appearance of larger mature β-sheet amyloid structures [140]. A further study by Sonawane *et al.*, used size exclusion chromatography to demonstrate that EGCG dissolves tau oligomers and disassembles full-length tau fibrils while using isothermal titration calorimetry to indicate that the compound actually binds to tau with micromolar affinity. The studies proposed that polyphenols, such as catechins, serve as good models for the further design of drugs. One such study that further probed the interaction of another polyphenol with tau is that described by Cornejo and coworkers [141]. In this study, rosmarinic acid (Fig. 1.9 **d)**) was shown to inhibit tau fibrillization. Molecular docking simulations reported aromatic groups coordinating the binding to the PHF6 motif, in a hydrogen bond network.

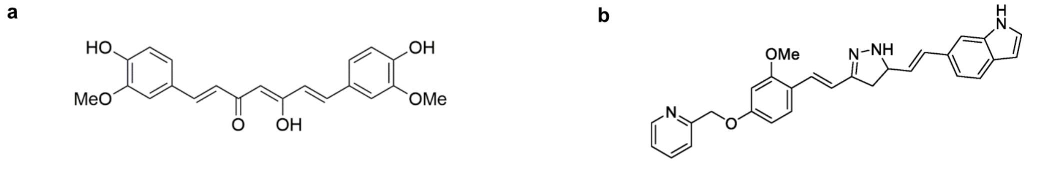

Curcumin **PE859**

Epigallocatechin-3-O-gallate (EGCG) **Rosmarinic Acid**

Figure 1.9: Name and chemical structure of polyphenols currently being used for tau fibrillization inhibition.

One of the first tau inhibitor screens was performed by Taniguchi *et al.* [128], and identified a variety of phenothiazines, polyphenols, and poryphins, as inhibitors. The screen used Thioflavin T and SDS-Page to quantify the presence of fibrillar tau. Although this assay only tested 42 compounds, a high-throughput assay by Bulic *et al.* expanded the screen to 292 000 compounds and identified several new classes of molecules, such as rhodanines, aminothienpyridazines (ATPZs), and benzothiazoles [99]. These classes of compounds, as shown in Fig. 1.10 are now being further studied for the development of therapeutic agents. One such class is the ATPZs which were identified as a new drug scaffold upon which further drug development could be based. The class of compounds was also identified in another high-throughput screen by Crowe *et al.* [142]. ATPZs have been developed into bioavailable derivatives, which have thus far shown high uptake of the drug in mouse models, with successful penetration of the blood-brain barrier [143].

While kinetic analyses of this compound have been conducted, there still remain structural analyses to be performed for compounds, to determine how the compounds interact with tau and its fibrillar structures.

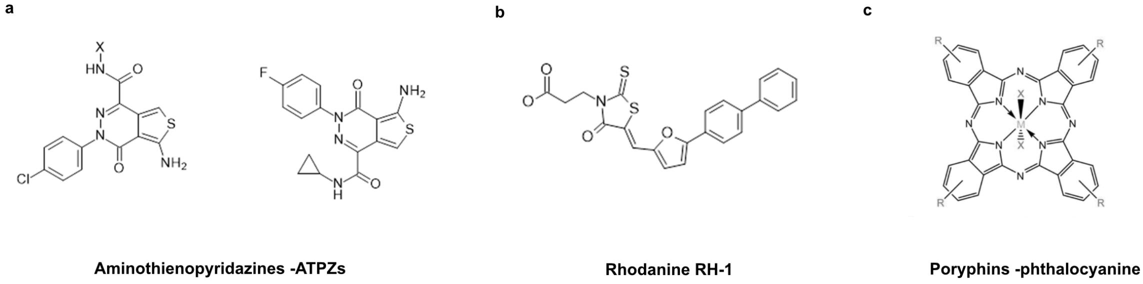

Aminothienopyridazines -ATPZs **Rhodanine RH-1** **Poryphins -phthalocyanine**

Figure 1.10: Name and chemical structure of main chemical classes identified as inhibitors for tau aggregation, as identified in screens by Crowe, Bulic and Taniguchi [99, 128, 142]

Metal ion chelation therapy has also been explored to address the high concentration of transition metals in the brain of ND patients by regulating metal dyshomeostasis [144]. Chelators are molecules that selectively bind to an ion, forming a ring-like coordination complex [145]. Several drugs have been tested in trials that target specific ions; the first to be tested in a clinical trial was deferoxamine, which targets iron and led to a reduction in aggregated $A\beta$, but without significant improvement in cognitive function [146]. Since then, other drugs, such as deferiprone, a lipid-soluble chelator which has also been used to specifically target iron in the central nervous system [147]. Chelators targeting zinc and copper such as clioquinol and PBT2 have recently been tested in animal models of AD. PBT2 is now in phase II of clinical trials with a promising reduction in $A\beta$ in the CSF of patients [148].

1.6 Main biophysical techniques used in this work

1.6.1 Nano-differential Scanning Fluorimetry

Nano-Differential Scanning Fluorimetry (NanoDSF) is a technique that monitors the intrinsic fluorescence of tryptophan and tyrosine residues at 350 nm and 330 nm. The method is based on the concept that the emission maxima of these amino acids experience a redshift when their microenvironment changes from hydrophobic to hydrophilic [149], which typically occurs when these fluorescent amino acids become solvent exposed (Fig. 1.11). Typically nanoDSF can be used to monitor the unfolding events of a protein by monitoring fluorescence emission and then calculating the 350 nm / 330 nm ratio over a temperature ramp. However, in this work, a new method was used to screen for droplet formation to identify conformational changes upon phase separation using the intrinsic fluorescence of the protein. As such, it is used to identify the transition point for these temperature-dependent phase transitions and may offer valuable information on the elusive pathway of soluble tau to an insoluble intermediate filamentous structure. This method can be combined in parallel with dynamic light scattering (DLS) which provides information on the size of molecules in solution and can report on droplet maturation, both over the temperature ramp or over time course measurements.

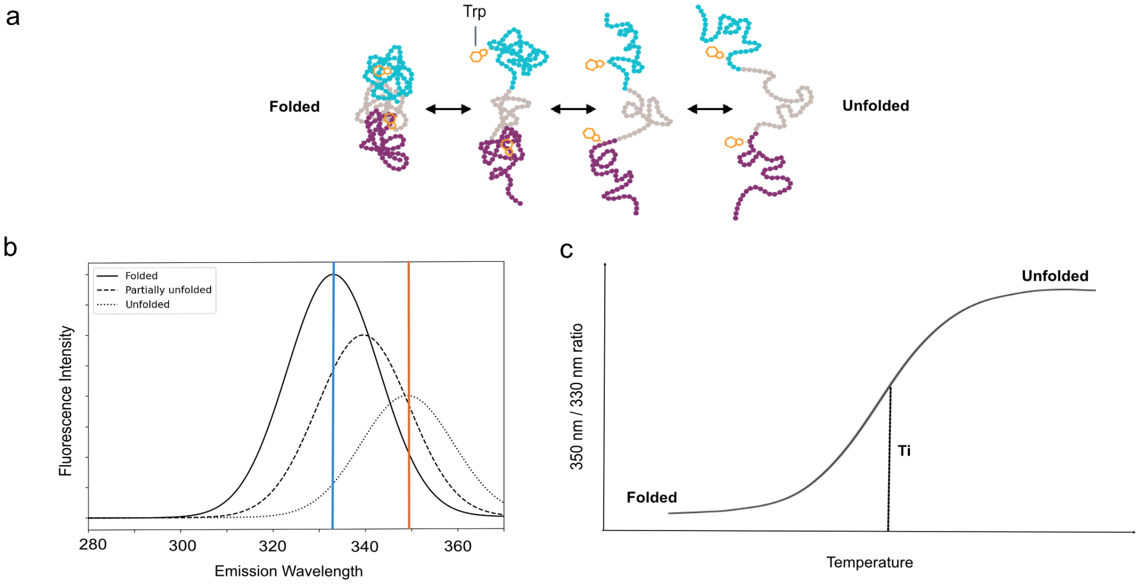

Figure 1.11: a) NanoDSF monitors use the change in the emission maximum on fluorescent amino acids, upon exposure to different microenvironments. **b)** The emission maxima are monitored at two wavelengths 330 nm and 350 nm, which depends on the degree of unfolding of the protein. **c)** Monitoring the 350 /330 nm ratio over a temperature ramp allows protein transitions on a conformational level to be measured.

1.6.2 Spectral Shift

To perform molecular interaction analyzes, spectral shift (SpS) is used to evaluate both the binding affinity constants for various interactions of tau. Spectral shift is a solution-based, low-volume, and high-throughput method. This approach relies on monitoring the extrinsic fluorescence of a dye-labeled target.

Isothermal spectral shift relies on the occurrence of a change in the location and intensity of the fluorescence emission maxima of a fluorophore when its chemical microenvironment is altered (Fig.1.12 **a)**) [150]. The chemical environment of a fluorophore-labeled target changes upon binding to a ligand because of either a change in the conformation of the target protein or just the fact that the ligand is in close proximity to the fluorophore. To detect spectral changes, the emission of the near-infrared fluorophore is detected at two distinct wavelengths simultaneously. Therefore, two detectors at 670 and 650 nm allow for the acquisition of a signal without a time delay of a whole-spectrum measurement and without the need for sequentially measuring the two wavelengths. The ratiometric approach allows the Stoke shift of the fluorophore to be measured with an accuracy of the degree of several picometers.

Typically, a measurement is performed by titrating the labeled target, at nanomolar concentrations, to a serial dilution of the ligand of interest. Each solution is loaded into capillaries and placed on a thermally controlled stage. The fluorophore is excited by an 590 nm LED and the emission at 650 nm and 670 nm is recorded as described. The change in ratio is plotted as a logarithmic function of the concentration of the ligand, from which the affinity constant, K_d is determined using the law of mass action.

Spectral shift assays may also be performed along a thermal ramp, in a fashion similar

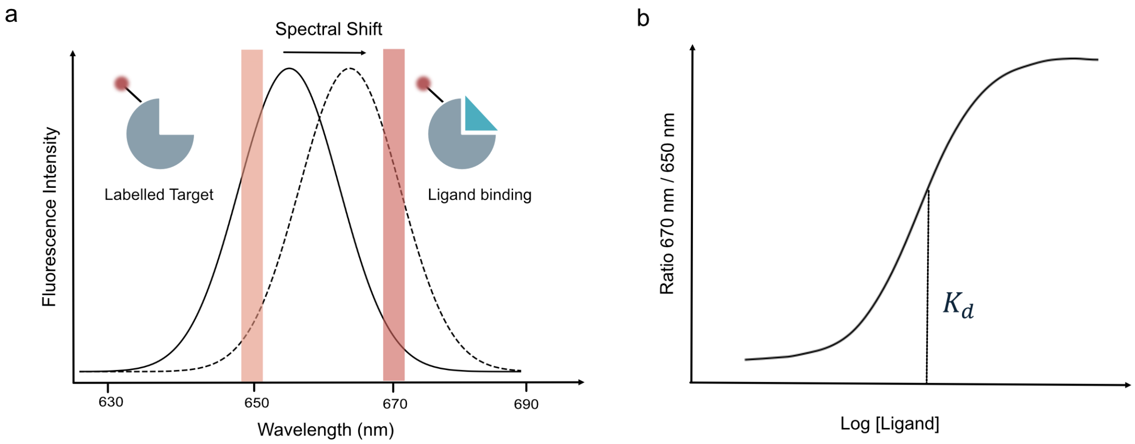

Figure 1.12: a) Spectral shift allows the change in position and intensity of the emission maxima of a fluorophore to be measured, before and after a dye-labeled target binds a ligand. **b)** The 670 nm / 650 nm fluorescence ratio can be plotted as a function of ligand concentration to determine the dissociation constant K_d.

to that of nanoDSF, to monitor the temperature-dependent behavior of systems using extrinsic fluorescence. Because this method relies on the microenvironment of the protein as a reporter of its conformational state, this method can be used to evaluate changes in the assembly of biomolecules labeled with an environmentally sensitive fluorophore. As such, it is proposed as a novel technique to characterize the liquid-liquid phase separation of biomolecules.

1.7 Thesis overview

The goal of this body of work is to develop methods that report processes involved in the early stages of fibrillization of tau, by 1.) characterizing the liquid-liquid phase separation of tau condensates, and 2.) developing affinity-based detection assays to provide high-resolution kinetic data for the oligomerization process.

In the first objective, phase transitions are detected using the intrinsic fluorescence of a protein and spectral shift measurements which allow the conformational changes of any labeled molecule to be determined, over a temperature ramp. In **Chapter 3**, techniques for evaluating these interval-based fluorescence measurements are developed and demonstrated. Dimension reduction techniques are introduced to showcase practices for analyzing multivariate systems, especially when evaluating the multiple factors that govern a phase-separating system. The technique chosen to analyze trends in LLPS was principal component analysis, for which the mathematical workflow is detailed, followed by a description of its implementation in Python. PCA is applied to a well-established metal-triggered Poly A-based phase separating system, proposed by Liu *et al.* [119]. The applicability of PCA to identify the main trends of a data set and the main transition points in the phase separation system are shown and the potential for PCA as a platform for LLPS screens in large data sets is discussed.

The analysis methods discussed in Chapter 3 are implemented in **Chapter 4** to highlight the trends in the conditions that regulate electrostatic and hydrophobically induced liquid-liquid phase separation of tau. These high-throughput fluorescence-based methods allow low-volume and low-concentration measurements of LLPS as an alternative to absorbance turbidity measurements. This allows not only the cloud point temperatures to be measured but also the critical concentrations for LLPS. The conditions identified in the high-throughput assay are then studied using confocal microscopy, which verifies droplet formation and provides data on droplet dynamics with Fluorescence Recovery After Photobleaching (FRAP) measurements. Lastly, the overlap of several LLPS conditions with the fibril-forming behavior is further explored to show the biological relevance of the findings.

The second objective focuses on the development of aptamer-based detection assays that aim to improve the measurement of early fibril formation using real-time measurements that can surpass the current state-of-the-art ThT assays. The spectral shift assays reported here allow quantification of the early stages of oligomerization, through affinity-based detection. **Chapter 5** documents the assay development, highlighting the importance of labeling approaches when measuring interactions. The robustness and range of applicability of the aptamer assay are tested in the presence of an inducer and various inhibitors. As such, different factors affecting the nucleation and elongation processes are explored using the in-solution aptamer assay.

The concept of using affinity-based spectral shift assays is further explored in **Chapter 6** which discusses the development of fluorescence-enhanced plasmonic assays. DNA-gold nanorod systems are optimized to provide signal amplification of the affinity-based detection systems proposed. The stability and applicability of three different oligonucleotide gold conjugates are characterized and assessed for use in both interaction and kinetic measurements. As such, each of the methods developed in this thesis aims to challenge the state of the art biophysical characterization of the various assembly states of tau.

Chapter 2

Materials and Methods

2.1 Materials

Lyophilized recombinant tau proteins and peptides of various constructs were obtained from two main manufacturers; Acrobiosystems and Biosyntan, with the two main projects-phase separation assays and fibrillization assays, utilizing items with a single lot number in an effort to avoid batch-to-batch variation. All HPLC-purified oligonucleotides were obtained from Integrated DNA Technologies (Leuven, Belgium). The names and sequences are indicated from 5′ to 3′ end, with modifications for each strand indicated in specified experiments. In the subsequent sections the experimental protocols and in some cases, methods of analysis are documented.

Table 2.1: List of proteins and suppliers.

Protein	Company
His-Tagged Human Tau-2N4R cat. no ACRBTAU-H51H4-100uG	Acrobiosystems,VWR, Darmstadt,DE
Tau 2N4R (Tag-Free) cat. no ACRBTAU-H51H3100UG	Acrobiosystems, VWR, Darmstadt,DE
Tau 2N4R (P301L)	Acrobiosystems, VWR, Darmstadt,DE
Recombinant Human Tau (K18)	bio-Techne, England UK
Tau R3 peptide	Biosyntan, Berlin,DE
Tau R3 peptide (P322S)	Biosystan, DE

Table 2.2: List of commonly used buffers and components.

Buffer	Composition
Storage Buffer	50 mM HEPES, 150 mM NaCl, 2mM DTT, 1mM EDTA (pH 7.5)
HEPES-T Buffer	0.05 % TWEEN in HEPES buffer
HEPES-P Buffer	0.1% Pluronic F-127 in HEPES buffer
LLPS Buffer	50 mM HEPES, 2 mM DTT,(pH 7.5)
Buffer A	20 mM TRIS, 100 mM NaCl, 1 mM EDTA, 0.01% Tween-20, pH 7.5
PBS Buffer	137 mM NaCl, 2.7 mM KCl, 8 mM Na_2HPO_4 and 2 mM KH_2PO_4, (pH 7.4)
NHS Labelling Buffer	130 mM $NaHCO_3$, 50 mM NaCl, (pH 8.2)

Table 2.3: List of Chemicals and Suppliers.

Chemical	**Supplier**
Aminothienopyridazine (ATPZ)	Sigma-Aldrich Co. GmbH, Taufkirchen, DE, cat. no. 580222
Bovine Serum Albumin	Fisher Scientific GmbH, Schwerte, DE, cat. no. 23209
Calcium chloride	Sigma-Aldrich Co. GmbH, Taufkirchen, DE, cat. no. C1016
Curcumin	Sigma-Aldrich Co. GmbH, Taufkirchen, DE, cat. no.239802
Deferasirox	Sigma-Aldrich Co. GmbH, Taufkirchen, DE, cat. no. SML2673
DMSO ($\geq$ 99.8 %)	Carl Roth GmbH + Co. KG, Karlsruhe, DE, cat.no. A994.2
DTT	Carl Roth GmbH + Co. KG, Karlsruhe, DE, cat. no. 6908.2
Epigallocatechin-gallat,EGCG (-)	Acros Organic BVBA, Massachusetts, US, cat. no. 15214248
Ethylenediaminetetraacetic, EDTA	Carl Roth GmbH + Co. KG, Karlsruhe, DE, cat. no.8040.1
Gold nanorods	Sigma-Aldrich Co. GmbH, Taufkirchen, DE, cat. no. 771686
HEPES	Carl Roth GmbH + Co. KG, Karlsruhe, DE, cat. no. HN78.2
Heparin sodium salt	Sigma-Aldrich Co. GmbH, Taufkirchen, DE, cat. no. H3149
1,6-Hexandiol	Sigma-Aldrich Co. GmbH, Taufkirchen, DE, cat. no. 240117
Hydrochloric acid	Sigma-Aldrich Co. GmbH, Taufkirchen, DE, cat. no. 258148
Magnesium Chloride	Sigma-Aldrich Co. GmbH, Taufkirchen, DE, cat. no. M8266
Methylene Blue	Sigma-Aldrich Co. GmbH, Taufkirchen, DE, cat. no. 457250
Pluronic® F-127	Sigma-Aldrich Co. GmbH, Taufkirchen, DE, cat. no. P2443
Polyethylene glycol, PEG 30	Sigma-Aldrich Co. GmbH, Taufkirchen, DE, cat. no. 25322-68-3
Poly(ethylene glycol)methyletherthiol	Sigma-Aldrich Co. GmbH, Taufkirchen, DE, cat. no. 729140
Poly-deoxy-adenylic acid	Sigma-Aldrich Co. GmbH, Taufkirchen, DE, cat. no. 10223581001

Chemical	Supplier
Polyuridylic acid potassium salt	Sigma-Aldrich Co. GmbH, Taufkirchen, DE, cat. no. P9528
Protein Standard Mix 15 - 600 kDa	Sigma-Aldrich Co. GmbH, Taufkirchen, DE, cat. no. 69385
Rosmarinic Acid	Sigma-Aldrich Co. GmbH, Taufkirchen, DE, cat. no. R4033
Roti®-Stock 10x PBS	Carl Roth GmbH + Co. KG, Karlsruhe, DE cat. no. 1058.1
Sodium Chloride,NaCl	Carl Roth GmbH + Co. KG, Karlsruhe, DE, cat. no. 0962.1
Sodium hydroxide,NaOH	Carl Roth GmbH + Co. KG, Karlsruhe, DE, cat. no.S8045
TCEP	Sigma-Aldrich Co. GmbH, Taufkirchen, DE, cat. no. C4706
Thioflavin T	Sigma-Aldrich Co. GmbH, Taufkirchen, DE, cat. no. 8818254467
Tris Buffer	Carl Roth GmbH + Co. KG, Karlsruhe, DE, cat. no. 201-064-4
Tween®-20	Sigma-Aldrich Co. GmbH, Taufkirchen, DE, cat. no. 93773
Zinc Chloride, ZnCl	Sigma-Aldrich Co. GmbH, Taufkirchen, DE, cat. no. 7646-85-7

Table 2.4: List of oligonucleotides and suppliers.

Oligonucleotide	Sequence
Aptamer A	Cy5 - GCGGAGCGTGGCAGG
Aptamer B	GCGGAGCGTGGCAGG - Cy5
Aptamer C	Cy5 - TTTTGCGGAGCGTGGCAGG
Aptamer D	GCGGAGCGTGGCAGGTTTT - Cy5
ssDNA1	Cy5 - TTGCGGAGCGTGGCAGGTT- SH
ssDNA2	SH-TTCCTTCCTCCGCAATAC - Cy5
ssDNA3	TTGCGGAGCGTGGCAGGTT- SH
ssDNA4	Cy5 - GTCCAGACTCTT - SH
ssDNA5	SH-TTGAGTCTGGACTTGCGGAGCGGGCAGG

2.2 Protocols for Interaction Analyses

2.2.1 Preparation and Storage of Tau

Each construct of recombinant lyophilized tau listed in table 2.1 was obtained in 500 µg vials. Reconstitution of protein was performed by re-suspending lyophilized material into 500 µl of storage buffer, at room temperature, and slowly stirred for 30 minutes to

Table 2.5: List of instruments and manufacturers.

Device	Supplier
Monolith X	NanoTemper Technologies GmbH, Munich, Germany
Prometheus Panta	NanoTemper Technologies GmbH, Munich, Germany
Prototype Prometheus -Andromeda X	NanoTemper Technologies GmbH, Munich, Germany
Dianthus	NanoTemper Technologies GmbH, Munich, Germany
Tycho	NanoTemper Technologies GmbH, Munich, Germany
CLARIOStar Fluorescence Plate Reader	BMG Labtech GmbH, Ortenberg, Germany
Nanophotometer NP80	Implen GmbH, Munich, Germany
UV-Visible Spectrophotometer V-750	JASCO Deutschland GmbH, Pfungstadt,Germany
Spectrofluorometer FP-8300	JASCO Deutschland GmbH, Pfungstadt,Germany
ÄKTA pure™ 25L	Cytiva™ , Uppsala, Sweden
Stellaris 5 Confocal Microscope	Leica Microsystems, Wetzlar, Germany

ensure the protein was completely dissolved using a rotating table tube revolver. For LLPS samples, the protein required the removal of salt, detergents, and protectants, so a buffer exchange was performed using Amicon-Ultra (3K) 0.5 ml spin-centrifugal filters (Sigma-Aldrich). Re-suspended tau solution was diluted to 500 µl, with the desired buffer, and centrifuged for 25 minutes at 10000 x*g* at 4 °C. The remaining 50 µl of concentrate was then re-diluted to 500 µl and the process repeated. After concentrating the sample, to 50 µl, the protein was then either aliquoted into 10 µl PCR-tubes and stored at -80 °C or used directly in experiments.

2.2.2 Protein Concentration Determination

The concentration of the protein after re-suspending into new buffers was determined by Beer- Lambert's law, using the 280 nm fluorescence of the protein. The extinction coefficient ϵ of tau was calculated using the PROTPARAM tool [151], and determined to be 7450 $M^{-1}cm^{-1}$. A nanophotometer was then used to measure the absorbance of the sample and protein concentration was determined using $c = A/\epsilon.l$, where l is the path length in cm.

2.2.3 DLS for protein stability

Dynamic Light Scattering was used to assess the size and monomeric nature of the protein after preparing the stock. To do so, 10 µM of 1 mg/ml sample was loaded into the (High Sensitivity Capillaries, PR-C006) and placed on the temperature-controlled tray of the Prometheus Panta (NanoTemper Technologies GmbH). A size analysis measurement was performed to obtain a distribution profile and hydrodynamic radius for the protein sample.

2.2.4 Microscale Thermophoresis and Spectral Shift

The interaction of various tau constructs with several ligands were studied using Microscale Thermophoresis (MST) and Spectral Shift Technology (SpS) using a Monolith X instrument. The following is a standard experimental method for determining binding affinity.

Pretests.

Fluorescently labeled protein target is diluted to a low nanomolar concentration and loaded into capillaries (MO-K025, NanoTemper Technologies, GmbH) or flat bottom 384-well plates (DI-P001C, NanoTemper Technologies, GmbH) to perform a pretest in which the LED excitation power is determined.

Following optimization of fluorescent and IR intensities, a binding check can be performed by preparing two samples, one with labeled target and buffer, and another with a labeled target and the highest available concentration of ligand. The samples are loaded into either the Monolith or Dianthus to validate if a sufficient signal-to-noise ratio could be obtained.

Capillary and Plate Based detection

After successful pre-tests, a 16-point dilution series is prepared by performing a 1:1 dilution series 16 times into the assay buffer (Fig. 2.1. After the dilution series is complete, 10 µl of the labeled target is added to each of the tubes. The mixture is then loaded into capillaries, or microwell plates and loaded into respective devices.

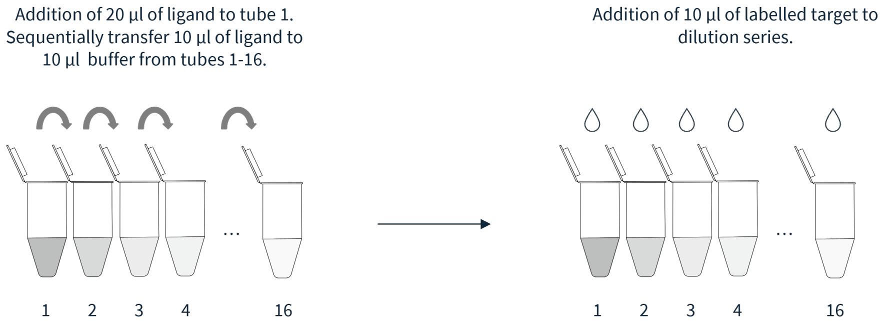

Figure 2.1: A 16-point dilution series is made by mixing a fixed volume of ligand with equal volumes of buffer. The highest concentration of ligand is in tube 1, with 10 µl of buffer in tubes 2-16.

2.2.5 Fluorescence Labeling Methods

Histag Labelling

The RED-tris-NTA 2nd Generation dye (MO-L018, NanoTemper Technologies GmbH) site specifically labels the full-length tau with a poly-histidine tag at the N-terminal of the protein. To ensure the dye successfully labels the protein, the interaction affinity between the dye and the protein was measured. A 5 µM solution of dye is made by suspending the stock in 25 µl of HEPES-T buffer. The dye was then diluted in 200 µl of buffer to create a 50 nM solution. A solution of 4 µM Histagged tau was created by diluting the 20 µM stock in HEPES buffer was created. A dilution series of tau was prepared as described in Protocol 2.2.4, to which 10 µl of 50 nM dye was added. The mixture was incubated for 30 minutes at room temperature and capillaries loaded into the Monolith X. The Kd can be determined in MO. Control or MO.Affinity Analysis using the Kd fit.

After the determination of the affinity between the dye and the tagged protein, the interaction between the labeled protein and ligand of interest can be calculated. If the affinity of the dye to the protein is < 10 nM, then the concentration of the following protocol is used. If the interaction of the protein and the dye was weaker than 10 nM, the concentration of protein was adjusted to more than 20 times the K_d. 20 µM stock protein was diluted to 200 nM, in HEPES-T buffer. Meanwhile, 125 pmoles of the dye was suspended in 25 µl of buffer to create a 5 µM solution. 2 µl of dye was mixed with 98 µl of buffer, to create a 100 nM solution of dye. 100 µl of dye (100 nM) is mixed with 100 µl of protein (200 nM) and incubated for 30 minutes, at room temperature, in the dark. The 100 nM labeled protein can then be used in interaction measurements.

NHS Labeling

Tau protein without a Histag was labeled with RED-NHS 2nd Generation dye (MO-L011, NanoTemper Technologies GmbH). The dye has a reactive NHS-ester group which covalently binds to primary amines - primarily the lysine residues - on the protein [152].

Tau was equilibrated into NHS-Labelling buffer (Table 2.2), and concentration was determined via method 2.2.2. To obtain a 600 µM solution of RED-NHS 2nd Generation dye, 25 µl of DMSO was added to 10 µg dye. Just prior to mixing with protein, the dye was then diluted with NHS-Labeling Buffer to three times the protein concentration. Equal volumes of protein and dye were mixed together and incubated for 30 minutes in the dark. Free dye was removed from labeled protein using a prepacked G-25 Medium Sephadex desalting column (Cytiva, Sweden) equilibrated in dilution buffer following the manufactures instructions. The labeled protein was then stored on ice, and concentration was determined by absorbance measurements.

For samples for the oligomeric state of the protein was needed to be assessed post-labeling, size exclusion chromatography was used. A Superdex 200 Increase Column (Cytiva, Sweden) was attached to an Akta Pure System. Prior to sample addition, the column was equilibrated with 2 column volumes (cv) of HEPES-P. 100 µl labeling mixture was applied to the column, and eluted with 1.5 cv of HEPES-P with a flow rate of 0.5 ml min^{-1}. Sample elution was monitored using UV detection at 280 nm and 650 nm, with absorbance used to calculate the sample concentration of each eluted peak. Peaks were collected as 100 µl fractions in a 96 deep-well plate, aliquoted, and used for further experiments.

2.3 Kinetics measurements

2.3.1 Thioflavin T Assays

Tau fibrillization was monitored using Thioflavin T (ThT) fluorescence assay. Briefly, in a ClarioStar Fluorescence plate reader (BMG LabTech GmbH, Germany) was used to record the fluorescence intensity over time for various fibrillization conditions. ThT excitation was at 450 +/- 15 nm emission was collected at 490 +/- 15 nm using detectors from the top of the plate. Assays were performed in HEPES buffer (50 mM Hepes, 150 mM NaCl, 1 mM EDTA, 2 mM DTT, pH 7.4), 10 µM of Tau was mixed with 5 µM ThT. Samples were placed in 384 flat bottom well plates (Greiner, Austria) and sealed using transparent sealing foils .which were shaken at 400 rpm and fluorescence intensity was recorded every 15 minutes over a period of 72 hours.

2.3.2 Automated Liquid Handling

For experiments that required the preparation of 384- microwell plates, an INTEGRA Assist Plus pipetting robot (Integra Biosciences GmbH, Germany) was used for the preparation of multiple serial dilutions. A liquid dispensing program was first specified using the Integra Vialab Software (v 3.01.02), with protocols shown in the Appendix which defined the volume of liquid required for each dilution, and the position of the pipette tips upon dispensing and the sequence in which each well was filled. The relevant solutions were prepared and the Dianthus micro-well plate was placed onto the platform and the program was initiated. All programs were first tested using a control fluorophore and buffer to ensure accurate implementation.

2.3.3 Automated Dianthus Spectral Shift Measurements

Kinetic experiments monitoring the rate of association (k_{on})of a binding partner with a fluorescently labeled target were achieved by automating a Dianthus with Spectral Shift (NanoTemper Technologies) using the Momentum (v. 6.1, Thermo scientific) scheduling software, where a specific process was written to allow time-resolved on-line measurements to be performed. The Momentum process is used to control an Orbitor RS1 arm to move the pre-prepared plate from a random access hotel into the Dianthus, at which point, the process calls Di.AutoControl (v. 2.0.1) which is a command line interface to the Dianthus remote procedure call (gRPC) interface. Prior to measurements, the excitation of the assay was set by running the first measurement in Di.Control (v. 2.0.1) after which is coded as a flag within the command used to call Di.AutoControl. A standard .dic file is then created after the measurement which includes the time of each measurement, allowing for time-resolved measurement of changes in Spectral shift as binding occurs.

2.4 Data Analysis

2.4.1 Evaluation of dissociation contants

The dissociation constant (K_d) is determined by fitting the spectral shift dose-response curve with a binding model using the law of mass action. The fraction bound $f(c_{\mathrm{ligand}})$ is evaluated for a particular ligand concentration c_{ligand}, using the following formula.

$$f(c_{\mathrm{ligand}}) = \frac{c_{\mathrm{ligand}} + c_{\mathrm{target}} + K_{\mathrm{d}} - \sqrt{(c_{\mathrm{ligand}} + c_{\mathrm{target}} + K_{\mathrm{d}})^2 - 4.c_{\mathrm{ligand}}.c_{\mathrm{target}}}}{2c_{\mathrm{target}}} \tag{2.1}$$

where c_{target} is the target concentration. The dissociation constant is then evaluated as:

$$R(c_{\mathrm{ligand}}) = R_{\mathrm{unbound}} + f(c_{\mathrm{ligand}}).(R_{\mathrm{bound}} - R_{\mathrm{unbound}}) \tag{2.2}$$

where $R(c_{\mathrm{ligand}})$ is the ratio value for a specific ligand concentration, and R_{unbound} and R_{bound} are the ratios for the unbound and bound target respectively. Evaluation of K_{d} was either performed using the MO. Control Software (v 2.5.4) or using Python. The packages NumPy and Matplotlib were used to implement the fits described in the above equations and can be found in Appendix B.1.

2.4.2 Evaluation of observed kinetic rate constants

The evaluation of kinetic constants k_{obs}, were evaluated by fitting data to a single exponential equation.

$$y = A(1 - \exp(-k_{\mathrm{obs}} \cdot t) + y_0) \tag{2.3}$$

$$t_{1/2} = \frac{ln2}{k_{\mathrm{obs}}} \tag{2.4}$$

where y is the amount of bound target at time t, y0 is the initial amount of bound target and A is the preexponential factor. All fits were implemented in Python, using the *curvefit* function in the *scipy.optimize* package. For fits that required a global fit, several progress curves were evaluated together, using k_{obs}, as a shared parameter as shown in Appendix B.2.

2.5 LLPS Measurements

2.5.1 Turbidity Assays

A JASCO V-750 spectrophotometer (JASCO, Germany), was used to measure the changes in turbidity via absorbance measurements. Tau condensate samples were prepared in

LLPS buffer (2.2), with varying salt concentrations as described in Chapter 4. Low-volume 20 µl quartz-cuvettes were filled by tilting to a forty-five-degree angle and injecting the sample into the well with a small-volume pipette. The UV spectra between 300 nm - 400 nm were measured over a temperature ramp, for LLPS samples in the presence and absence of inhibitors. Controls with the given inhibitors in LLPS buffer were also performed in parallel to the measurement of the sample. For temperature ramp measurements, the JASCO software was used to set the heating rate of the samples were heated to 1° C/min, in order to determine the cloud point temperature.

2.5.2 nanoDSF and DLS

A Prometheus Panta instrument (NanoTemper Technologies GmbH) was used to measure the nanoDSF and dynamic light scattering experiments in parallel to characterize phase-separating systems. Samples were prepared and loaded immediately into capillaries (High Sensitivity Capillaries, PR-C006). For thermal ramps, samples were heated at a rate of 1° C/min, with fluorescence ratio values being measured approximately every 2 seconds. For samples with large scatters, a longer acquisition time was selected, resulting in DLS measurements every 5 seconds. Prior to each experiment, all capillaries were sealed with a paste (NanoTemper Technologies GmbH), to prevent evaporation of the sample. The cloud point temperatures and droplet size were then determined from the data, as detailed in Chapter 4.

2.5.3 Protocol for Confocal Microscopy Imaging

To validate LLPS measurements *in vitro* using nanoDSF and DLS measurements, confocal microscopy directly visualized the formation of tau droplets under a variety of conditions. Full-length tau with a His-tag at the N-terminal of the protein was labeled with Cy5 fluorophore-conjugated with Tris-NTA, via the method described in section 2.2.5. The his-tagged protein (5 µM)was labeled in a 1:1 ratio with the dye in LLPS buffer, and this labeled mixture was combined with unlabeled tau in a 1:10 ratio, in order to produce an ideal signal: noise output upon imaging. 4 µl of sample was placed onto silicon isolators which were secured onto a glass slide and subsequently sealed with a coverslip. Samples were imaged on a Leica Stellaris 5 microscope (60 x Oil Immersion Objective), with illumination performed with a 683 nm laser, and light collected through a Power HyD photon counting detector. The gain, scanning speed, and objective were fixed for all experiments. Experiments were performed at 25 ° C, for isothermal measurements, and for thermal ramps the microscope was connected to a VAHEAT heating stage (Interherence, Erlangen, DE) for temperature control.

Droplets were loaded onto the slides immediately after desalting using an Amicon Spin Ultra filter columns, and subsequently imaged after one hour and then again at 4 hours. Droplets were imaged by finding the z-position at which the edges were in sharp focus, and a corresponding z-stack taken for three population areas. Images were processed using both ImageJ (detailed in Chapter 4) and a Python image processing pipeline (detailed in Appendix A.2). To evaluate droplet size, the z-stack for which droplets were in focus was chosen and placed through the processing pipeline.

2.5.4 Fluorescence Recovery After Photobleaching

In some cases, additional information on the viscoelastic properties of the droplet over time was determined using Fluorescence Recovery After Photobleaching (FRAP) experiments. FRAP measurements were obtained by bleaching a region of interest on the particle with high-intensity laser light for 3 seconds. Prior to bleaching the intensity of the fluorescence in the selected region was measured, and the intensity in the region after bleaching was monitored for 300 seconds. The recovery of fluorescence in the region of interest is an indication of diffusion of labeled protein within the droplets. In order to process FRAP images, the intensity in the region of interest was corrected for the overall bleaching of the sample by normalizing to another unbleached region of interest in the particle.

2.5.5 Image Processing

A Python image processing pipeline was created to evaluate the droplet size and density using the OpenCV image processing library [153] (see Appendix A.2). To calculate the size of a droplet, the image is converted to a greyscale to enhance contrast, and a threshold value set to eliminate both small aberrations and out-of-focus droplets. Using the Otsu threshold algorithm, this threshold can be detected automatically. A circular mask is applied to the detected edges of the droplets in the image. The mask is used to determine the area, size and number of droplets. From each micrograph, the distribution of droplet area is calculated, and a secondary plot of average size over time is produced.

2.6 Development of in-solution plasmonic assays

2.6.1 Characterization of Gold Nanorods

Cetyltrimethylammonium bromide (CTAB) coated 60 nm x 40 nm gold nanorods (Sigma-Aldrich) in aqueous solution were characterized using Dynamic Light Scattering to determine the stability and monodispersity of particles prior to functionalization. 10 µl of stock rods into three premium coated capillaries and loaded into the Prometheus panta. A size analysis experiment at 25 °C was performed in high-sensitivity mode, which takes 10 acquisitions for each sample. The absorption spectra of the nanorods were characterized by UV-Visible spectroscopy using a JASCO spectrophotometer, by performing an absorbance spectra scan in the range of 400 nm - 750 nm, at an acquisition rate of 1000 nm/min. The stability of rods was characterized before and after each functionalization step.

2.6.2 Activation of thiolated oligonucleotides

After characterizing rods with absorbance and DLS, the functionalization with thiolated ssDNA strands (IDT) could be performed. In order to reduce the thiol-modified oligonucleotides to the active sulfhydryl form, ssDNA was treated with 100 X excess of TCEP for one hour at room temperature, as per manufacturers' instructions. G-25 DNA Grade Sephadex Columns (Cytiva, Sweden), were used to remove the excess reducing agent, by first equilibrating the column in TE Buffer and adding 100 µl of 100 µM sample, followed by 500 µl of Buffer. The absorbance of the samples was then measured to calculate the concentration of the samples, using their given extinction coefficients. The thiol-activated oligonucleotides were either used immediately or stored in 10 µl aliquots at - 20 ° C.

2.6.3 Acid Functionalization of Gold Nanorods

1 ml of nanorods were placed in a polypropylene 2 ml centrifuge tube and spun for 10 minutes at 5000 x g, in order to begin CTAB-removal. The rods pelleted to the bottom of the tube and the supernatant was removed. The reduced ssDNA was added to the gold nanorods followed by reconstitution in TRIS-HCl (20 mM Tris, 100 mM NaCl, 0.01% Tween-20) buffer which was adjusted to pH 3. The reaction was left for five minutes at room temperature, and subsequently centrifuged for 10 minutes at 5000 x g. The rods were re-suspended in HEPES-T buffer, and the washing step was repeated three times. After the functionalization of gold rods, the absorbance spectra and DLS measurements were performed to assess the stability of the AuNR-ssDNA complex. The quantification of dye-labeled ssDNA on the gold nanorods was done via a ligand displacement protocol [154], using 0.5 M DTT. A calibration curve was created by measuring fluorescence counts on the prototype Andromeda (NanoTemper Technologies GmbH), using known concentrations of the free-labeled aptamer in the HEPES-T buffer. The fluorescence of the labeled system was monitored over 10 hours to determine the fluorescence of unattached strands. The calibration curve was then used to estimate the amount of strands in solution and the number of strands per rod was determined by dividing the concentration of dye molecules by the rod concentration.

2.6.4 Pegylation of nanorods

Nanorods were pegylated in a protocol adapted initially from reference [155]. Firstly CTAB removal was performed by centrifuging 1 ml of nanorods for 10 minutes at 5000 x g. The supernatant was again removed and 50 µl of 1 mM mPEG -SH, and 1 ml of 0.01 % Tween. The centrifugation and resuspension steps were repeated 3 times, each time reintroducing Tween and mPEG-SH. The activated thiolated ssDNA was added to the pellet, after the third wash, and the solution was brought to 1 ml in Buffer A (20 mM Tris, 100 mM NaCl, 0.01% Tween-20, pH 7.5). The solution was incubated for one hour, after which the centrifugation and wash steps were repeated three times. The final solution was resuspended in Buffer A, and the concentration of the rods and oligonucleotides was characterized as in Section 2.6.1.

2.6.5 BSA passivation of nanorods

In order to coat the surface of the gold nanorods post-oligonucleotide a Bovine Serum Albumin (BSA) was used as a passivation agent. The oligonucleotide functionalization for the nanorod system was carried out as described in Section 2.6.3, with relevant strands. Then, 500 µl of 2 nM DNA-AuNR conjugate was added to 500 µl of 1 µM BSA and incubated for 1 hour at room temperature. The stability of the mixture was then assessed by its absorbance spectra and dynamic light scattering.

Chapter 3

Data analysis techniques for analyzing temperature-dependent phase transitions.

The techniques and approach chosen to evaluate a data set greatly dictate the quality and quantity of information that can be uncovered. The experimental methods described in this chapter and used in the next chapter produce fluorescence intensity measurements, in the form of traces which must be analyzed. In the case of nanoDSF and Spectral Shift (SpS) assays, this means that the intensity changes over a temperature ramp. The characteristics of a temperature-fluorescence trace (hereafter just trace) that are deemed important depend on the nature of the experiment but typically center around the amplitude of a signal as a function of temperature or a rapid change in intensity, normally reported as an inflection point. Mathematically, this means that the curvature of a trace must then be evaluated either within an area of interest or by analyzing the entire curvature. This chapter reviews techniques that are currently used to analyze intrinsic (nanoDSF) and extrinsic (Sps) fluorescence data sets and introduces a new comprehensive analysis approach derived from principal component analysis (PCA), designed to obtain shape descriptors from large data sets.

Principal component analysis is a technique that allows a data set to be reduced to a function of the main variances that determine the overall behavior of the data set. This technique is valuable in evaluating large sets of data, which may have multiple governing variables, by reducing the dimensionality to a few distinct variables [156]. When this method is applied to the fluorescent ratio traces, the main variances influencing the signal, called the principal components, can be obtained. Decomposing the signal into these independent components is a useful technique since conditions that best represent the overarching trends in the data set can be derived. For instance, for a data set where there are minute changes in the position of an inflection point, or where the amplitude of the signal varies slightly with a corresponding change in experimental conditions, each represents sources of variance in a data set. The method developed and described in this chapter aims at detecting these variances and quantifying them in a descriptive way.

3.1 Evaluation of onset and inflection points

The two main parameters defined for characterizing protein unfolding in intrinsic and extrinsic fluorescence measurements are the temperature of unfolding onset (T_{onset}) and the inflection point (T_{i}). Fig. 3.1 shows an example trace for the evaluation of a simple two-state transition. To calculate T_{onset}, a threshold is set that defines the percentage for which the fluorescence ratio should change relative to a baseline (typically set to 0.5 %). The algorithm currently used in the software packages Panta Control and Andromeda Control (NanoTemper Technologies, GmBH), uses a reference x-value for which the trace is unchanged, or baseline, and then slides a 'window' along the trace. A fitting window is determined on the basis of the first inflection point, after which a two-state model is fitted to the data. The temperature at which the exponential part of the two-state fit deviates more than the given threshold from the linear part is determined as the onset temperature.

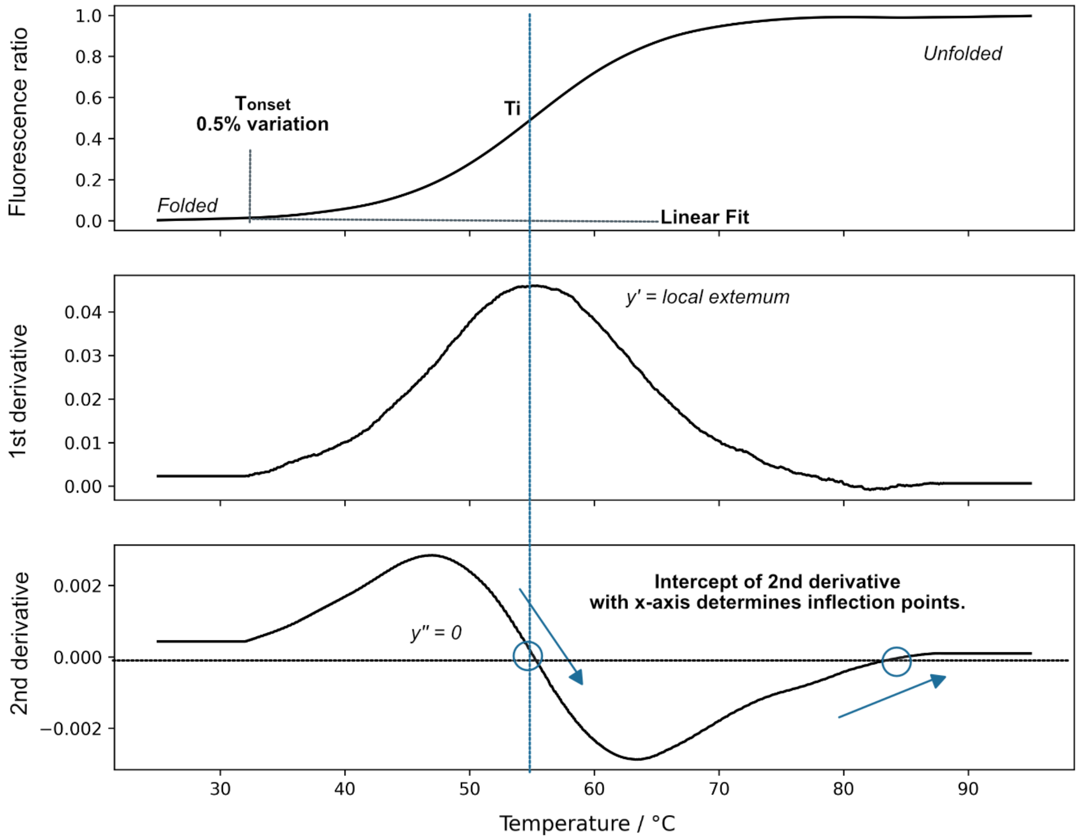

Figure 3.1: The onset point of a fluorescence trace can be determined by establishing a baseline and scanning along the curve until a change in signal above a certain percent, here 0.5% above the baseline is found. The first and second derivatives of the trace are calculated and used to determine the points of inflection. The x-intercepts at points of the curve in the opposite direction to the original trace are chosen as valid inflection points.

For systems that exhibit distinct transition points (e.g. proteins), the inflection points can be calculated. The inflection point is a good estimate of the temperature where half of the protein underwent the transition that is represented by the change in the ratio of the intensities (in most cases unfolding). Mathematically, the inflection point represents the point where a curve changes direction from convex to concave or vice versa. At an inflection point, the curve's first derivative reaches a local maximum or minimum, and the second derivative changes sign. Therefore, a simple way to calculate the inflection point of a trace is to first smooth the data points and calculate the first and second derivatives, an example of which is shown in Fig. 3.1. Curve smoothing refers to the process of reducing noise in the signal by applying a locally weighted regression. LOWESS (locally weighted scatterplot smoothing), is used to smooth traces, which performs a moving weighted average on data points along the trace [157] (refer to code in Appendix A.1). The intercept of the second derivative and the x-axis is determined, but only the points showing an opposite direction in the second derivative compared to the original curve are identified as inflection points.

This method is feasible for a wide array of cases, but there are a few limitations. For instance, the onset temperature evaluation is particularly meaningful for determining transition points that may not have large changes in amplitude and curvature. This may be the case for proteins with low intrinsic fluorescence when using nanoDSF or for transitions that do not result in major conformational or size changes but minor changes in global folds as is the case for the intrinsically disordered protein tau. However, this evaluation of onset points depends on establishing a percentage threshold value that determines which change in signal is deemed relevant - a factor that may vary from system to system.

In order to evaluate large data sets that feature more nuanced transitions, a generally applicable method is required. This chapter explores the use of trace-shape parameters derived from an unsupervised learning method. This technique is applied to phase separation systems as a demonstration of how evaluating shape parameters derived from principal component analysis can be a powerful supplementary data analysis tool.

3.2 Principal Component Analysis

Principal Component Analysis (PCA) is a technique widely used in multivariate statistical analysis, to increase the interpretability of data sets with multiple governing variables. The method involves reducing the dimensionality of the data set, from n variables into a subset of orthogonal uncorrelated variables which describe the variance of the data set as a whole. This is done by projecting the data set onto a lower dimensional space using eigenvectors of a covariance matrix [158]. For simplicity, consider the data set in Fig. 3.2 **a)**, in which data points are plotted on two primary axes, x and y. The first principal component, or plane onto which data points must be projected, is chosen such that the distance between the point and the plane is minimized. In so doing, the direction of this principal component is along the direction of greatest variance. The second principal component, which is required to be in a direction completely uncorrelated to the first, will then represent the direction with the next highest amount of variance. The process can be continued until the number of the principal components used can sufficiently represent the majority of trends in the data set.

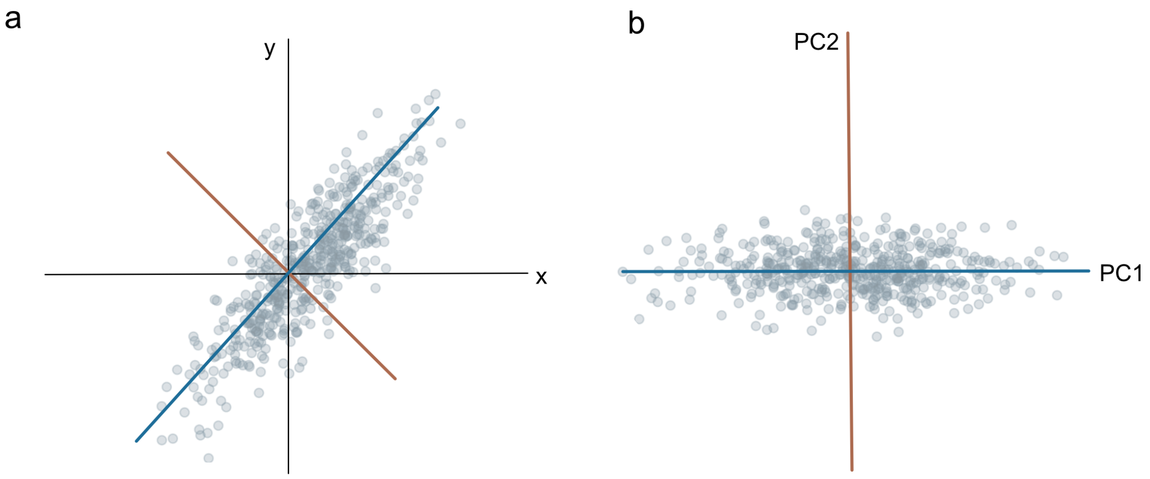

Figure 3.2: a) shows the projections of a 2-dimensional data set onto 2 perpendicular 1D lines, in the directions of maximum variance. Dotted lines represent the distance to be minimized . **b)** The lines in **a** represent the principal components.

The method essentially described the transformation of a high-dimensional $m \times n$ matrix X onto a lower-dimensional matrix Y such that Y=XV. In this equation, Y represents a $m \times m$ matrix and V a $n \times m$ matrix. Dimension reduction is commonly performed through a technique called Eigenvalue Decomposition (EVD), which involves the eigendecomposition of the covariance matrix C -which contains the information on the variance of the total data set X. The covariance C of the matrix is calculated by multiplying the data set by its transpose i.e. C=$X.X^T$. The second step is the calculation of the eigenvectors $v_1, v_2, v_3, ..$ and eigenvalues $\lambda_1, \lambda_2, \lambda_3, ..$ of the covariance matrix such that $C = W\lambda$. At the end, a linear combination of orthogonal variables is attained, which describes the maximum variance in the data set such that each eigenvector **v** - or principal component- and its associated eigenvalue λ -or weighted coefficient- quantify the magnitude and direction to which the original variable is represented.

$$\mathbf{C} = \sum_{i=1}^{n} \lambda_i \mathbf{v}_i \tag{3.1}$$

The eigenvectors obtained from the covariance matrix are then sorted with those having the largest eigenvectors being ranked as those representing the most variance in the data. These eigenvectors are now projected onto a new reduced dimensional space, with each eigenvector representing an orthogonal direction. For instance, the first principal component is a line on which the data points of X can be projected in a least squares sense. The new coordinate on this line is called a score. When the second principal component is plotted this will represent a direction orthogonal to the first component and as such represents the second eigenvector with the scores being the second largest eigenvalues.

Another way to perform dimension reduction is through single value decomposition (SVD), which is a more generalized and computationally easier version of EVD for square matrices. The single value decomposition of X is derived from the following equation,

$X = USV^T$ where U is also an $m \times n$ matrix, S is a $n \times n$ diagonal matrix, and V^T is a $n \times n$ matrix.

$$\mathbf{X} = \sum_{i=1}^{n} \mathbf{u_i s_i v_i}^T \tag{3.2}$$

The columns of U form an orthonormal basis for the fluorescence traces and are termed the left singular vectors $\mathbf{u}_i$. Meanwhile, the rows of V^T contain the elements of the right singular vectors $\mathbf{v}_i$. Lastly, S is comprised of a matrix with the non-zero values only on the diagonal - which are called the singular values. Typically, if the matrix X was centered, then eigendecomposition of $X.X^T = V^T$, resulting in the right singular vectors being equal to the principal components. Fig. 3.3 shows the workflow for each of the dimensional reduction methods, used in PCA, and summarizes each of the mathematical steps to transform the data matrix X onto a lower dimensional space. At the end the variance of the data set as a whole should be equal to the variances of the reduced space and the original data can be fully recovered from the lower dimensional projections from $X = YV^T$ [159].

3.2.1 PCA for Traces

Data represented as smoothed curves or functions can be evaluated using PCA, and can be applied to analyzing continuous functions obtained from interval based fluorescent measurements. As such the output of the PCA analysis are continuous eigenvectors, each of which have a corresponding eigenvalue. For the evaluation of thermal shift and nanoDSF measurements, each of the n condition tested is represented by a function of fluorescence ratio and temperature. The collection of data points in this curve is stored into a matrix $n \times f$. If this data is transformed into a lower dimensional space with PCA, the principal component directions correspond to those curves which represent the main variances of the data set. By projecting along these principal component directions back to the higher dimensional data space, we can recover curve "modes" which can be used to represent the experimental curves quite accurately. The PCA component value (or linear fit coefficient) of a mode for an experimental curve corresponds to the relative importance of that mode in describing that curve's shape. If a given mode corresponds to a clear physical parameter, e.g. droplet size, it can be used as a qualitative description of that parameter for a given experimental data trace.

3.2.2 PCA in Python

In this work, the PCA function in the *scikit-learn* [160] package in Python, is used, which uses a 'fit and transform' method. In *scikit-learn.decomposition*, PCA is used as a transformer object that learns a certain number of components in its **fit** method, and then transforms it into a reduced data set. After a data set is loaded into the PCA class, it centers the input data set, after which single value decomposition is applied. The fit step allows the data to be analyzed prior to transforming the data set into a new matrix. The projection of the data set onto the components is done, which results in a new reduced

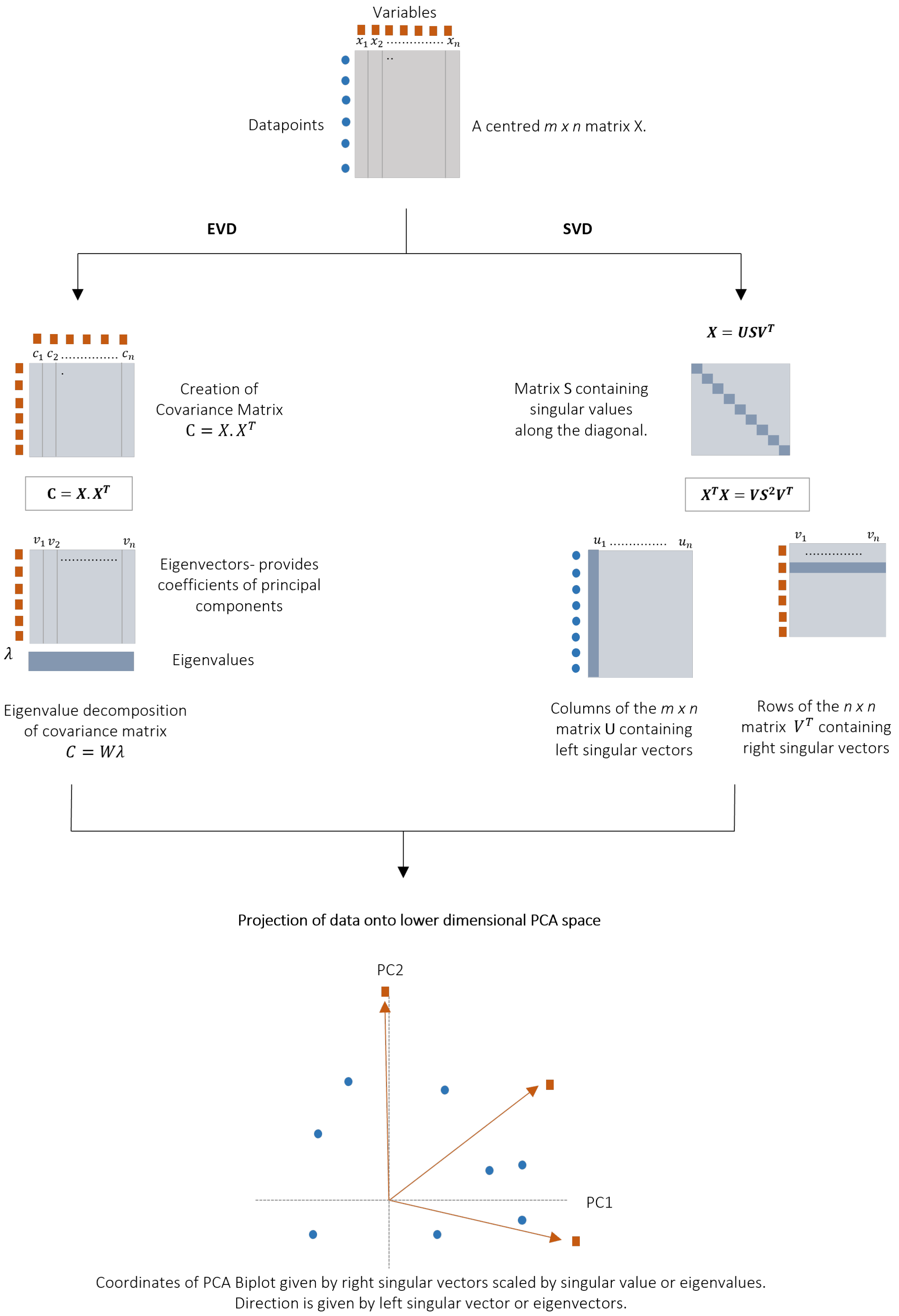

Figure 3.3: Comparison of EVD and SVD for PCA

matrix. The output is an array in which the number of rows, is the number of principal components evaluated, and the number of columns describes the number of traces (or unique variables) analyzed i.e. the length of the input dataframe. The following is a breakdown of the main computational steps and its implementation in Python.

Firstly, the raw fluorescent traces extracted from the file format "example.pan" from Panta Control software, is loaded into a dataframe **pca_for_curves**. An empty matrix X of appropriate dimensions is created and populated with the input traces to be analyzed. This is done by iteratively assigning variables from the input data into the corresponding row of X.

```

curves_for_pca = df.traces
X = np.zeros((len(df), len(curves_for_pca[0])))
for idx in range(len(df)):
    X[idx, :] = curves_for_pca[idx]
```

Listing 3.1: Preparation of input dataframe

The number of principal components is defined, by the variable **n_comp**, and is chosen by ascertaining how many components represent more than 90% of the variance in the data set. The PCA object is then initialized using the number of components specified. The output of this object is stored in the matrix **pca**, which is then used to perform PCA on the data stored in X. An identity matrix A is created, after which the inverse transform of A using the PCA object. The variable **X_trans** thus stores the dimension-reduced PCA data set.

```

n_comp = 4
n_plot = int(np.ceil(np.sqrt(n_comp)))
pca = PCA(n_components=n_comp)
pca.fit(X)
A = np.identity(n_comp)
X_trans = pca.inverse_transform(A)
```

Listing 3.2: Generation of PCA components

A linear regression model is used to fit the principal component data to the original trace data. The predictions of this model are stored in the **fits** array. The linear regression fit on the inverse transformed data obtained from PCA represents the loading or weighted coefficient for each principal component, and will thus output a number that ranks the importance of each component in describing the variance in the original data set.

```

fits = np.zeros((len(df), n_comp))
for idx, trace in enumerate(curves_for_pca):
    reg = linear_model.LinearRegression()
    reg.fit(X_trans.T, trace)
    y_pred = reg.predict(X_trans.T)
```

```python
    fits[idx, :] = reg.coef_
for idx in range(n_comp):
    df[f"pca_comp{idx+1}"] = fits[:, idx]
```

Listing 3.3: Fit method to generate PCA loadings

3.3 Analysis of temperature dependent phase transitions

In this section, a well established phase transitioning system will be analyzed to demonstrate the applicability of both the typical inflection point determination, ideal for sharp transitions observed in this system as well as the supplementary information derived from PCA. The system has been reported by Liu et al [119] and consists of a metal dependent phase separation ssDNA system, with two known transition points. As described in the work by Liu, this Poly A system demonstrates a first cloud point temperature, after which it forms dense DNA nuclei and a second transition point in the maturation phase with droplet formation. This system was initially evaluated with turbidity measurements and this work will also demonstrate the novel application of spectral shift to accurately characterize phase separation processes.

The cloud point temperatures were seen to be dependent upon the level of Ca^{2+}, with higher ionic concentration leading to decreasing nucleation transition point T1. Fig. 3.4 shows the results of **a)** spectral shift assay and **b)** thermal DLS ramp, performed on the Andromeda and Prometheus Panta instruments (NanoTemper Technologies GmbH). For the spectral shift experiment, the Poly A ssDNA is labeled with a Cy5 fluorophore, and diluted in buffers with varying levels of CaCl. The two-step transition is seen clearly, with the cloud point T1, decreasing from 60.4 °C to 28.4 °C and T2 changing slightly from 77 °C to 75 °C (Fig. 3.4) when increasing the Ca2+ concentration from 10 mM to 200 mM, agreeing with previously reported absorbance turbidity measurements.

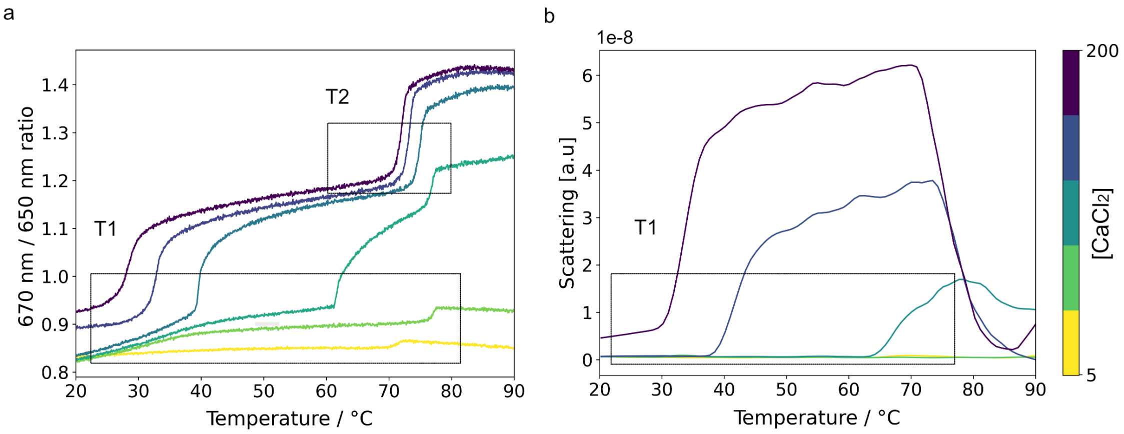

Figure 3.4: a) A thermal spectral shift assay performed monitoring spectral shift ratio over a temperature ramp of 1°C / min, reveals a two-phase transition Poly A LLPS system. Two transition points T1 and T2 can be observed, each of which shows a decrease with increasing Ca2+ levels **b)** Dynamic light scattering measurements allow indirect measurement of droplet formation over a thermal ramp. Scattered light indicates the metal ion concentration dependence of T1 and saturation past T2.

Similar trends are also seen in the DLS data, for which the scattering intensity is plotted over temperature as seen in Figure 3.4. The scattering counts are reliable until 74 °C, after which large particle size render the DLS detector oversaturated by scattered light. Since this sample has two distinctive transition points, which can be determined via the inflection points, it is possible to evaluate this data simply.

This system, where we only vary one experimental parameter, can be analysed simply using PCA. However, this system is only evaluated for the effect of the ionic strength on each transition point and may become easily more complex, if different ions, chain length, or other phase determining behavior were to be screened. As such it is interesting to evaluate this system using PCA in order to identify the variances in the shape of the traces and determine which components influence the first and second transition points. Fig. 3.5 **a)** shows the first four principal components which describe the main variances in the data set. As such the traces shown in Fig. 3.4 **a)** can be decomposed into four main shapes which together account for changes in transition points T1 and T2. Whilst PC1 and PC2 seem to determine the amplitude of the signal and length of the growth phase respectively, PC3 and PC4 are more heavily influenced by the nucleation phase. If PCA is used to just evaluate the position of the T1 and T2, the nucleation phase for lower Ca^{2+} can be classed as a T2. However, this system does show a valuable feature extraction in the identification of curves with either one or two transition points, which is shown in Fig. 3.5 **c)**, which allows this classification to be visualized in a plot of PCA1 and PCA3. For example, the first and second transition curves can be separated with PCA 1 and 3 because PCA 3 has a steeper slope to the second transition like the high CaCl concentrations, and it has a negative value in the case of the low CaCl concentrations because subtracting the PCA 3 curve from the PCA 1 curve gives you a flatter curve. The points at the top left corner are lower salt concentrations whilst those at the bottom right show the higher salt concentrations which show two transition points. This feature of PCA analyses can be useful when applied to a bigger dataset. Variations to this algorithm will be highlighted in the next section.

3.4 Potential progression of PCA algorithm

PCA has been used as a method for decomposing complex data in a variety of fields ranging from genomics [161], spectral analysis [162] and molecular dynamics [163]. In each case, the method has been used to successfully denoise data, extract dominant features in a data set, and reduce the dimensionality of multivariate systems. The application of PCA in this work has provided a novel avenue for pattern recognition in a data set, by evaluating trends in curvature to output shape parameters. Since the method is robust, it has the potential to be applied to different data sets, for which the outcome is to either 1.) determine the main variances and thus curve shapes in the data or 2.) estimate the variation of a single component in a large data set. As such the algorithm may be improved depending on which use and system to which it is applied.

There are two main avenues for which the algorithm developed in this work may be modified. The first is through the use of functional PCA, a variation of the algorithm

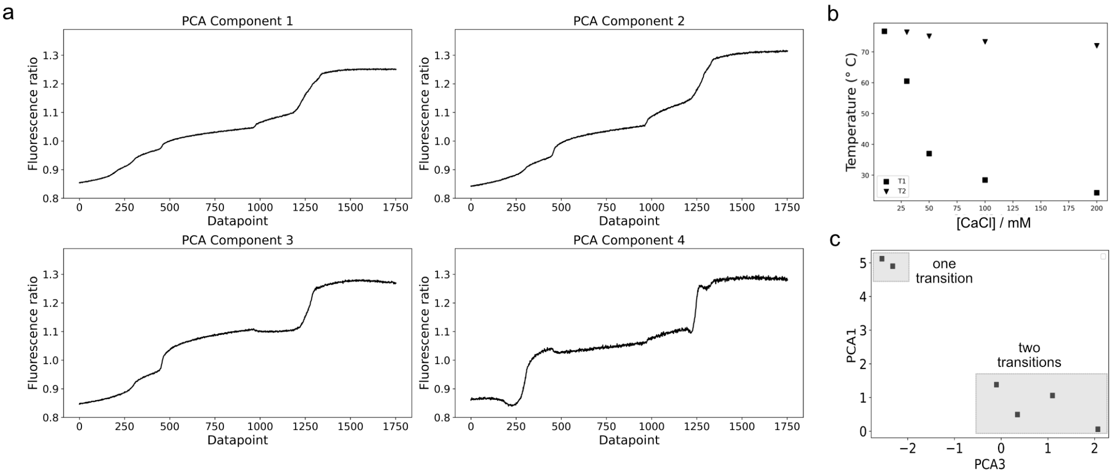

Figure 3.5: a) Traces from the thermal shift assay of the Poly A ssDNA LLPS system can be decomposed into four main principal components in which PC1 and PC2 describe the second transition point and PC3 and PC4 describe the first transition point. **b)** The onset temperatures are plotted against CaCl concentration for each transition T1 and T2. **c)** The principal components, when plotted against the related assay conditions, indicate a relationship between the onset transition temperatures and the principal components determining the inflection points of the trace

used in this work. Since curve traces are already the input set, the output of PCA would not only just be the shape parameter, but a smoothed eigenfunction that describes the composition modes of the trace as polynomials as is reminiscent of Fourier analysis. This offers an even more quantitative approach but is harder to implement for a novel system for which little is known. Another approach to evaluating traces can also be borrowed from shape analysis. In this framework, the data set is divided into discrete coordinates, termed landmarks. However for this method to work, landmarks for an average shape must be defined in a vector space. Then Procrustes analysis is used to characterize the coordinates of each trace as a factor of variance from the average shape [164]. This step also allows the comparison of a new data set in a large screen to shapes that have already been identified as the main modes of a data set. This is particularly useful for sorting data into groups, and for outputting a descriptive classification.

Apart from modification using either of these approaches, PCA is most commonly used as a basis for machine learning techniques which must be trained on large data sets, and is the primary advantage for using this form of dimension reduction technique. The main limitation of PCA, in any of its applications, is the presence of the interpretation step, when identifying the components of importance. This is also the case for the application of shape parameter based learning methods for any of the uses identified in references [159, 161–163]. This step can only be circumvented by training a model using a much larger data set, for which the model can learn to identify the most important components. In this case, the method becomes a supervised learning method. Thus this approach whilst is used extensively to characterize trends in a data set, has already provided a major proof of concept for its applicability to evaluating trends in fluorescence traces, and can be used as a framework for more complex modes of analyses.

Chapter 4

Liquid liquid phase separation

Tau is a stable, microtubule-associated protein that is primarily located on axons of neurons in the central nervous system. In addition to its main physiological function of stabilizing microtubules, tau can also be found in the unbound state in which it can interact with various biomolecules such as enzymes [22], actin filaments [165], DNA [166], and tRNA [78]. However, the intracellular concentration of this unbound tau is only approximately 1-10 nM [167]. How tau transitions from its physiologically stable and soluble state to pathogenic filamentous inclusions is a process that has yet to be understood [168]. Thus, mechanisms by which proteins can be recruited into assemblies that increase their local intracellular concentration past their solubility limits have become of critical interest in the field of neurodegenerative disease research.

Tau has recently been identified as one of the several intrinsically disordered proteins that undergo the physiochemical process of liquid-liquid phase separation, in which transient multivalent interactions recruit biomolecules into a high-density phase, forming biomolecular condensates [169]. The formation of biomolecular condensates as a means of compartmentalization of molecules was first identified in a study characterizing the formation of p-granules, which are micron-sized organelles capable of concentrating protein and RNA necessary for regulation of transcription in germ cells [170]. These granules exhibit liquid-like mobility and viscosity, with the ability for proteins to freely diffuse into and out of the cytoplasm, be deformed by shear force, as well as undergo fusions and fission [171].

Since this initial discovery, many membraneless condensates have been shown to serve a variety of functional roles in the cell, ranging from facilitating DNA repair [172], signal transduction [171], and stress response via granule formation [173]. Liquid-liquid phase separation (LLPS) is widely accepted as the process that leads to the formation of these localized and mobile droplets, with the distinct increased concentration within the condensate representing a phase boundary [17]. The selective sequestration of molecules allows condensates to impact biochemical processes in a variety of ways including control of reaction kinetics by up-concentrating molecules [174], regulation of specificity of reactions by excluding competing interaction partners [175], and precise control of function of its constituents due to the sharp transitions to and from a droplet state. However, even though the formation of some condensates is highly regulated, aberrant formation of such condensed phases through a misregulated response to environmental signals has been widely associated with deleterious effects, especially in the case of neurodegenerative diseases [176, 177]. Understanding the process of biomolecular condensation may aid in elucidating intermediate pathways in amyloid fibril formation and subsequent aggregation, processes that rely heavily on orders of magnitude higher local concentration of molecules within the dense phase to explain the eventual liquid-solid transition (see Fig.4.1).

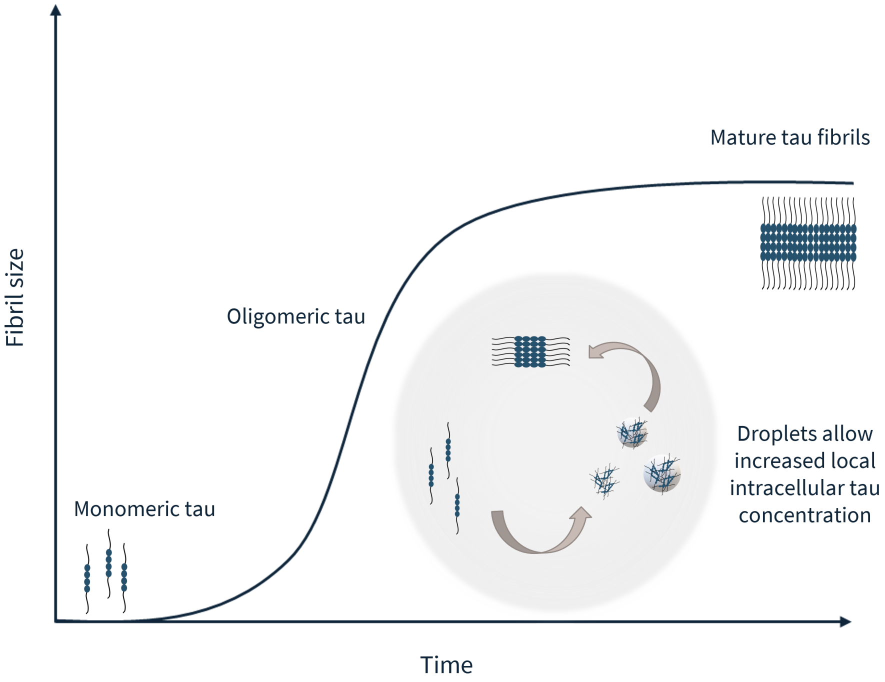

Figure 4.1: Tau is an intrinsically disordered protein that forms filamentous aggregates seen in Alzheimer's disease. Liquid-Liquid phase separation of tau is proposed as a mechanism to explain the formation of small oligomeric species.

LLPS relies on the concept from polymer science that multivalent molecules undergo self-assembly upon mixing, and in so doing decrease their solubility. Multivalency of a molecule refers to its ability to participate in multiple forms of weak, nonspecific, inter, and intramolecular interactions. These interactions promote polymer-polymer interactions over polymer-solvent interactions, and its decreased solubility increases its propensity to phase separate [74].

This concept can be extended to certain intrinsically disordered proteins that are flexible multivalent molecules with a heterogeneous charge distribution. The interactions that promote this self-organization process range from electrostatic charge-charge interactions, dipole-dipole interactions between charged side chains and the protein backbone, and hydrophobic interactions. Thus, it becomes imperative to determine not only conditions that may exist in a physiological environment but also pathological triggers that result in an increased propensity for phase separation.

4.1 Modulating valency of phase separating proteins.

4.1.1 Sequence determinants of LLPS in IDPS

Phase separation is largely governed by a molecule's valency, which promotes protein-protein or protein-polyanionic cofactor interaction. There are several properties of intrinsically disordered domains that are correlated with the propensity for LLPS. First, there is the presence of low-complexity domains (LCD); regions that have low amino acid diversity relative to the proteome [177]. With low diversity, there is often a bias in amino acids, where the protein is enriched in different ways, for example with glycine in TDP43, serine in hnRNPS, or tau with proline. LCD interactions have received the most experimental attention to date, in part because of the frequency of disease-causing mutations found within these domains [178, 179]. These mutations allow homologous interactions between molecules with modular, repeating, positive, and negatively charged regions, or proteins consisting of repeating sequence motifs [21]. This is the case for RNA-binding RGG motifs, found in FUS proteins, or RNA recognition motifs (RRM) in the TIA-1 protein [180]. Such sequence compositions allow for some of the main multivalent interactions that promote phase separation, including dipole–dipole interactions, π-stacking interactions, cation-π interactions, and charge–charge interactions [181]. Charge-charge interactions are usually interactions between charged side chains and the protein termini. The overall charge of a protein is modulated by pH, allowing proteins with a very high or low pKa to undergo phase separation more easily [177]. Cation-π and π-π interactions typically occur between arginine and tyrosine residues and are also prominent within both proteins and nucleic acids, particularly with single-stranded nucleotides as unfolded nucleic acids have their aromatic nucleotide bases exposed. Each of these transient interactions may allow the self-assembly of these proteins and the subsequent formation of condensates as seen in Fig. 4.2.

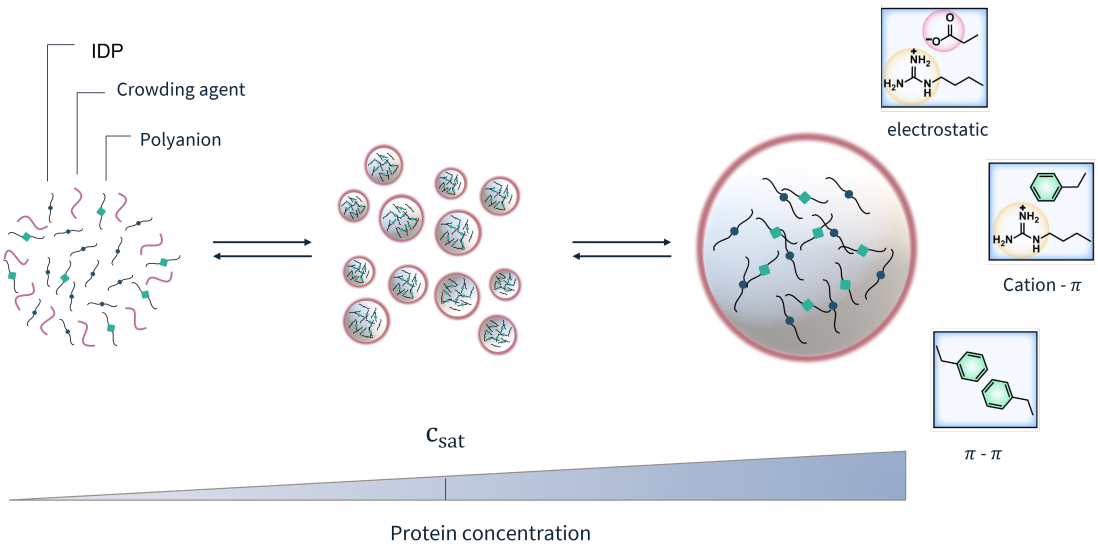

Figure 4.2: LLPS is governed by transient multivalent interactions which allow self-association of a biomolecule, or to another charged molecule. Such interactions allow proteins such as IDPS in the monomeric form to transition into a dense phase after a critical concentration is reached. The main interactions involved in modulating IDP LLPS are shown on the right.

4.1.2 Specific properties of tau lead to phase separation.

Tau’s lack of secondary structure and the heterogeneous charge distribution along the full-length tau promote the multivalent weak interactions leading to LLPS. The N-terminal and the first 120 amino acids have a net negative charge; while the central proline-rich domain (amino acids 151-243) and MTBR (amino acids 244-369) have a net positive charge and the C-terminus (amino acids 369-441), a net negative charge (Fig.4.3 **a) - b)**).

A further critical regulator of protein phase separation is the occurrence and frequency of post-translational modifications. IDPs are more prone to such modifications, as the disordered structure exposes more residues to acetylation, phosphorylation, and methylation; modulating the effective valency of the protein [182]. There are several regions in the tau sequence that may be key in modulating its overall valency. For example, positively charged lysine, which accounts for 10% of the tau amino acid sequence, can be altered by acetyltransferases, altering the total charge and subsequent protein interactions [183]. The proline-rich region also holds the most phosphorylatable sites in the sequence because it includes a large number of serine, threonine, and tyrosine residues. Another key factor for tau LLPS is the presence of the aggregation-regulating hexapeptide motifs VQIINK and VQIVYK, which are found in the microtubule binding region (MTBR). The MTBR is susceptible to mutations (for instance, P301L, N279K, or V337M), which all alter the valency of the protein. This region can greatly impact the self-associating properties of tau, with evidence pointing to it being a viable nucleation site for the LLPS process, with the K18 MTBR fragment showing a high propensity for phase separation [184].

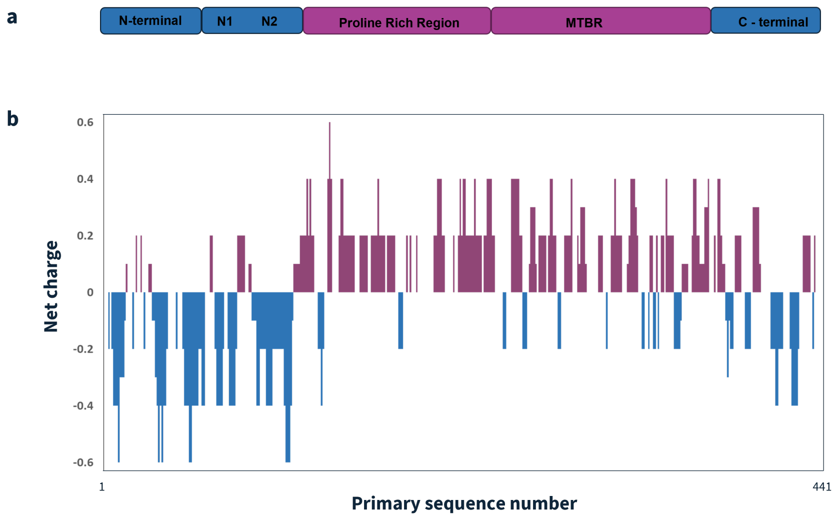

Figure 4.3: Charge heterogeneity displayed in relation to the amino acid sequence of tau, generated by CIDER[185]. The MTBR and proline rich region display a net positive charge, with the N and C terminals and inserts have a net negative charge.

The simple coacervation of tau is promoted by electrostatic or hydrophobic interactions, both of which can be observed under pathological conditions. For example, hydrophobicity is increased in hyperphosphorylated proteins. Studies have often used salt concentrations far from physiological conditions with the aim of mimicking the effects of pathological conditions such as increased hydrophobicity of phosphorylated tau [176], charge screening due to post-translation acetylation [165], enhanced intracellular osmotic crowding pressure, as well as certain pathological mutations of tau discussed in section 1.2.1. Ionic strength is an important modulator in regulating the formation of liquid droplets. Neutral or kosmotropic salts in the Hofmeister series such as NaCl, with high concentrations promoting hydrophobic interactions between proteins producing a salting out effect [186]. Water is sequestered away from protein molecules, which then amplify its hydrophobic self-association. Similarly, low salt concentrations can also be used here to reduce the effect of electrostatic screening and allow for the interaction of charged domains within the protein. To further mimic the cellular environment, the use of crowding agents such as PEG, dextran, heparin, or ficoll has also been used to promote the interaction of proteins [74, 187].

4.2 A multiparametric optical approach to studying LLPS

To monitor liquid-liquid phase separation, either *in vitro* or *in vivo*, there is a strong reliance on macroscopic detection techniques. This is largely sufficient to detect the presence of micrometer-sized droplets but does not give enough detail on the processes of nucleation and clustering, precursors to visible droplet formation. Currently, the main techniques for observing LLPS use a variety of microscopy techniques for visualizing the droplets, as well as the use of turbidity and sedimentation assays to determine cloud points for temperature-dependent phase transitions. In this work, intrinsic and extrinsic fluorescence spectral shifts are introduced as methods to monitor temperature-dependent phase transitions of proteins and labeled biomolecules, respectively as discussed in Chapter 1. Furthermore, the supplementary methods of data analysis introduced in chapter 3 will be used to greatly improve the scope of the technique by allowing trends in high-throughput screens to be easily identified. This signal is complemented by dynamic light scattering, which detects the formation and maturation of protein droplets on a macroscopic scale. The conditions selected in the high-throughput assay for optimal LLPS conditions are validated by visualizing droplets via confocal microscopy, which further supplements the data on droplet size and growth over time. Recently, there have been more techniques looking specifically at the conformational changes of proteins during phase separation. Majumdar et al, showed using a pyrene-based proximity probe, that tau K18 fragment undergoes a conformation change from a more compact to extended structure during the phase separation process [188]. Similarly, single-molecule FRET and fluorescence correlation spectroscopy performed by Wen et al, was used to look at interdomain interactions of tau in native and LLPS conditions. The study showed conformational changes as a consequence of LLPS, with changes of Förster radius indicating the native paperclip fold being unraveled as the N and C terminals extended away from the MTBR region [77]. Both techniques require mutagenesis for site-specific labeling of the protein at each termini, but provide valuable information on the dynamics of tau during phase separation. With nanoDSF the protein does not need to be labeled, with just the intrinsic fluorescence of the tyrosine and protein backbone used to monitor phase separation at a conformational level, before and after the transition.

4.3 Simple coacervates of tau

The thermoresponsive behavior of proteins depends greatly on the type of interaction that guides the phase-separation behavior. For instance, in LLPS promoted by hydrophobic interactions, entropic contributions hold more importance, resulting in lower critical solution temperature (LCST) transitions. This means that droplet formation is promoted at higher temperatures, where entropic rearrangement of solvating water molecules results in a reduction of the solubility of protein. However, this is not the case for transitions driven mainly by electrostatic interactions, which instead exhibit an Upper Critical Solution Transition (UCST). Hydrophobic interaction-driven LLPS can be mimicked by using a high-salt system, whilst full-length tau and the K18 fragment have been reported to undergo electrostatically driven phase separation in low salt conditions [189, 190].

To perform LLPS screens of simple coacervates, 20 μM full-length tau in LLPS buffer (20 mM HEPES, 2 mM DTT, pH 7.4) in the varying salt concentrations as described in Section 2.5.2. The mixture was stored at 4°C to prevent droplet formation and then loaded into the Prometheus Panta device for measurement. The solution was then heated at a rate of 1°C / minute from 15-55 °C. To display the ionic strength-dependent phase separation of tau, firstly a low (10 mM NaCl) and a high (4 M) condition, were measured. The dual measurement of intrinsic fluorescence ratio (IFR) and DLS are displayed in Fig. 4.4 which demonstrate the different transitions of tau. IFR indicates onset of conformation changes in the protein at around 38.5 °C, for the LCST exhibited by the high salt system, whilst the low salt system shows a UCST, with droplets forming below 47 °C (Fig. 4.4 **a)**). This information is then further described by DLS data (Fig. 4.4 **b)**), which indicate mesoscopic clusters of protein, which are precursors to visible droplet formation. Wegmann *et al.* have reported similar precursors to droplet formation, with dynamic light scattering on tau LLPS systems [187]. Together, the data provide evidence of conformational changes during this clustering process.

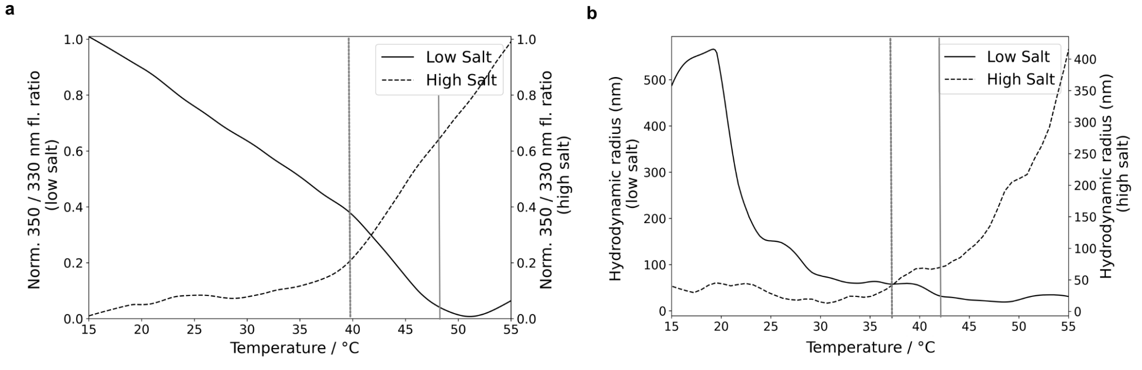

Figure 4.4: nanoDSF and DLS traces demonstrate the context-dependent phase transitions of tau. a.) A thermal ramp at 1 deg/min shows 20 μM full-length tau in LLPS buffer undergoes a Lower Critical Solution Temperature in the presence of 4M NaCl while in the presence of 10 mM NaCl an Upper Critical Solution Transition can be observed. b.) the size of precursor droplets is measured for each condition using dynamic light scattering.

Confocal microscopy was also employed to visualize droplet formation in simple coacervates. First, the LCST of the high salt system was investigated by performing a thermal ramp on using a temperature-controlled stage as described in Section 2.5.3. Fluorescent clusters were not visible until 39 °C, however, the nuclei observed were still below the resolution limit of the microscope (Fig.4.5 **a) - e)**). After increasing to 41 °C discernible droplets were observed, with the size and number of droplets increasing with temperature. The average area of droplets was estimated for three sample populations, in order to estimate droplet growth as seen in Fig. 4.5 **g)**. The average size of the droplet is determined from these measurements.

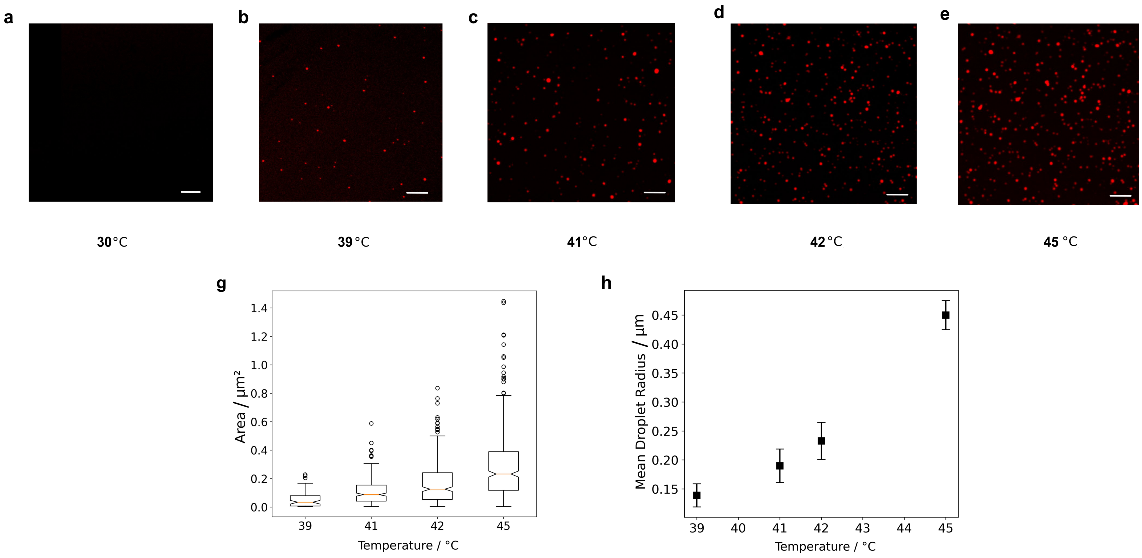

Figure 4.5: A LCST transition is demonstrated using 20 µM full-length tau in LLPS buffer, and 4M NaCl. **a)-e)** Micrographs showing nuclei formation over a temperature ramp between 39 - 45 °C. **g)** The area of each droplet is measured over three sample populations. Box plot represents the distribution of sizes, with the error bar indicating the standard deviation from the mean. **h** The average droplet radius is determined for the three sample populations. Error bars represent the standard deviation n=3. Scale bar = 5 µm.

Next, simple coacervates of tau were examined under low salt conditions as shown in Fig. 4.6. As tau undergoes an Upper Critical Solution Transition (UCST) (Fig. 4.4), experiments were carried out at room temperature, as cooling was not possible using only a temperature stage. Droplets formed immediately after mixing (Fig. 4.6 **a)**) with the number of droplets increasing over time, with only a moderate increase in size (Fig. 4.6 panels **b)** and **c)**. As mentioned in Section 4.1, the dynamics of molecules within the dense phase informs the nature of the biochemical processes that can occur. To assess the dynamics of the protein within the dense phase, fluorescence recovery after photobleaching (FRAP) measurements were performed as described in Section 2.5.3. A stationary droplet of size ranging between 2 and 8 µm was chosen and a selected region of interest was bleached for a period of 5 seconds (Fig. 4.6 **j)**). The fluorescence recovery was monitored over a period of five minutes, with the increase in fluorescence in the bleached area representing any dynamic exchange of protein outside of the dense phase. Initially, the droplets were found to be dynamic and viscoelastic, as FRAP showed almost complete recovery (Fig. 4.6 **j**, dark red trace). Over time, the molecules become more glassy, and this transition occurs after 4 hours when the droplets only have 20 % recovery. The time taken to reach half the maximum recovery $t_{1/2}$, was found to be 120 s (t = 0), 103 s (t = 1 hour) and 78 s (t = 4 hours). The transition has been observed before in the literature with FRAP times ranging from 37 s - 200 s [74, 76, 191].

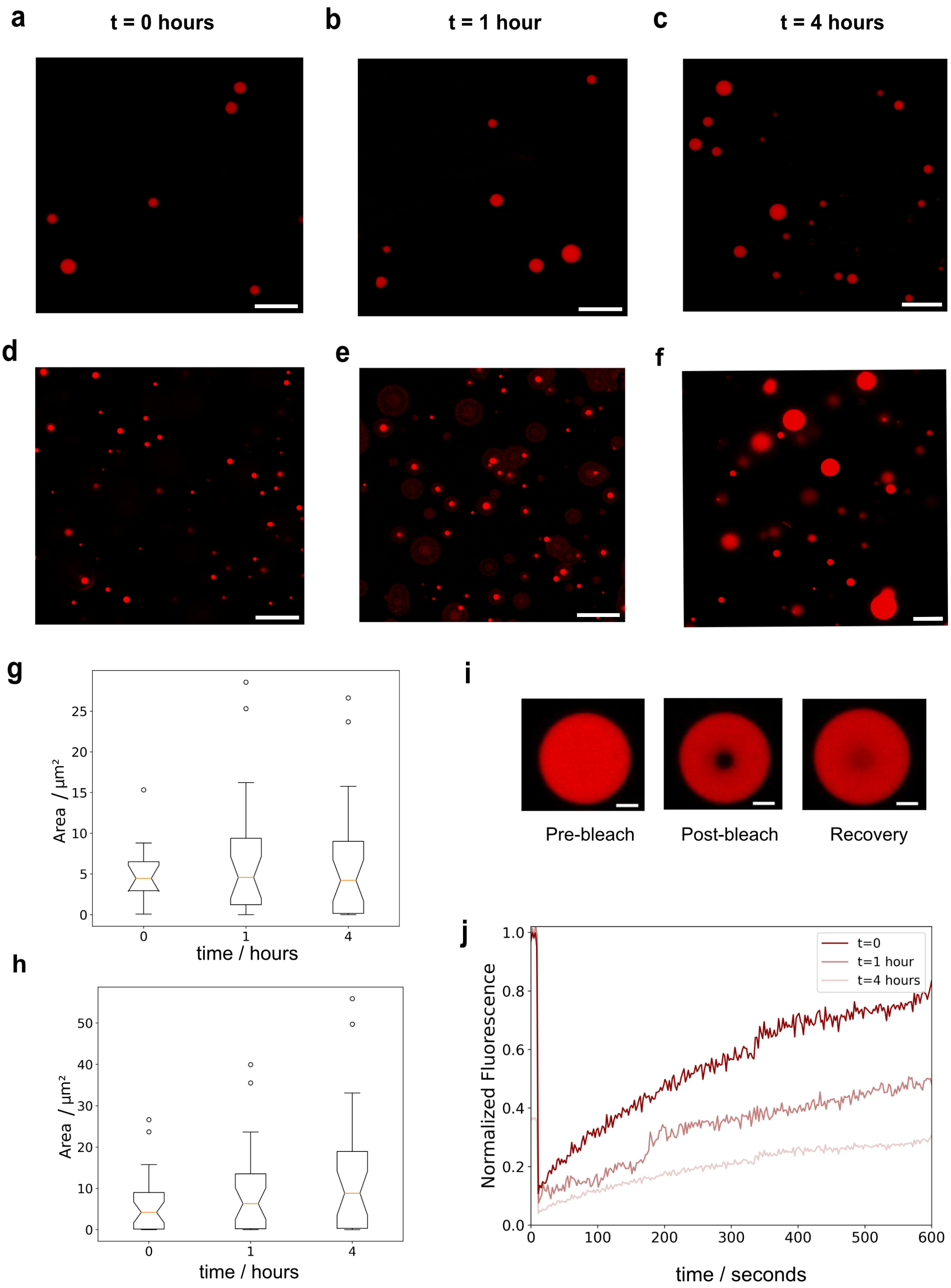

Figure 4.6: Micrographs in **a)** - **c)** show droplet formation over the first four hours for 20 µM tau (20 mM Hepes, 10 mM NaCl, pH 7.4), whilst **d)** - **f)** show the effect of crowding with the addition of 10% w/v PEG 8000. Scale bar = 10 µm. **g)** show the distribution of droplet surface area over time for the uncrowded sample **h)** show the distribution of droplet surface area over time for the crowded sample. Error bars show the standard deviation for measurement over three sample areas. **i)** Shows the selection of a region of interest, in the pre and post bleaching as well as recovery phases. **j)** FRAP measurements show the fluorescence recovery for the coacervates measured at t = 0, t = 1, and t = 4 hours. Scale bar = 2 µm.

The decrease in dynamics has been correlated with the formation of fibrillar structures, but it also suggests stronger transient interactions occurring over time in the droplet. Furthermore, low-salt conditions were also tested in crowded samples, where PEG is used to increase tau-tau interactions by excluding the volume in which they can associate. This effect was visible in the appearance of a protein corona around nuclei which are larger in size even at t = 0 (Fig. 4.6 **d)**). The number of initial nuclei was also much higher in the presence of PEG than in the system without crowding, with the number and size of droplets showing a greater increase over 4 hours (Fig. 4.6 **h)**).

4.4 Complex coacervates of tau

Many intrinsically disordered proteins implicated in neurodegenerative diseases contain RNA-binding domains or are able to interact with various polyanions. Therefore, the formation of complex coacervates is particularly relevant and of interest within cells. The formation of complexes with polyanionic cofactors leads to even stronger electrostatic interactions and can lead to significant changes in droplet growth and behavior [79, 189]. It is interesting to distinguish between the specific interactions of these proteins and the electrostatic interactions available through the multivalency of other polyanions [118]. Thus, a system of tau and polyadenylic acid (Poly dA) was used as a model system to monitor electrostatically triggered phase transitions.

In order to perform a small-scale LLPS screening on the varying conditions which affect droplet formation, complexes of tau and poly dA were formed at varying charge ratios of tau : Poly dA and salt concentrations varied between 0 and 150 mM NaCl. The aim was to determine the effect of the two main electrostatic forces driving the LLPS process. The Prometheus Panta was used to perform a thermal ramp, in a high-throughput manner of measuring 48 samples simultaneously. The tau (10 μM) and poly dA were mixed in LLPS buffer, and each sample was subjected to a thermal ramp at 1 °C/ min. Fluorescent ratio traces were evaluated using the PCA algorithm (see Section 3.2.2), with the main modes of curvature represented in the first two components of the PCA as shown in Fig. 4.7 **a)** and **b)**. Onset temperatures were determined by manually setting the threshold and were compared to the PCA component 2 which described the phase separation propensity of each condition the most accurately. From the PCA analysis, it could be seen that the charge ratio R = 1 showed the highest degree of droplet formation (Fig. 4.7 **d)**). Increasing salt concentrations suppresses droplet formation when using this charge-matched system (Fig. 4.7 **c)**). The results for ideal droplet formation were then verified by confocal microscopy.

Unlike simple coacervating systems, in the presence of crowding agents, both the tau and polyanion are localized inside the droplets. This can be seen in Fig. 4.8 which shows the dual-channel confocal image of Histag-labeled tau using the protocol described in Section 2.2.4 and Cy3-labeled polyadenylic acid. The composite image demonstrates the colocalization of both charged polymers within the dense droplet phase. To test the effects of various conditions on droplet formation in complex systems, we investigated the effect of charge ratio (R) between polydA and tau, followed by modulating the ionic strength

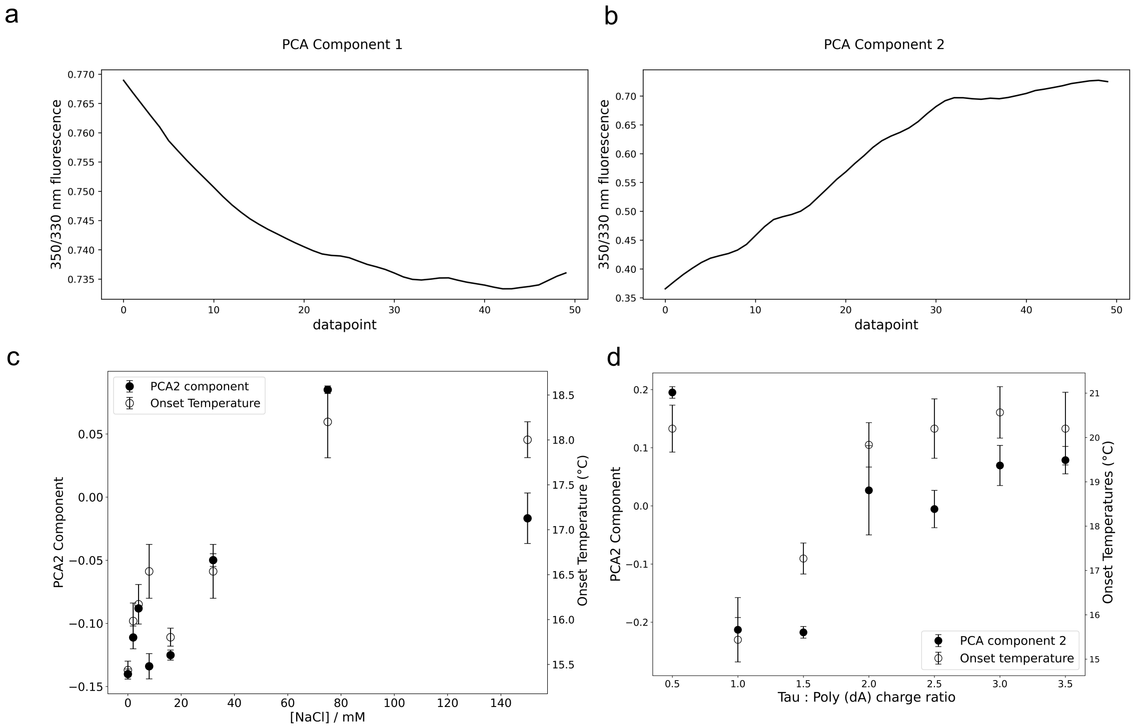

Figure 4.7: An LLPS screen for complex coacervates with a tau: poly dA system was performed by monitoring nanoDSF traces over a thermal ramp from 15-55 ° in 15 conditions. **a)** The LLPS screen uses 45 traces to produce PCA components that describe the main variances in the dataset. PCA components 1 and **b)** 2 are shown which describe over 77% of the variance. **b)** PCA 2 component describes the changes in the traces at the transition point and correlates with the onset data detected with a Pearson coefficient of 0.89. The PCA components are plotted over **c)** each salt and **d)** tau : poly dA charge ratio tested, to highlight trends in the LLPS behavior.

of the buffer. Droplet formation occurs most readily upon charge matching the system to R=1. When the charge ratio deviated to R=0.5 (Protein to Poly dA) and R=2, only a few droplets were seen and did not remain stable over time. Thus, the system in which charge ratio = 1 was monitored over a 4-hour period to measure droplet growth and stability. The complex system had an increase in the number and size of nuclei immediately after mixing, compared to the simple system. The growth of the droplets was approximately two times faster, with $t_{1/2}$ times reducing to 75 s and the droplet size reaching up to 8 μm after 4 hours.

Interestingly, even though droplet growth and fusion occurred rapidly in the first hour, the dynamic properties of the droplets showed a drastic decrease over time. FRAP measurements indicate a high degree of tau movement within the droplet initially, but after one hour, there is no FRAP recovery (Fig. 4.9 **e)**), indicating that the glassy transition occurs much more quickly. Many studies propose that this is as a way for highly tenuous structures within liquids to seek lower energy configurations [187, 191, 192]. Thus it is proposed that the propensity for low-complexity domains in proteins (such as tau) to undergo phase separation can be attributed to systems falling down a thermodynamic well. In a recent study by Tejedor *et al.* [193], the formation of inter-protein β sheets in the dense phase also produces another stable configuration, which has been shown to promote the glassy transition within droplets, with the presence of polyanions greatly

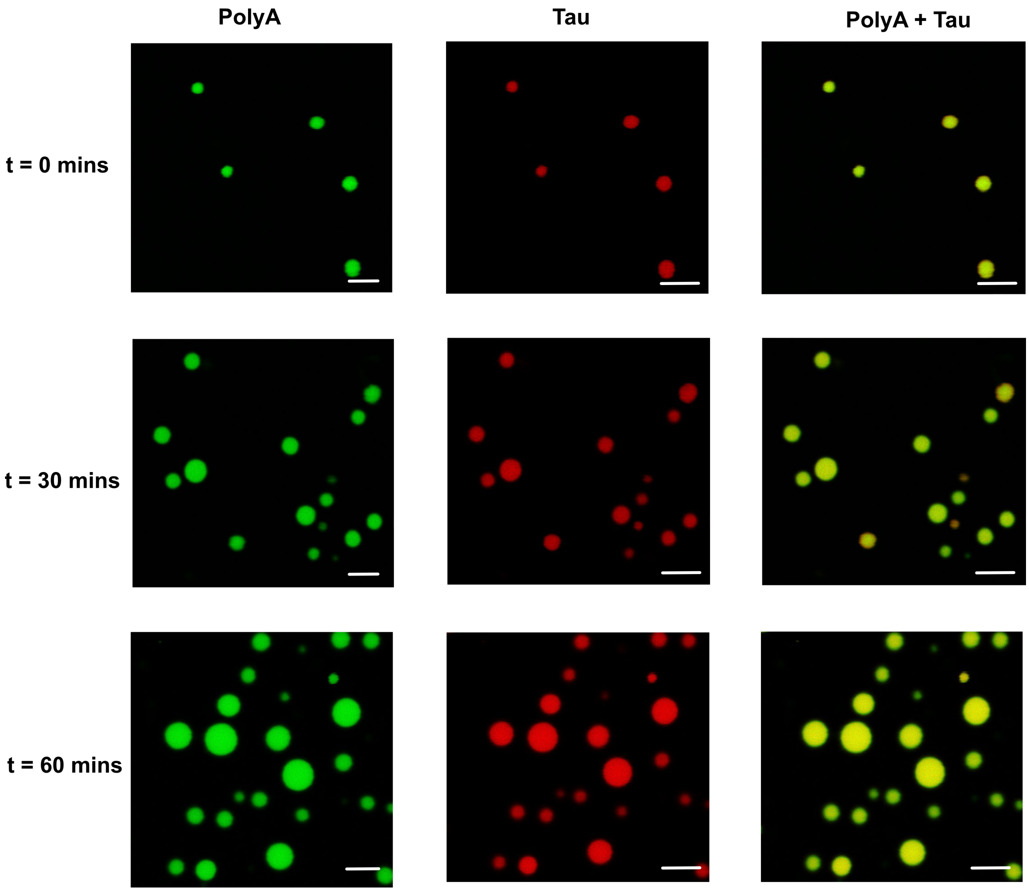

Figure 4.8: Confocal micrographs showing co-localization of 10 µM Cy 5 labelled Tau 2N4R and the Cy3 labelled Poly A single stranded DNA at R=1, in LLPS buffer (20 mM Hepes, 0 mM NaCl, pH 7.4). Droplet maturation is observed over an hour for the complex coacervate system. Scale bar = 5 µm.

increasing the extent of crosslinking, and the time scales in which they occur [194].

Another important electrostatic contribution is the influence of the ionic strength of the buffer. As shown in the nanoDSF results in Fig. 4.7, the addition of NaCl to the complexed system results in a reduced propensity for droplet formation, particularly at concentrations greater than 70 mM NaCl. The micrographs in Fig. 4.10 **a) - h)** show that not only does the addition of 10 mM NaCl reduce the initial number of droplet nuclei formed, but in conditions higher than 20 mM NaCl, droplets dissolve, and reform over a longer period of time. In 50 mM NaCl, droplet formation is completely hindered, and instead protein precipitates are visible in micrographs. The secondary plots in Fig. 4.10 **i) - j)** show the processed micrograph droplet area in detail, and show that the average droplet size increases the most for complexes that are not exposed to electrostatic screening.

Dynamic Light Scattering performed in parallel to nanoDSF experiments also show a similar trend for the decrease in droplet size upon addition of NaCl in solution. Fig. 4.10 **k)** show the raw scattering signal (a proxy for particle size) and the calculated hydrodynamic radius, respectively. Since measurements are performed immediately upon mixing, the values show the nuclei and the effect of screening their size. The scattering information also provides a more accurate representation of trends of larger droplets,

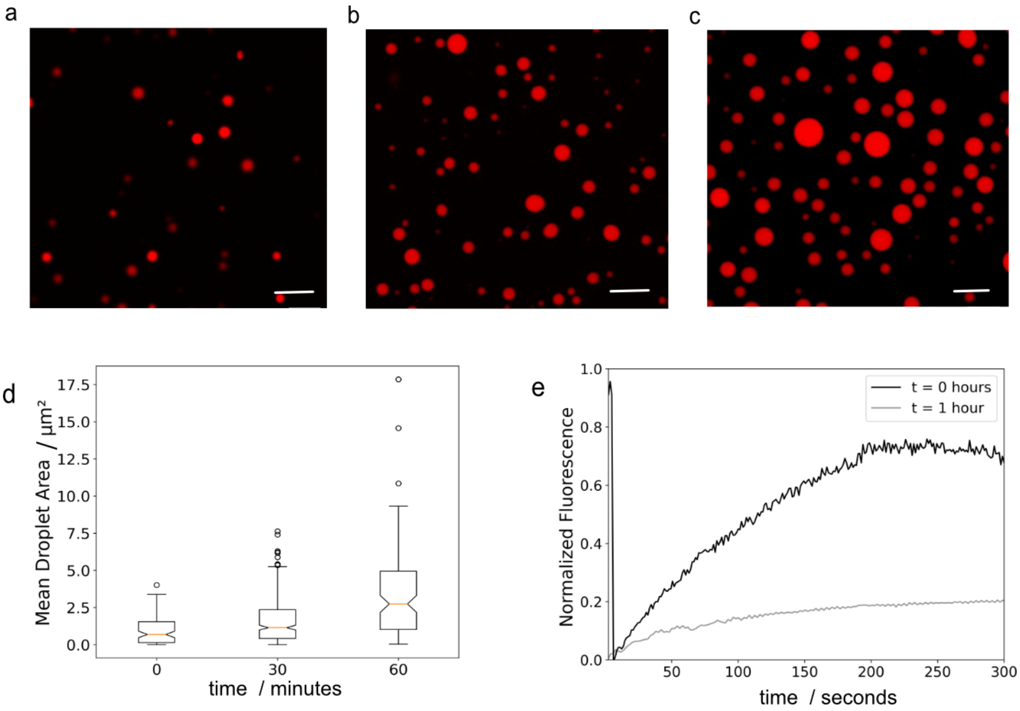

Figure 4.9: shows the growth of Tau: Poly dA complex coacervates over at **a)** t=0, **b)** t=30 mins and **c)** t=60 mins. **d)** - **e)** shows that the average size and polydispersity of droplets increase over time. **f)** FRAP of the droplets taken immediately after mixing and one hour later show a loss in viscoelasticity of the droplets over time. Scale bar = 5 µm.

which show a size greater than one micrometer and scatter light orders of magnitude greater. The fit used to provide the radius of hydration data also becomes less accurate for more polydisperse samples, especially those containing large particles.

Another important factor in defining pathological relevance of the LLPS process is determining the critical concentration at which phase separation can occur. To date in the literature, the lowest concentration used for bulk measurements has been 2 µM, and utilized GFP-fused tau constructs to perform confocal microscopy [191]. The GFP fluorescence was used to obtain linear regression of the calculated droplet area as a function of concentration. The study reported that 760 nM is the critical concentration for full-length tau, and 550 nM for the P301L aggregation prone tau mutant to phase separate. However, another study that performed single-molecule FRET and fluorescence correlation microscopy used low nanomolar concentrations of tau to identify clustering prior to visible droplet formation [77]. The study used PEG as a crowding agent and was able to determine a critical concentration of 5 nM, by comparing the diffusion time of the clusters with that of monomeric tau.

Spectral shift assays are capable of highlighting changes in the immediate microenvironment of the fluorophore and, as demonstrated in Chapter 3, can reveal details of phase separation processes. Tau was labeled as described in Section 2.2.5, using a polyhistidine tag at the N-terminal of the protein. The total labeled tau concentration was approximately 50 nM which was mixed in various ratios with unlabeled tau to produce final concentrations ranging from 10 - 0.25 µM. A thermal ramp at 1° C/ min was performed on each concentration from 10-55 °C. The curves were analyzed using the PCA algorithm,

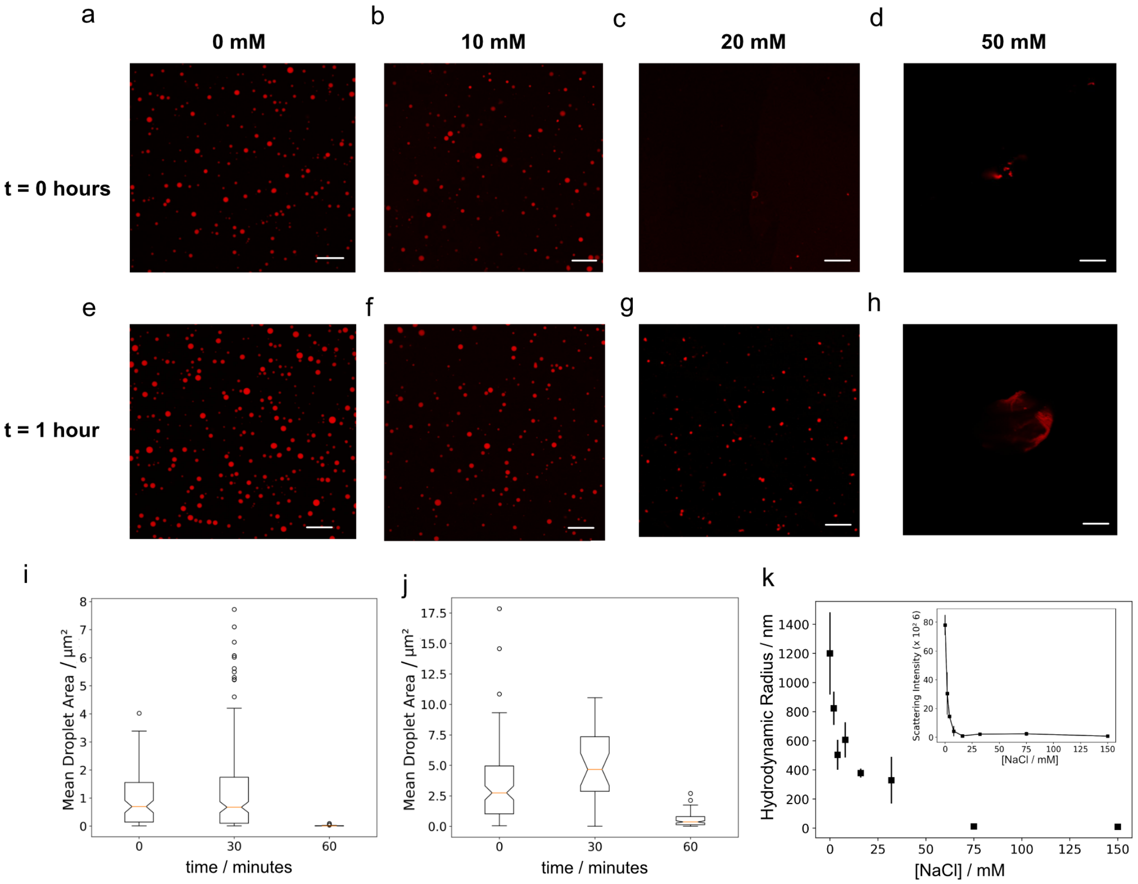

Figure 4.10: The effect of electrostatic screening on 10 µM complexed with 33 µg/µl Poly dA by varying NaCl concentration between 0 - 50 mM in LLPS buffer. Confocal micrographs **a) - d)** show droplet formation at t=0 whilst **e)-h)** show droplets after 1 hour. The average area and distribution of droplets are calculated at **i)** t=0 and **j)** t=1 hour **k)** The trends in droplet sizes are confirmed with dynamic light scattering performed on the complex in each salt concentration. Scattering is shown as secondary plot to highlight large scatterers at lower salt concentrations. Scale bar = 10 µm.

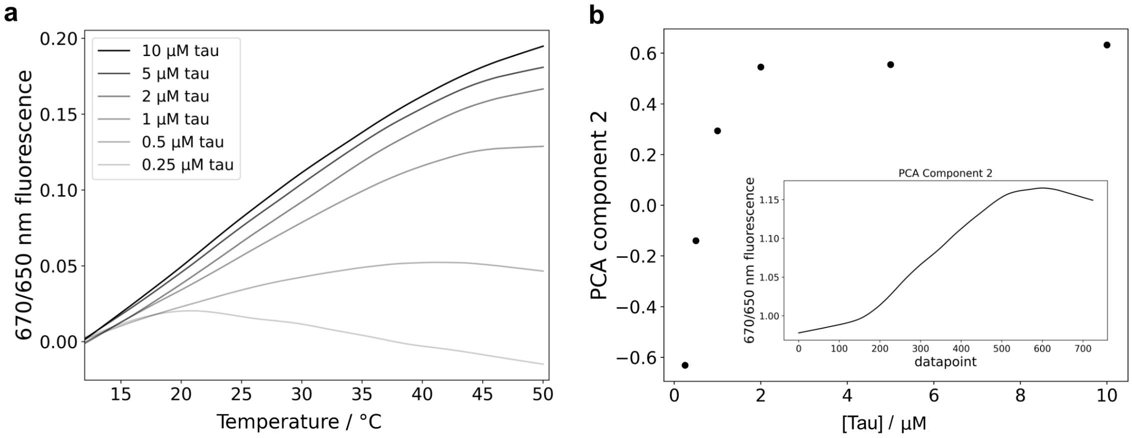

Figure 4.11: a) Simple coacervates of tau at varying concentrations in LLPS Buffer are monitored by the change in 670/650 nm fluorescence ratio over a thermal ramp from 1-55 °C , at a rate of 1 ° C/ min. **b)** The principal components describing main variances in curve are calculated, with PCA 2 describing the transition point most accurately. A critical concentration is determined by the points below which PCA 2 has a negative magnitude.

in which the second component described the phase transition most. The components were plot as a function of temperature, as shown in Fig. 4.11 **b)**. The curvature of the traces changes markedly below 500 nM, and this is reflected in the negative component of PCA2 below this concentration. A critical concentration of 500 nM in crowded conditions is comparable to studies performed by Kanaan *et al.* and is much higher than that reported by single-molecule FRET and fluorescence correlation spectroscopy by Wen *et al.*

4.5 Pathogenic implications of tau LLPS

The connection between aberrant protein aggregation leading to the formation of pathological β sheet conformations of tau and LLPS has been addressed in several ways in the literature. Wegmann *et al.* demonstrated that through the use of aggregation-competent, heparin-induced seeds, LLPS conditions could sustain fibrillization [187]. Condensates induced by both crowding and polyanionic cofactors were reported to also act as seeds for aggregation. Bokyo *et al.* investigated the impact of several tau mutants that are more prone to aggregation, such as P301L, to see effects on LLPS transitions [76]. It was found that, while the rate of droplet formation could not be altered, it in fact accelerated the formation of fibrillar aggregates, once again in the presence of an inducer. The overlap of phosphorylated tau and aggregation has also been widely studied, indicating that phosphorylation, although not a prerequisite for LLPS, usually requires the presence of crowding agents to successfully form droplets [187, 195]. Therefore, with the already high overlap in disease-causing mutations in LLPS-prone proteins [17, 196], it is interesting to consider the potential for therapeutic approaches that not only target fibrillar aggregates but inhibit condensate formation. For droplets mediated by hydrophobic interactions, the amphiphilic alcohol 1,6 hexanediol has previously been reported to dissolve condensates of both the FUS protein [196] and more recently tau [184, 187]. Droplets formed using crowding agents are typically also more robust and will not dissolve upon changing the ionic strengths of the buffers or by adding agents that simply disrupt hydrophobic interactions [79]. This makes the system interesting when determining factors that may inhibit droplet formation.

Substantial work has yet to be done to evaluate viable tau LLPS inhibitors and large-scale screenings have not been performed. Instead, reports have begun to characterize the effects of known aggregation inhibitors on LLPS. The premise that fibrillization inhibitors may instead prevent LLPS mechanisms has had interesting results. For instance, Pradhan *et al.* showed that a synthetic derivative of curcumin, which can inhibit the formation of neurotoxic oligomeric species, can also inhibit tau LLPS. The approach was validated both *in vitro* and *in vivo*, confocal microscopy being used to demonstrate a decrease in the size and number of droplets with increasing concentration of C1. However, in another study, another known aggregation inhibitor, epigallocatechin-3-gallate (EGCG), a green tea-derived polyphenolic compound, showed a different impact on LLPS and droplet formation [197]. EGCG has previously been reported to disassemble mature fibrillar inclusions [139] and suppress the rate of oligomerization of tau [198], with several interaction sites located in the proline-rich and microtubule domains of tau. The experiments performed by Chen and co-workers suggest that EGCG, however, promotes LLPS

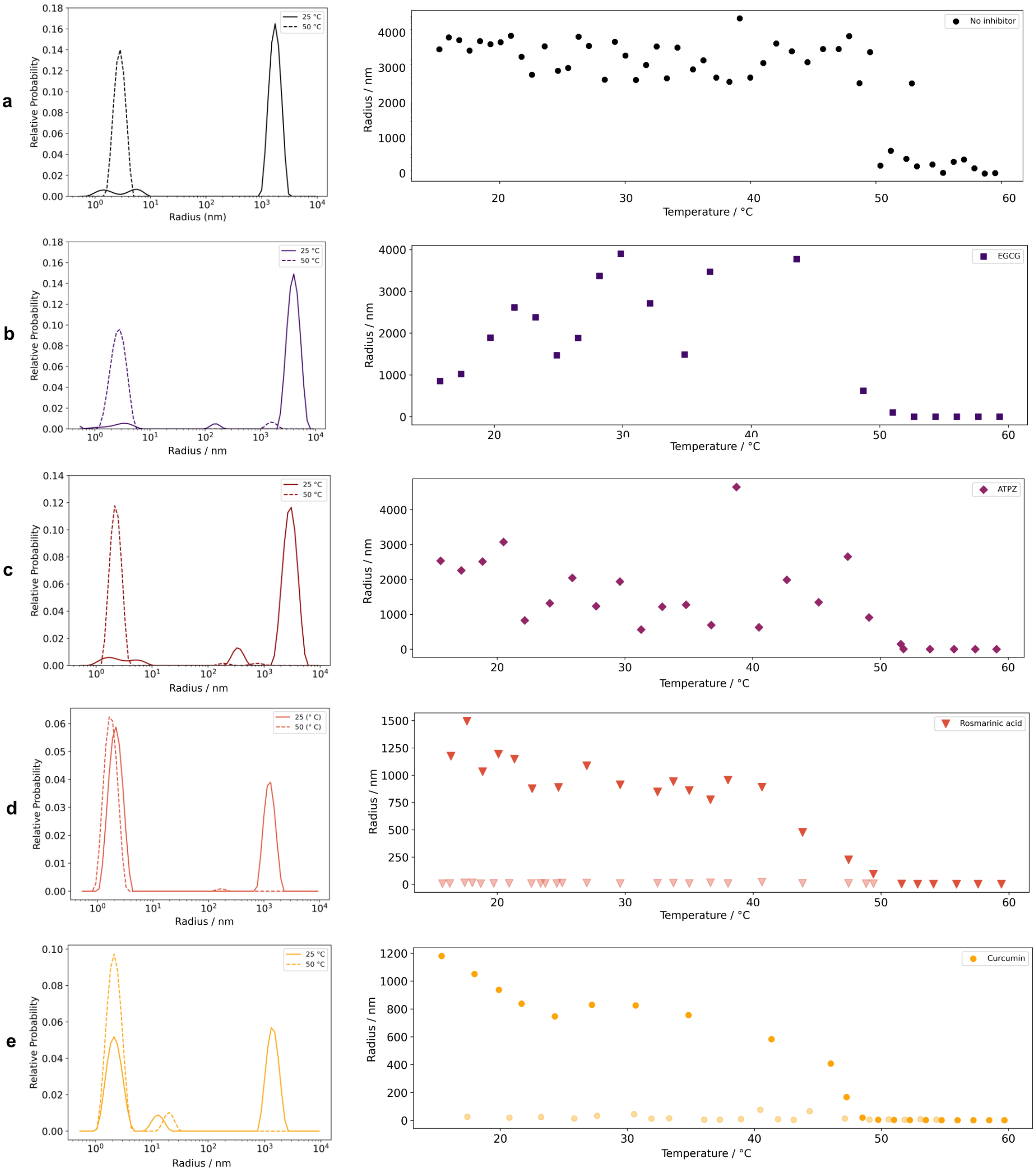

Figure 4.12: a) Inhibitor screening of LLPS using dynamic light scattering over a temperature ramp of 1 °C/min. A crowded LLPS system of 20 μM tau in the presence of 10 % PEG was used to screen four compounds. Dynamic light scattering of a) Uninhibited tau-PEG system, **b)** ATPZ aggregation inhibitor, **c)** EGCG **d)** Rosmarinic acid, and **e)** Curcumin extract measurements allow the size distribution to be determined over a temperature ramp. The left panel shows the distribution before and after the transition point whilst the right panel shows size population over a ramp.

of tau through a combination of hydrogen bond formation and hydrophobic interactions of EGCG with the proline-rich region. Turbidity measurements and microscopy analyses showed a concentration dependence of EGCG on droplet promotion, which was proposed to be due to the availability of binding sites on tau.

To evaluate the effect of other inhibitors on tau LLPS, both compounds which were previously evaluated in the literature, as well as two other aggregation inhibitors, rosmarinic

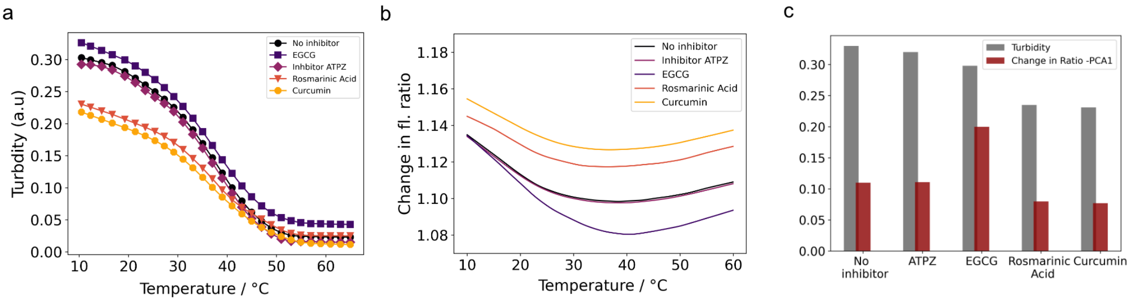

Figure 4.13: a) shows the absorbance measurements at 400 nm, for each inhibitor system tested over a thermal ramp of 2 °C/ min. **b)** spectral shift ratios are used to demonstrate the effect of the compounds over a thermal ramp. **c)** The change in absorbance at 15 °C is shown for each condition tested. A comparison is made from the PCA analysis evaluating the change in curvature of each trace compared to the uninhibited LLPS system.

acid and an aminothienopyridazine inhibitor (ATPZ-16), were tested using three methods. Since polyphenolic compounds such as EGCG and curcumin have a low fluorescence in the 350 nm range, the extrinsic fluorescence ratio method was used instead of intrinsic fluorescence to monitor the 650 nm / 670 nm fluorescence ratio of labeled tau over a thermal ramp, to allow all compounds to be screened on the same platform. The tau - PEG system was analyzed by dynamic light scattering to observe the size of droplets over a temperature ramp, and to monitor the distribution of different size populations in the presence of each compound, using microliter volume capillaries. Lastly, absorbance measurements taken at 400 nm are used to monitor any changes in turbidity, by using a temperature-controlled cuvette-based spectrophotometer as described in Section 2.5.1. The concentrations of inhibitor compounds chosen were in the range of at least twice the known binding affinities to tau, with 50 µM ATPZ, 200 µM EGCG, 50 µM rosmarinic acid and 50 µM curcumin extract. Sample volume and tau concentration were kept constant for each sample, and controls with each inhibitor in the presence of PEG were formed in parallel for each measurement method used. For spectral shift measurements, all traces are evaluated using the PCA algorithm to compare the change in curvature of each trace to the uninhibited system. The values plotted in Figure 4.13 **b)**, are the first principal component that determines the change in ratio over the ramp.

The effect of each compound on the size of the droplets monitored using dynamic light scattering is shown in Fig. 4.12 **a)** to **e)**. The control uninhibited system shows a single population of large droplets with radii in the range of 1-2 µm. The temperature dependence of the UCST system is shown with the droplets dissolving at 47°C. The first inhibitor, ATPZ, also showed this transition without a noticeable effect on droplet size Fig. 4.12 **b)**. The turbidity measurements confirm this observation, with the maximum absorbance varying only by 0.01 A.U. However, the effect of EGCG is evident in the particle size being greater in the range of 3-8 µm, suggesting that larger droplets are indeed promoted in the presence of this compound and in the small increase in absorbance (Fig. 4.12 **e)** and Fig. 4.13 **b)**). Interestingly, both the curcumin and rosmarinic acid polyphenols demonstrated an inhibitory effect on tau LLPS. While Pradhan *et al.* [199] demonstrated the decrease in droplet size in their work, this effect is seen in the presence of two main size populations when tau-PEG is treated with curcumin. The same effect is also observed with rosmarinic acid in Fig. 4.13 **a)**. The darker points in Fig. 4.12 **d)** and **e)** represent the population with the highest relative probability in the size distribution, whilst the lighter points represent the second population, with a noticeably smaller size. This size distribution for each sample indicates not only the presence of smaller droplets but also a decreased propensity for droplet formation. The decrease in absorbance values and smaller spectral shift ratio are also highlighted for each of these compounds in Fig. 4.13 **a)** - **b)**. This is the first reported instance of rosmarinic acid showing suppression of tau LLPS. The mechanism by which rosmarinic acid binds to tau has been suggested to be via the carboxylate group of polyphenol and the lysine in the VQIVYK motif in the microtubule-binding region [141]. This interaction may decrease the propensity for tau-tau interactions by reducing the number of nucleation points in the MTBR. However, as is the case for Curcuma, the exact mechanisms behind LLPS inhibition by polyphenols may be multifold. As such, any mechanism which is successful in suppressing droplet formation may range from increasing the solvation entropy of tau to decreasing the tau-tau self-interactions, or another valency-modifying mechanism.

4.6 Conclusion

The process of evaluating the efficacy of any inhibitory compound must first begin by means of a screening process. High-throughput methods presented here, with multi-parametric measurements using intrinsic and extrinsic fluorescence ratios coupled with DLS, can in combination provide a powerful approach for assessing the LLPS behavior of both novel and model systems. As is the case for tau, an intrinsically disordered protein, the use of IFR to measure tyrosine fluorescence offers a unique opportunity to report on this process at the amino acid conformational level. However, this process is not trivial and requires techniques that can reliably identify the changes in these fluorescence traces. PCA demonstrates a way of evaluating a dataset independently of setting a threshold for onset temperatures and successfully identifies small changes in the fluorescence traces. The power of the method was further proven using a tau-PEG system as a model system, relative changes in the curves seen in the presence of each inhibitor can be identified. Labeling tau with a near IR extrinsic fluorophore enhances this approach by offering to increase the number of compounds to be tested regardless of their intrinsic fluorescence in the UV-VIS range, as well as offering the capability of working at nanomolar concentrations. Thus, this robust method of LLPS analysis holds the potential for extension into a large screen which can be used as a stepping stone to the discovery of more candidates in a dual therapeutic approach for tauopathies.

Chapter 5

Routes to Aptamer Based Assays to Monitor Early Stages of Tau Fibrillization

5.1 Affinity-based detection techniques for tau

Affinity-based molecular recognition typically uses the specificity of an antibody or aptamer for the detection, identification, or even quantification of a certain tau construct. Antibodies have been widely used in immunoassays to identify oligomeric species of tau and have also been a major therapeutic approach targeting monomeric and oligomeric tau. However, the specificity and stability of various tau antibodies have raised concerns about their use in quantitative studies [200]. In an extensive study by Ellis *et al.*, the specificity of certain isoforms and oligomeric state-specific antibodies was shown not only to have a high degree of cross-reactivity with off-target tau constructs but also to show that several antibodies are incapable of detecting low levels of tau in Western blot and immunohistochemistry experiments.

Another tool for molecular recognition that has become a popular alternative to antibodies is a class of functional nucleic acids, termed aptamers. These 15-200 nucleobase sequences were first identified in 1990 and demonstrated the ability to form tertiary structures capable of binding to a specific target [201, 202]. Although natural aptamers are observed, synthetic aptamers are commonly isolated in a process that allows the enrichment of target binding sequences in a combinatorial process called SELEX (Systematic Evolution of Ligands by Exponential Enrichment) [201]. In this process, a large pool of random oligonucleotides are exposed to the target in a selection round, after which an amplification round enriches the population of bound sequences. Several iterations of this process allow the isolation of a small number of potential aptamers, which are only confirmed after performing interaction analyses with the target [203].

Aptamers have now emerged as reliable bioreceptors for a variety of molecules, including proteins, lipids, viruses, and even small molecules such as ions [204]. The affinities of these DNA- or RNA-based sequences are normally in the range of nanomolar to picomolar, analogous to antibodies. As such, the use of aptamers for their specific binding, low batch-to-batch variation, and stability has made them an advantageous alternative to target specific pathological versions of tau [205].

Until now, the use of aptamers in neurodegenerative disease research has been focused on their use as a detection agent in biosensing platforms to quantify tau levels, or as a therapeutic app/roach where the binding of aptamers to various tau constructs is intended to have an inhibitory effect on the fibrillization pathway [203, 206, 207]. Table 5.1 lists the known aptamers and the tau construct to which they target, as well as the type and length of the oligonucleotide sequence. Thus far, two aptamers have been successfully reported to inhibit the fibrillization of tau. The aptamer reported by Kim *et al.* [207], is an RNA aptamer called tau-1, capable of binding tau dimers and trimers, while demonstrating reduced neurotoxicity in cell models. Meanwhile, the aptamer developed by Teng *et al.* [208], instead targeted the phosphorylatable epitopes of tau, primarily in the proline-rich region. The aptamers reported here, unlike tau-1, not only reduced the levels of oligomers but also completely prevented the oligomerization process. Both aptamers were discovered using the SELEX approach, but two tau aptamers have been identified using variations of a capillary electrophoresis-based selection method, which does not require repetitive rounds of PCR amplification. The aptamers reported by these two groups targeted different tau isoforms, with affinity constants ranging from 14 nM for full-length tau as reported by Lisi *et al.* [209] to 350 nM for tau-410 as reported by Krylova *et al.* [210]. Thus, these aptamers have been used primarily in diagnostic approaches, for example, as recognition elements for electrochemical and optical-based biosensing platforms[206, 207, 211, 212], and thus appear ideal for the development of a real-time kinetics assay.

Table 5.1: Aptamers that bind to tau described in the literature.

Construct	**Nucleic Acid**	**Ref.**	**Specificity**
His-tagged Tau40	RNA - 40nt	[207]	Targets tau dimer and trimers. Inhibitory
Tau 381 and 410	ssDNA - 15nt	[210]	Target tau monomers. Not inhibitory
Tau 441	DNA 6-68 nt	[208]	Targets phosphorylatable epitopes. Inhibitory
Tau 441	DNA (length undisclosed)	[209]	Targets monomeric tau

5.2 Using aptamers to monitor the concentration of tau monomers

This chapter explores the use of aptamers specific to monomeric tau to create an affinity-based real-time detection assay. The hypothesis used to develop the assays described in this work is that monitoring the change in monomer concentration over time can be used to estimate the kinetics of the early stages of fibrillization, before the beginning of mature fibril formation reported in thioflavin T assays (Fig. 5.1). As such, the chosen aptamer should specifically bind to tau monomers and should also be noninhibitory during the fibrillization process. Therefore, the aptamer reported by Krylova et al. [210] was selected, as this satisfied the requirements. The aptamer reported in reference [209], bound to monomeric tau with low nanomolar affinity, however, the sequence was not made accessible for public use. The affinity of the aptamer was determined by measuring the

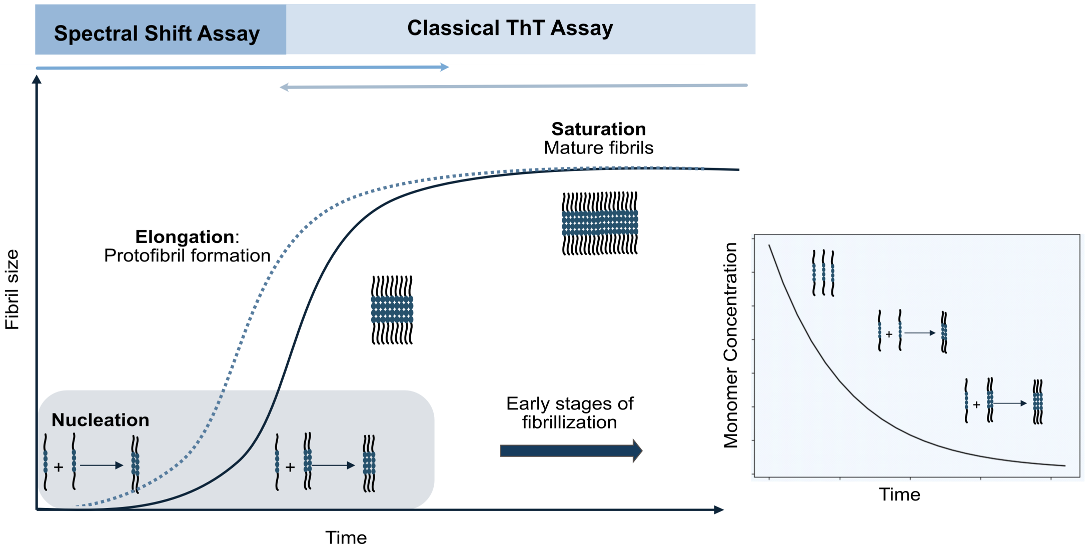

Figure 5.1: Schematic which demonstrates the development of a real-time affinity-based detection assay which monitors the concentration of monomeric tau (dotted line), in comparison with classical ThT assay.

fluorescence of a fluorescein-labeled nucleic acid sequence during non-equilibrium capillary electrophoresis.

5.2.1 Choosing the correct labeling approach

To design a system in which the concentration of monomeric tau could be monitored in real-time using a fluorescence-based signal, it is critical to assess labeling approaches. Previously, the aptamer was identified in a process in which the nucleic acid was labeled, and the dye did not inhibit specific interaction with the target protein. However, the position of the label on the aptamer may be crucial for the formation of the correct three-dimensional structure necessary for target-specific binding. This was not previously investigated, and as such, several labeling sites were chosen. The NUPAC server was used to predict which regions of the aptamer could form secondary structures [213]. The structure of each aptamer is shown in Fig. 5.2 and shows that the aptamer undergoes a fold near the five prime end. The first approach was to label the aptamer at the five prime end (Aptamer A) and then the 3′ end (Aptamer B). In addition, to ensure that the proximity of the fluorophore to the folded regions of the nucleic acid structure did not affect the binding to the target, we also added a polyT spacer to each of the labeled sequences (Aptamers C and D). The interaction of labeled aptamer and unlabeled tau was measured using an automated plate-based spectral shift experiment as described in Section 2.3.3. The spectral shift binding isotherms over a course of ten hours are shown in Fig. 5.3 **a) -d)**.

From these data, it is visually evident from the change in K_d over time that the labeled aptamer has a slow association to tau, with the dissociation constant changing from 5 μM to 300 nM. To quantify the rate of association of the aptamer to tau, the observed rate constants (k_obs) for this process must first be determined by evaluating the change in the

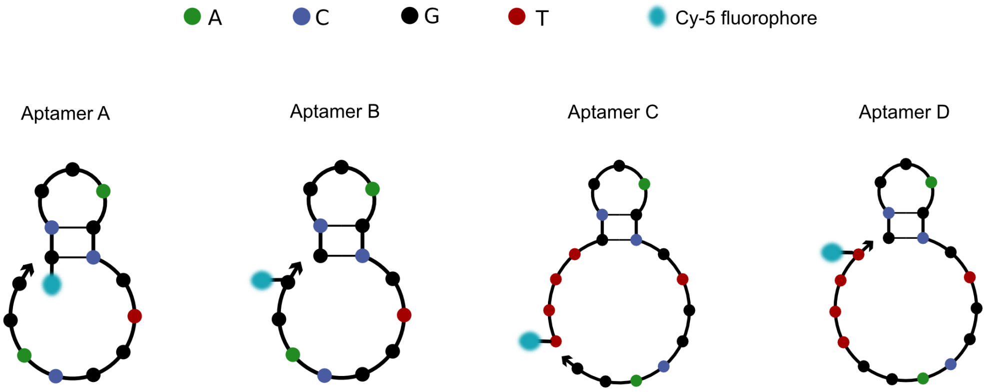

Figure 5.2: Predicted secondary structure of differently labeled aptamers. Aptamers A and B are labeled at 5′ and 3′ ends without spacers, whilst Aptamers C and D are labeled with poly T spacers. Arrow indicates 3 prime ends.

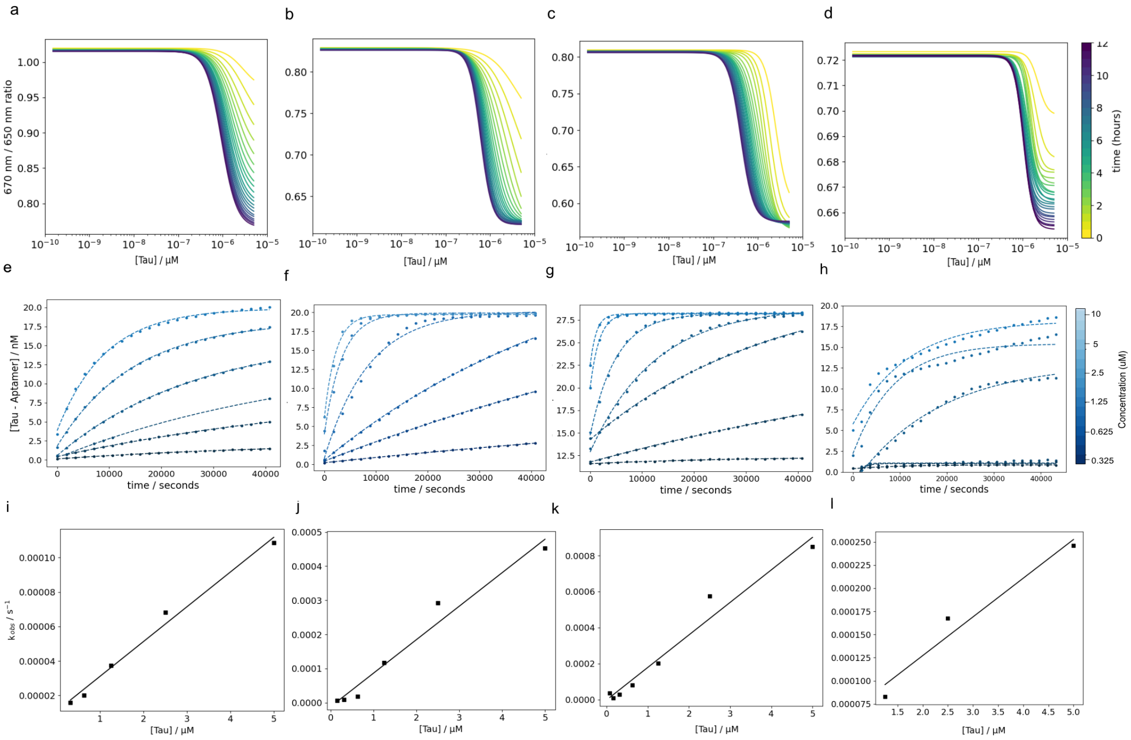

Figure 5.3: a) - d) shows fitted binding isotherms for Aptamers A, B, C, and D respectively, over 12 hours, using 20 nM aptamer and a dilutions series of unlabelled tau, evaluated using spectral shift. Assays are performed at 25 °C, in HEPES buffer (10 mM Hepes, 150 mM NaCl, 2 mM DTT, pH 7.5) **e) - h)** show the change in the ratio over time for different tau concentrations, for each aptamer fitted to a single exponential equation 5.1. **j) - l)** The k_{obs} values for each tau concentration are plotted and fitted to a straight line to determine the on-rate for each system.

concentration of the aptamer-tau complex for varying values of tau over time. A pseudo-first-order approach to measure the on-rate requires that the concentration of free tau in solution should not effectively change as the aptamer-tau complex forms. Since this assay uses tau concentrations that are significantly higher (> 10X) than the concentration of the labeled aptamer, this approach is valid.

The concentration of bound tau can be calculated by determining and assigning the value of 100 % bound to the ratio value at saturation and 0% to the ratio value for the lowest concentration of tau. A linear relationship between the ratio and the fraction bound can be used to determine the value of the tau-aptamer complex for each concentration of tau. The progress curves are fitted to a single exponential equation 5.1 to derive observed rate constants, k_{obs}, as well as the half-time of the reaction $t_{1/2}$ by the relation in equation 5.2.

$$y = A(1 - \exp(-k_{\text{obs}} \cdot t) + y_0) \tag{5.1}$$

$$t_{1/2} = \frac{ln2}{k_{\text{obs}}} \tag{5.2}$$

where y is the amount of bound tau at time t, y_0 is the initial signal of the tau bound, and A is the preexponential factor, equivalent to the maximum amount of aptamer-tau complex.

Concentrations that showed a sufficient change in the amplitude of the exponential function were evaluated, maintaining that the concentration of aptamer was >10X concentration of the tau, as shown in Fig. 5.3 **e)**- **h)**. Values for k_{on} were then determined by plotting the observed rate constant k_{obs} against the concentration of tau and fitting the data points to a straight line since k_{obs} = k_{on} [tau] + k_{off}. The on-rate was thus determined by evaluating the slope of this line as indicated in Fig. 5.3 **i)**- **l) and reported in Table 5.2**

Table 5.2: List of differently labeled aptamers

Oligonucleotide	**Sequence (5′ to 3′)**	k_{on} ($M^{-1}s^{-1}$)
Aptamer A	Cy5 - GCGGAGCGTGGCAGG	20.16
Aptamer B	GCGGAGCGTGGCAGG - Cy5	98.15
Aptamer C	Cy5 - TTTTGCGGAGCGTGGCAGG	160.85
Aptamer D	GCGGAGCGTGGCAGGTTTT - Cy5	41.45

The addition of polyT spacers to the aptamers improved the initial binding to the protein, as shown by the higher association rates, compared to aptamers without the spacers. Interestingly, the five-prime modified aptamer with the spacer (Aptamer C) showed the fastest on-rate and was not affected by the proximity of the dye to the secondary loop shown near the five-prime end. However, the presence of the cationic fluorophore ultimately affected the interaction between the protein and the aptamer. Because the use of the labeled aptamer to monitor in situ kinetic measurements could prove unreliable if the change in the dose-response signal over time is due to the slow binding of the aptamer and not to fibrillization of the tau, an alternative approach utilizing labeled tau was pursued.

5.3 Optimization of aptamer-based kinetics assay

Because the presence of a label on the aptamer was not ideal for a real-time detection system, the second approach was to label the tau protein and mix it with a titration of an unlabeled aptamer, and again monitor the binding signal as a function of time. There are several important parameters to consider before performing fibrillation studies on labeled protein samples. The first is to ensure that the monomeric protein is stable before and after labeling, since labeling can result in unwanted aggregation of the protein. Second, the label should not interfere with the fibrillization process, and in the case of the affinity-based detection assay, it should not prevent interaction with the aptamer. Finally, it is imperative that the protein fibrillizes in a reproducible way, in order to reliably compare conditions that affect fibrillization.

5.3.1 Optimisation of labeling of Tau

The study of tau fibrillization commonly uses fragments of the full-length tau isoform, consisting of varying sections of the microtubule-binding region, as it is the most aggregation prone region in the protein. Since truncated versions of tau have been found in the brains of Alzheimer patients, likely due to the sensitivity of tau to catalytic digestion, the aggregation behavior of fragments containing the MTBR has also been studied [214]. Two of the most used sequences are the K18 and dGAE peptides, as shown in Fig. 5.4 **a)**. K18 has been commonly used in cellular studies, specifically due to its reliable seeding behavior, however, the dGAE fragment has gained significant interest due to the discovery that it is capable of self-assembling into fibrils that closely resemble the structure of those derived from patient samples, without the need for cofactors. [215, 216].

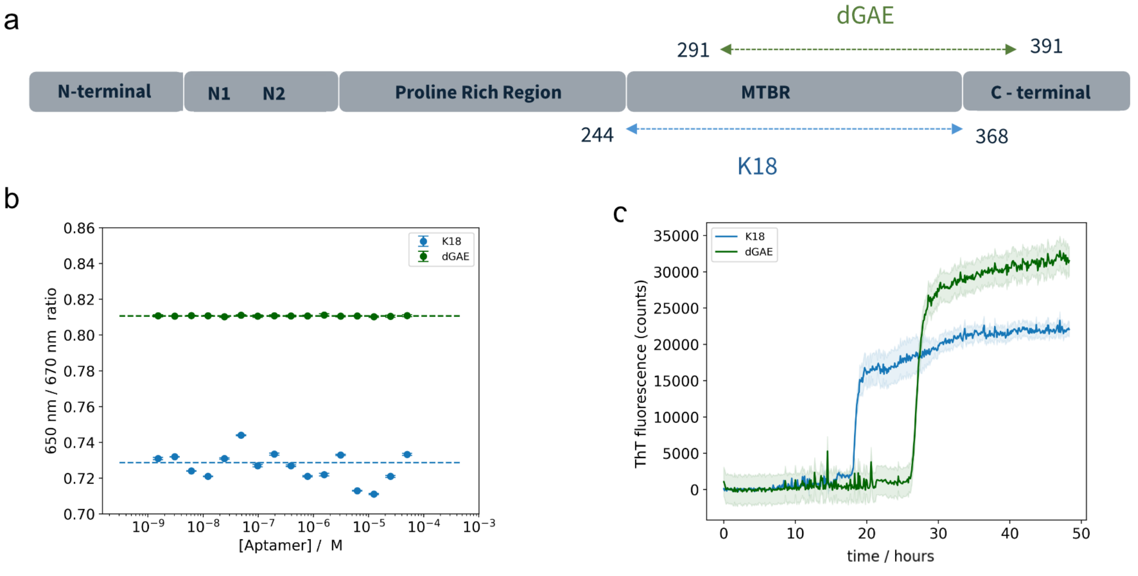

Figure 5.4: a) the amino acid sequence of Tau 441, with fragments K18 (blue) and dGAE (green) highlighted. **b)** The interaction of each fragment with labeled aptamer using Spectral Shift analysis. The line is fitted with a non-binder model using Monolith Control Software. **c)** Thioflavin T assays performed on 100 µM dGAE, without an inducer, 100 µM K18 in the presence of 10 µM heparin. Assays were performed in 10 mM phosphate buffer (pH 8.2).

Therefore, the interaction of the labelled aptamer with these fragments was evaluated using spectral shift. However, as shown in Fig. 5.4 **b)-c)**, whilst the fragments reliably show fibrillization in thioflavin T assays, the aptamer failed to bind to these truncated fragments. Because these fragments primarily consist of the MTBR region of tau, it can be inferred that the N- and C-termini may be important for the binding of aptamers. Since the MTBR is also imperative for the oligomerization process, the seeming lack of dependence on MTBR for aptamer binding could explain why the aptamer is not inhibitory. Thus, the tau construct chosen for this fibrillization assay had to be full-length tau.

For the full-length tau, two labeling approaches were explored: Non-covalent Histag labeling, and covalent NHS-ester labeling. Since the Tris-NTA dye showed specific binding to his-tagged tau-441 (Fig. 5.5 **a)**. However, when Histag-labeled tau was titrated against a series of aptamer dilutions, no interaction was observed between labeled tau and aptamer, as shown in Fig. 5.5 **b)**. Because the polyhistidine tag is located at the N-terminal of the protein, this supports the hypothesis that the N-terminal is necessary to support the binding of the aptamer to the protein.

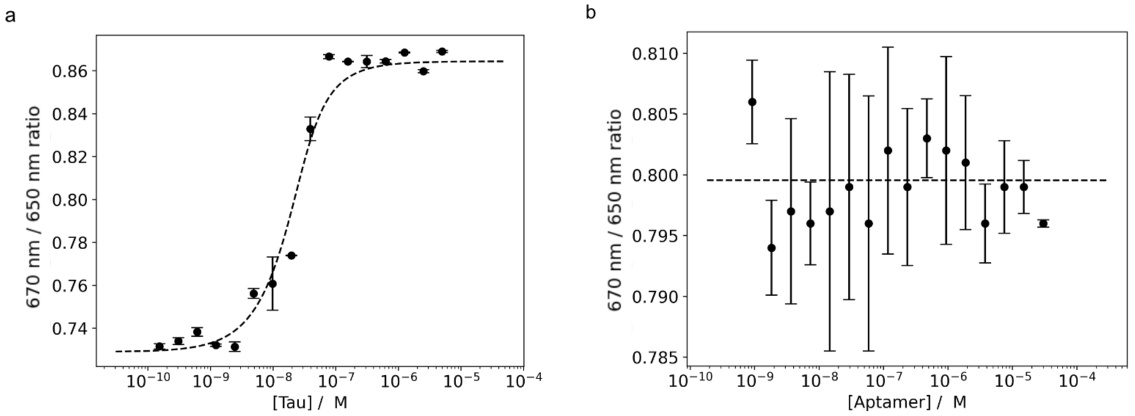

Figure 5.5: a) The strength of interaction of RED-tris-NTA 2nd Generation dye with Histagged tau-441 using Spectral Shift analysis. Assays were performed in HEPES Buffer (20 mM HEPES, 150 mM NaCl, 2 mM DTT, pH 7.5). The line is theoretical and described by the single site binding model with a calculated K_d of 8.2 nM. **b)** Dose response curve for 20 nM of Tris-NTA labeled tau with unlabelled aptamer shows no binding. The line is fitted with a non-binder model using Monolith Control Software

Therefore, NHS-ester-based labeling was chosen in which primary amines, predominantly lysines, are labeled as described in Section 2.2.5. For this purpose, a tag-free tau-441 was used to eliminate any potential interaction of the polyhistidine tag with the aptamer. Since the quality and monomeric nature of the protein needs to be verified post-labeling and the NHS-ester-based labeling strategy requires the removal of excess quenched dye, size exclusion chromatography was performed, monitoring both the absorbance of protein at 280 nm and dye at 650 nm. As shown in Fig. 5.6 **a)**, the labeled protein appeared to be monomeric post-labeling. The peak eluted at the 12 ml position was collected. Note that tau is an intrinsically disordered protein and has been documented to migrate in size exclusion chromatography columns at higher apparent molecular weights [40, 217]. The tau-441 concentration (1.3 μM) and the degree of labeling

(0.7) were determined using the absorbance values at 280 and 650 nm using the method described in Section 2.2.5.

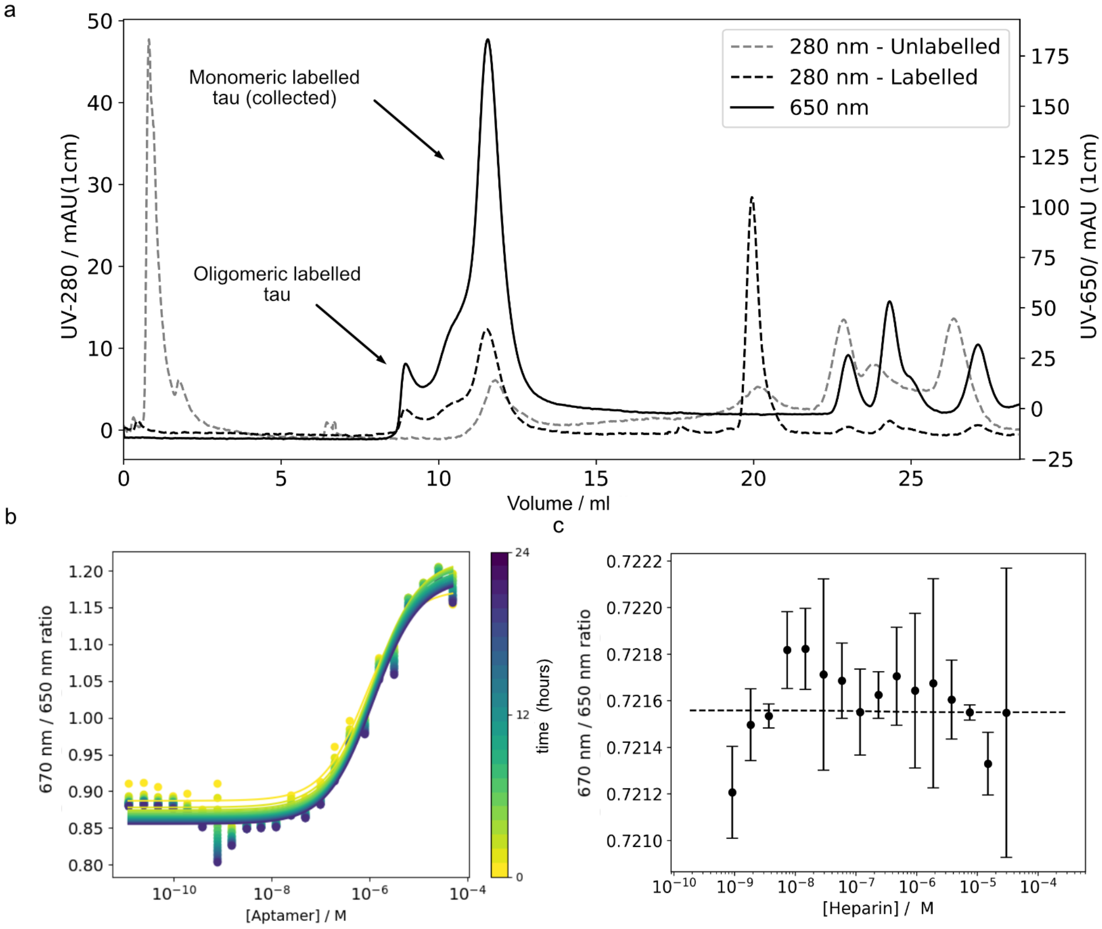

Figure 5.6: a) The size exclusion chromatogram shows the monomeric labeled tau being eluted at 12 ml peak, by monitoring the 280 nm and 650 nm absorbance of the protein and dye respectively. Protein was eluted into HEPES Buffer (20 mM HEPES, 150 mM NaCl, 2 mM DTT, pH 7.5). Both labeled and unlabelled protein were purified via this method. **b)** Binding isotherm over 24 hours for labeled tau and unlabelled aptamer shows immediate binding of tau to aptamer with affinity 500 nM. **c)** 20 nM labeled aptamer is titrated against heparin to confirm no interaction prior to use in fibrillization assay.

The labeled tau-411 was then titrated with the unlabeled aptamer to determine the binding affinity via spectral shift, as shown in Fig. 5.6 **b)**. Interestingly, the aptamer without the fluorescent label bound immediately with an affinity of 500 nM to the labeled protein and showed no change in dissociation constant over time. Thus, it is proposed that the cyanine 5 dye when attached to the aptamer allosterically or electrostatically hinders the necessary conformational change required for a specific interaction with the protein. Therefore, experiments using the unlabeled aptamer were used to study the kinetics of tau fibrillization. For reliability, fibrillization assays were performed in the presence of a known inducer, heparin [59]. Control experiments confirmed that heparin does not specifically interact with the labeled aptamer (Aptamer C) (Fig. 5.6 **c)**), allowing the change in monomeric tau concentrations over time to be monitored using the affinity-based aptamer assay.

The concept of this assay is to monitor the change in amplitude of tau-aptamer populations over time, providing a signal for decreasing monomeric tau concentration (Fig. 5.7). This change in signal describes the first oligomerization steps in fibrillization assay by monitoring the change in amplitude of the dose-response curve as an indication of a decreasing monomeric tau population. A key factor that determines the rate of oligomerization is the concentration of heparin used to induce fibrillization [114]. The effect of heparin in the oligomerization of tau has been widely debated in the literature, with respect to the mechanism of induction. Although polyanionic heparin is used as a crowding agent, its electrostatic interaction with tau has led to varying positions on whether it is incorporated into the fibril [71, 218], or not [109, 114, 219].

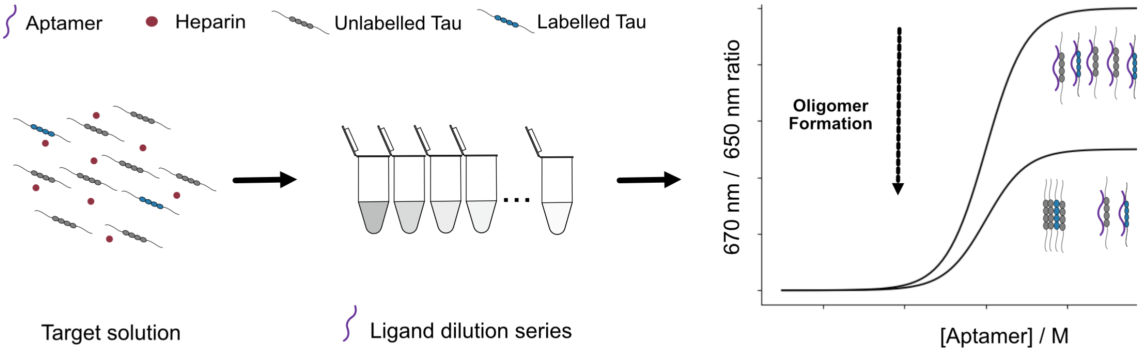

Figure 5.7: Experimental schematic describing the affinity based detection assay for monitoring tau fibrillization. 20 nM labeled and 2 μM unlabeled tau are mixed together. Heparin is used to induce fibrillization. The heparin : tau mixture is added to a dilution series of unlabelled aptamer, and the interaction is monitored using spectral shift, continuously over time.

Heparin molecules have also been suggested to interact with tau and have been shown to alter the conformation of tau fibrils, compared to those induced by seeding [72]. However, the mechanism behind heparin-induced fibrillation has been extensively studied due to the physiological relevance of similar polysaccharides that have been known to interact with tau [220]. As such, the effect of heparin concentration was studied using this aptamer-based assay, not only to validate the efficacy of the assay but also to observe changes in the impact of the inducer on the early stages of oligomerization.

Three different concentrations of heparin were used to induce fibrillization of tau, which was mixed with a series of dilutions of the unlabeled aptamer. To ensure fibrillization was induced, 20 nM labeled tau was used as the reporter within a total concentration of 2 μM tau. The samples were measured every hour for a period of one to two days at 37 ^{o}C until no further changes in the amplitude of the dose-response curve could be observed. Fig. 5.8 **a)** - **d)** shows the decrease in the amplitude of the signal in the dose-response curves of aptamer binding to tau, for three different conditions, 0.01, 0.02, and 0.04 mg/ml heparin. The molar ratio of heparin : tau for each condition was estimated to be 0.3:1, 0.6:1, and 1:1, respectively, since the molecular weight of heparin is between 12-15 kDa. To assess which concentrations of aptamer in this assay would reliably report the concentration of monomeric tau, the fluorescence ratio as a function of time was plotted and fitted to a single exponential equation (Equation 5.1), to model the reduction in monomer concentration. A global fit was performed using the method described in Section 2.4.2 and Appendix B.2 by fitting each data set with a shared parameter of k_{obs}

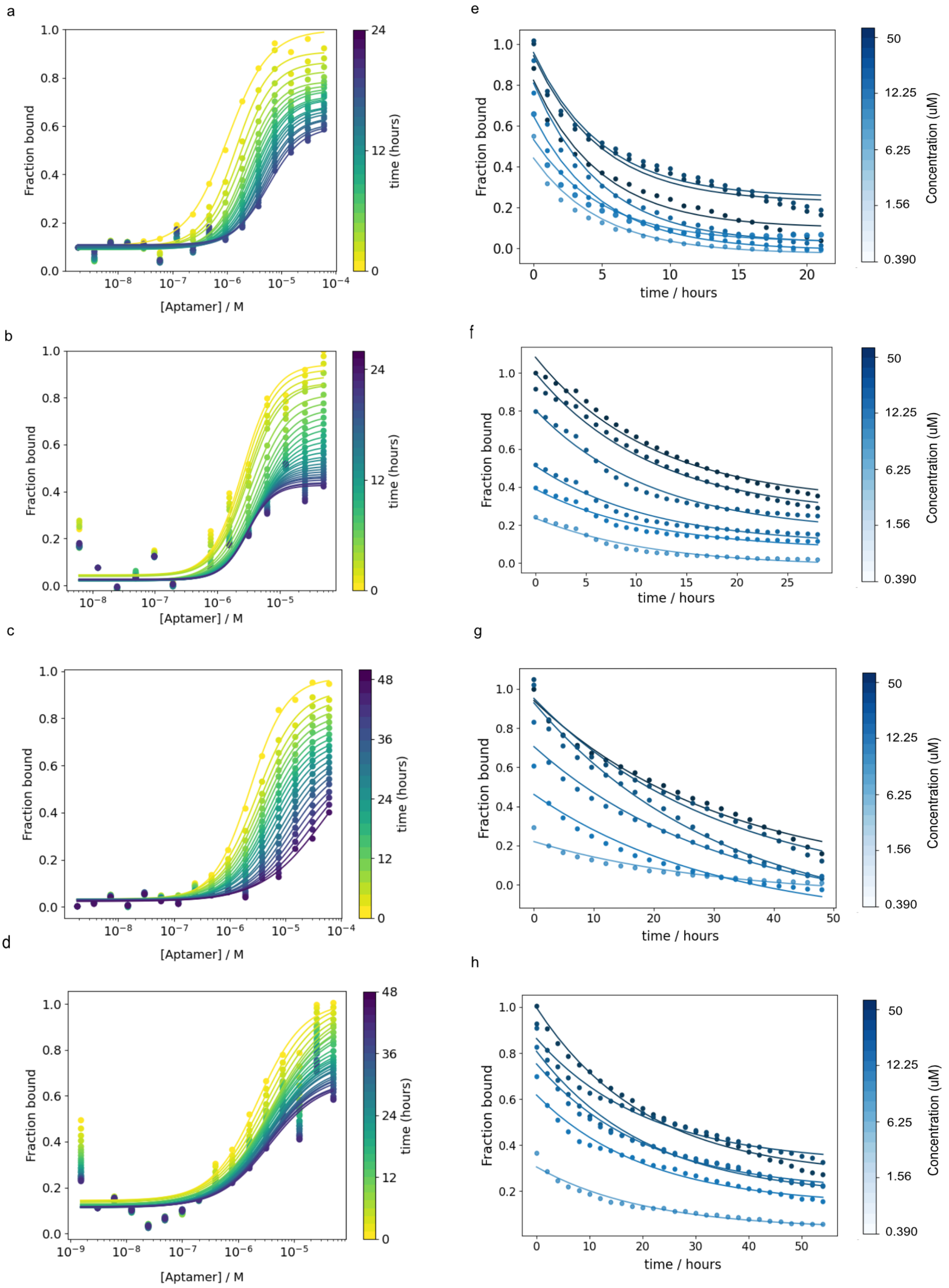

Figure 5.8: The dose-response curve for 20 nM labeled tau against unlabelled aptamer, in the presence of excess 2 µM unlabelled tau and heparin to induce fibrillization. The heparin : tau ratios are **a)** 1 **b)** 0.8 **c)** 0.6 and **d)** 0.3. **e) - h)** For each heparin concentration, the change in ratio for the first 8 concentrations of the aptamer is plotted over time and fitted to a global single exponential fit, from which a global kinetic parameter k_{obs} can be derived. The assay is monitored over 24 hours, at 37 °C in HEPES buffer (20 mM HEPES, 150 mM NaCl, 2 mM DTT, pH 7.5).

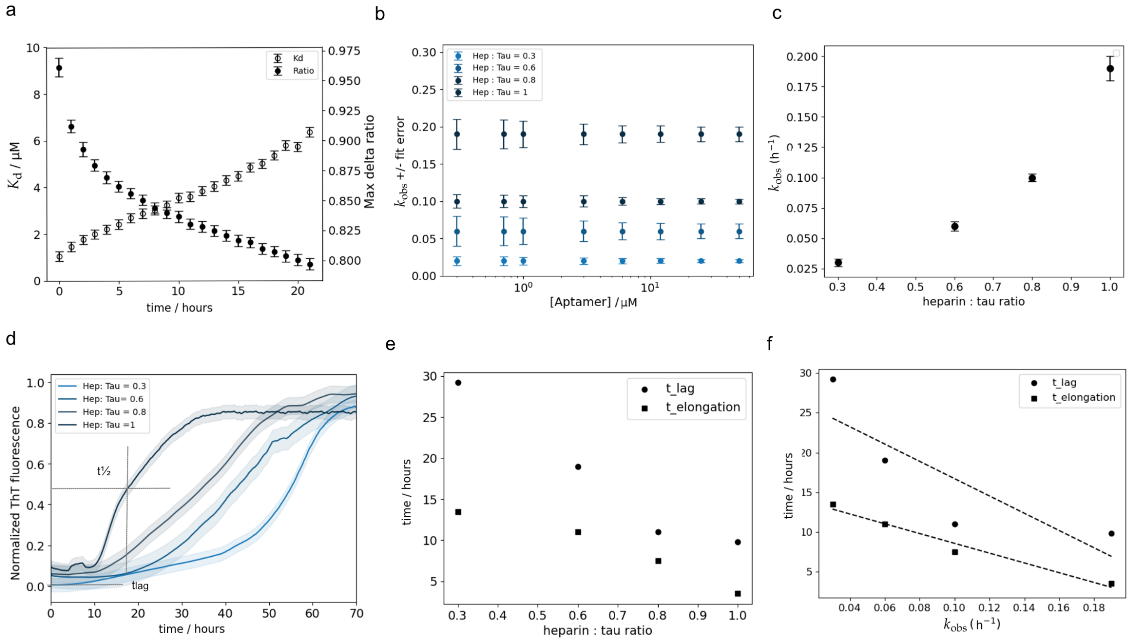

Figure 5.9: a) The change in ratio and K_d over time are shown for tau : heparin ratio 1:1. **b)** The concentration limit for which the aptamer can be used reliably as a detection agent in this assay was determined by sequentially comparing the error in the global fit for k_obs for each aptamer concentration. **c)** The effect on the heparin concentration used to induce fibrillization can be monitored as a function of k_obs **d)** Thioflavin T assays were performed for each of the heparin ratios 37 °C in HEPES buffer (10 mM HEPES, 150 mM NaCl, 2 mM DTT, pH 7.5) **e)** The relevant time constants for nucleation and elongation are plotted as a function of varying heparin : tau ratios. **f)** Shows a linear regression between each ThT time constant and k_obs.

and the global fit error parameter was evaluated as each concentration was sequentially added (Fig. 5.8 **e) - h)**). As the amplitude of exponential decay decreases with lower concentrations of aptamer, the signal-to-noise in the ratio value decreases, resulting in a progressively larger error in the fit as shown in Fig. 5.9 **b)**. The number of curves chosen to be evaluated for each system was thus based on when the fit error increased to 30% its original value, resulting in the evaluation of 6-7 curves to obtain the global fit. The values for k_obs were found to be 0.02, 0.06, 0.1 and 0.19 h^{-1} with increasing heparin : tau ratios, as shown in Fig. 5.9 **c)**. The effect of heparin on the fibrillization rate has been reported so far to depend on the ratio of heparin to tau, and some studies indicate that there is a dose-dependent mechanism [112, 114]. Carlson *et al.* reported that below a 1:1 heparin : tau ratio, increasing heparin concentrations promotes fibrillization, and above a ratio of 4:1, there is instead an inhibitory effect [114]. Therefore, the trends reported by this aptamer assay agree with the positive effect of fibrillization heparin in specific heparin : tau ratios.

The observed rate constants for the reduction of monomers show a clear positive trend with increasing heparin concentration; i.e. monomer tau concentration decreases faster at higher concentrations of heparin. However, to contextualize this process on timescales for nucleation and elongation, thioflavin T assays (see Section 2.3.1) were performed under conditions identical to those of the aptamer spectral shift assay, that is, samples were incubated at 37 °C, in a microwell plate, without shaking (Fig. 5.9 **d)**). To quantify the nucleation and elongation phases, two values; the lag time t_lag and the elongation time constant T were calculated, where $t_{lag} = t_{1/2} - 2T$ [96]. Each of the time constants is plotted in Fig. 5.9 **e)**. The trend in time constants was then compared with those obtained by the aptamer assay with the nucleation time, t_{lag}, showing a correlation of 0.70 with k_{obs}, while the elongation time constant, T gives a correlation of 0.98 (Fig. 5.9 **f)**). Thus, it is proposed that the monomer reduction observed in these experiments mainly describes both nucleation and elongation, since the rates of these processes are inherently linked, as described in Equation 5.3.

$$\mathrm{tau} + \mathrm{tau} \underset{k^1_{\mathrm{off}}}{\overset{k^1_{\mathrm{on}}}{\rightleftharpoons}} \mathrm{tau}_2 + \mathrm{tau} \underset{k^2_{\mathrm{off}}}{\overset{k^2_{\mathrm{on}}}{\rightleftharpoons}} \mathrm{tau}_n \tag{5.3}$$

Each of the experiments performed in the aptamer-based kinetics assay was performed in coated glass capillaries. To increase the number of simultaneous measurements, the system was also studied in a plate-based spectral shift setup, using 384 microplates in a Dianthus instrument as described in Section 2.2.4. Since the temperature control of this instrument was not capable of reaching 37 °C, the experiments were instead performed at 25 °C. As shown in Fig. 5.10 **a)** - **c)**, whilst the system shows a similar decrease in amplitude of the dose response curve over time, the binding isotherm does not reach saturation. This could be explained by the presence of DNAases and a decrease in the concentration of active DNA in the interaction or the possible adhesion of the protein or oligonucleotide to the surface of the plate. Although the absolute concentrations in the interaction are now only to be estimated, the change in ratio for the concentrations of aptamer that show significant amplitude changes can be evaluated over time, as shown in Fig. 5.10 **d)** - **f)**. The kinetic rate constants reported by the plate-based system were found as previously described by performing a global exponential fit for the first four concentrations. The fit value was found to be 0.04, 0.05 and 0.14, which showed a trend similar to that reported for capillary-based detection.

The aptamer-based assay was thus successfully applied to study the rate of early-stage fibrillization of tau, induced by heparin. The system proved sensitive enough to small variations in the fibril formation system, triggered by heparin concentration, and was seen to be most successful in the capillary-based set-up. Therefore, the applicability of the aptamer system to potential inhibitors will be assessed, in order to more closely study factors affecting tau oligomerization.

5.4 Monitoring effects of inhibitor compounds on tau fibrillization

To further test the robustness of the assay and explore factors affecting tau fibrillization, the assay was used to monitor the effect of several known inhibitors on aggregation. Because the assay is capable of reporting on the early stages of oligomerization, there is an opportunity to assess the effect of inhibitor compounds, reporting not only the ability to prevent large aggregates via thioflavin T assays but also by mediating dimer and small oligomer formation. The three main polyphenolic inhibitors used in the literature

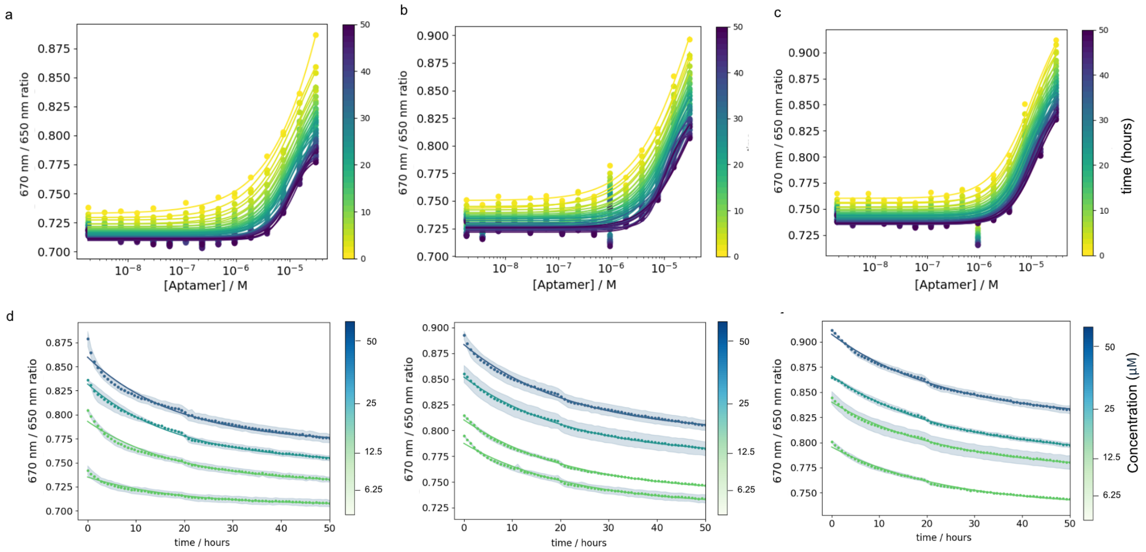

Figure 5.10: a) - c) The dose-response curve for 20 nM labeled tau against unlabelled aptamer within a total concentration of 2 µM tau, for heparin : tau ratios 0.3, 0.6 and 1 respectively, over 24 hours, at 25 °C in HEPES buffer (10 mM HEPES. 150 mM NaCl, 2 mM DTT, pH 7.5) **d)- e)** The change in ratio for the first 4 concentrations of aptamer are plotted over time and fitted to a single exponential fit. The value of k_{obs} is computed via a global fit as detailed in Section 2.4.2.

- curcumin, rosmarinic acid, and EGCG(-), as well as phenothiazine methylthioninium chloride (LMTM) and aminothienopyridazine (ATPZ) compounds were selected. Since LMTM is a reduced and more stable derivative of methylene blue, which has inhibitory effects above a molar ratio of 1:10 [216], it required more than 200 nM to be used in the assay. However, this compound produced a signal at 670 nm wavelength, even at 100 nM, and thus could not be used in the spectral shift assays, because of the strong autofluorescence. Thus, the viability of the other four compounds for use in the aptamer assay was determined by performing an interaction analysis between each compound and the 5'- Cy5 labeled aptamer - Aptamer C (Table 5.2). A dilution series of each compound was titrated against 50 nM of labeled aptamer, as seen in Fig. 5.11 **a)** - **d)**.

It was observed that aptamer binds with varying degrees of affinities to each of the polyphenolic compounds. The aptamer bound to curcumin with approximately 32 µM affinity, 80 µM affinity to rosmarinic acid, and 244 µM affinity to EGCG. However, the aptamer showed no reactivity towards the ATPZ compound. To proceed, the polyphenols were still assessed at concentrations lower than their respective affinity to the aptamer, given it was still in amounts necessary to perform its inhibitory function. EGCG typically requires high micromolar concentrations to inhibit tau fibrillization, but it has also been reported to inhibit oligomerization at substoichiometric concentrations [140]. In a recent study by Sonawane et al, EGCG was shown to have a half-maximal aggregation concentration (IC50) of 64.2 µM for tau aggregation. Therefore, this concentration was used in the aptamer assay. However, as seen in Fig. 5.12 **a)**, when EGCG was added to the assay, the interaction between tau and the aptamer is disrupted. EGCG is proposed to have multiple binding sites with tau, not only in the microtubule-binding region of the protein but also near the N - terminal [139]. The disappearance of the tau-aptamer interaction may thus be due either to EGCG binding to the tau in a region that hinders aptamer

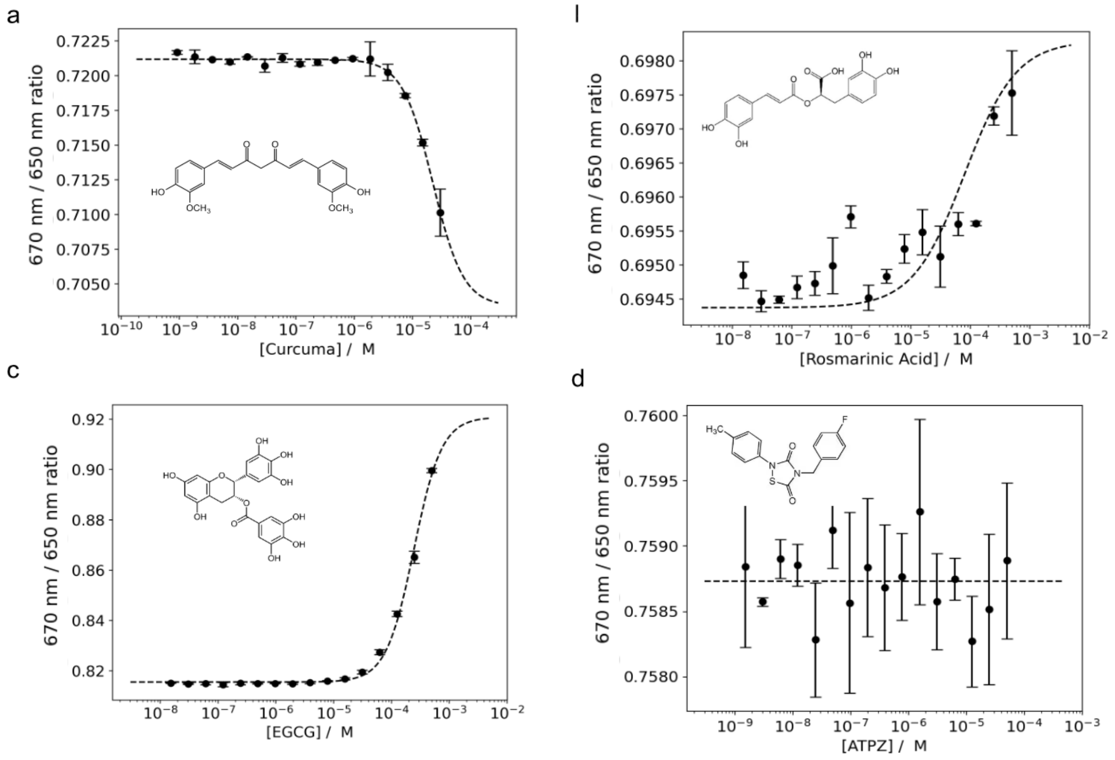

Figure 5.11: The interaction of the 5'-labeled aptamer with **a)** Curcumin **b)** Rosmarinic acid and **c)** EGCG(-) and **d)** APTZ are shown, together with the chemical structure of each inhibitor. Reactions are performed at 37 °C in HEPES buffer (10 mM HEPES, 150 mM NaCl, 2 mM DTT, pH 7.5).

binding, a change in the conformation of the protein after interaction with EGCG, or a possible interaction of the polyphenol with the aptamer. However, this compound could not be evaluated using the aptamer-based assay.

A similar effect could also be seen in using rosmarinic acid, which showed an unsaturated binding curve, as seen in Fig. 5.12 **b)**. Cornejo *et al.* reported that the IC_{50} of rosmarinic acid is estimated to be 7.7 μM [141], with up to 80% inhibition reported for 100 μM rosmarinic acid for 40 μM tau. Even at 10 μM, the compound hindered the binding of the aptamer to tau and therefore could not be evaluated in this assay.

However, the final polyphenol to be tested, curcumin, did not inhibit the tau-aptamer interaction. Curcumin requires approximately 5 μ M to observe inhibitory effects, Rane *et al.* [221] reported that the IC_{50} of curcumin is 10.6 μ M. The aptamer-based assay was performed in parallel to a thioflavin T assay. To work below the affinity measured with the aptamer, only 5 μM of curcumin was used in the assay. As shown in Fig. 5.12 **c)**, the interaction could be measured over time. The change in ratio was plotted over time, with the rate of decrease in amplitude being much reduced. As seen in Fig. 5.13 **a)**, a simple exponential equation could not be fitted to the observed changes in ratio, with the rate constant derived from this fit being 0.000003 h^{-1}. A thioflavin T assay was performed in parallel to this experiment, showing that heparin-induced fibrillization was indeed inhibited over time. A decrease in amplitude is observed, as well as a significant increase in the nucleation and elongation period (Fig. 5.13 **c)**). This is in agreement with the literature, with curcumin reported to reduce the rate of oligomerization [221], and even

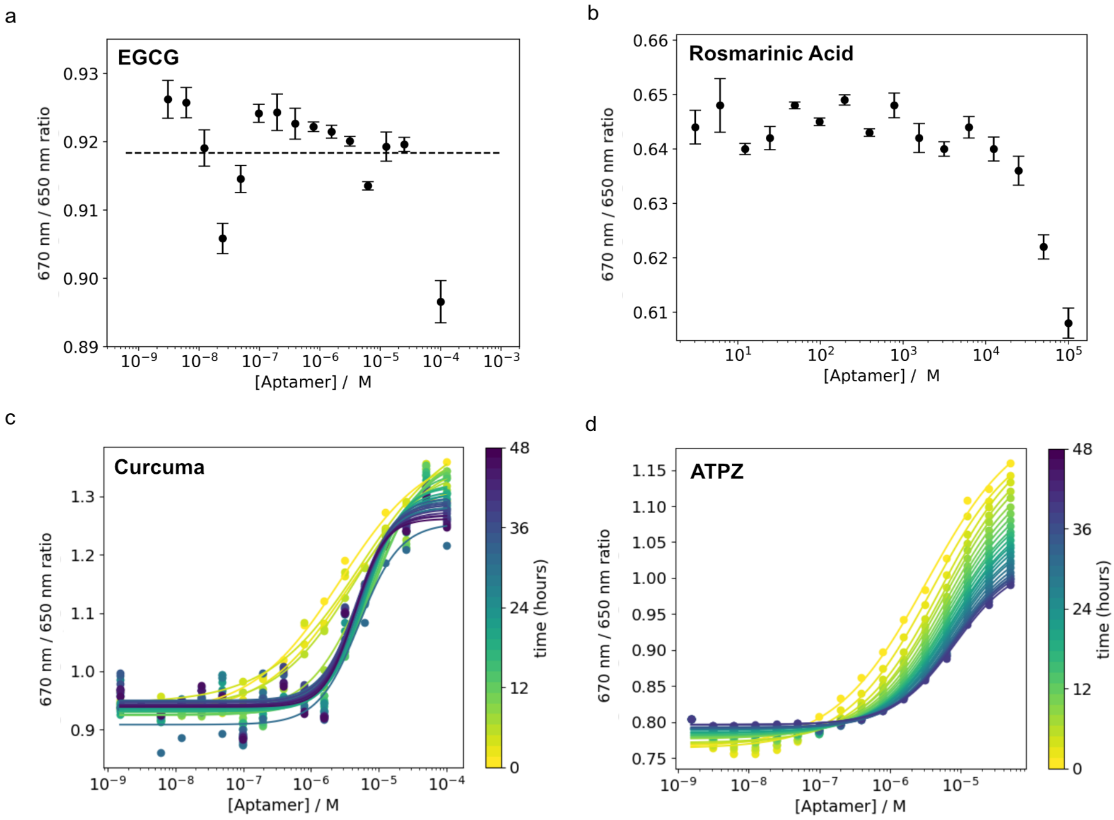

Figure 5.12: The interaction of 50 nM labeled tau, in the presence of 2 uM unlabelled tau, and heparin: tau ratio 0.8, are evaluated using spectral shift. Dose response curves for show binding of the aptamer to **a)** EGCG and **b)** Rosmarinic acid. However, **c)** Curcumin and **d)** ATPZ does not abolish the tau–aptamer interaction and is monitored over a period of 48 hours, at 37 °C in HEPES buffer (10 mM HEPES, 150 mM NaCl, 2 mM DTT, pH 7.5).

one study showed the ability to dissolve tau dimers [222]. Whilst the aptamer reports a decrease in the rate of oligomerization, irregular changes in amplitude observed in spectral shift assay could be due to either the interaction of curcumin with the aptamer, or possible precipitation in the capillaries.

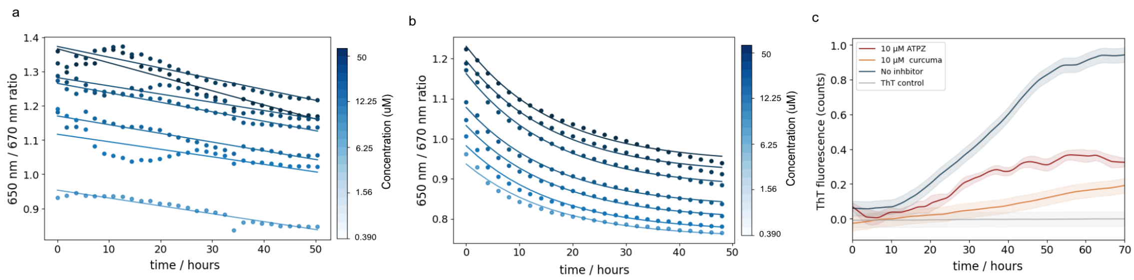

Figure 5.13: The change in ratio over time is evaluated by fitting to a single exponential function for a system inhibited by **a)** Curcumin and **b)** ATPZ **c)** Thioflavin T assays were performed at 37 °C in HEPES buffer (10 mM HEPES, 150 mM NaCl, 2 mM DTT, pH 7.5).

For ATPZ compounds, Ballatore *et al.* reported that the compound had an IC_{50} in the range of 1 -10 μM, but inhibited fibrillization most effectively when present in a 1:1 molar ratio with tau [223]. In this assay, 5 μM of ATPZ was used, and as seen in the thioflavin assay, it showed inhibition of fibrillation, with a 75% decrease in amplitude (Fig. 5.13 **c)**), as well as an increased nucleation phase (Fig. 5.12 **d)**). The aptamer-tau interaction over time was not affected by the compound, and remarkably, the rate of change in the ratio decreased compared to the uninhibited system (Fig. 5.3 **b)**). The observed rate constant, k_{obs}, decreased from 0.1 to 0.06 h^{-1}. This quantifiable decrease in the rate constant shows the ability of ATPZ to influence the formation of small oligomeric species, which is not as easily quantified in the ThT assay seen in Fig. 5.13 **c)**. While the applicability of the aptamer assay is currently limited to certain chemical groups, it offers the potential to quantify the effects of inhibitors at the beginning stages of the fibrillization process.

5.5 Conclusion

The assay developed and presented in this chapter aims to leverage the specificity and stability of aptamer-based systems. It was determined that the presence and position of a fluorophore on the aptamer can greatly affect the rate of association with a biomolecule. As such, consideration should be given to labeling approaches when studying interactions. The experiments performed with the differently labeled aptamers also allowed insight into the nature of the conformational change necessary for the aptamer to bind to tau, with the N-terminal region showing great significance. An assay using an unlabeled aptamer was then optimized to study interactions with tau, was successfully implemented in a real-time kinetic experiment, and was used to quantify the nucleation and elongation stages of tau fibrillization. The assay thus was able to successfully report on the early stages of oligomerization, and quantitatively look at monomer concentration, a feat not possible with the classical ThT method which relies on mature fibril formation. The aptamer system was also able to report on the effects of different concentrations of heparin on the rate of oligomerization. Although the aptamer is capable of binding to certain polyphenols, the use of the aptamer system can be further applied to studying the effects of different chemical classes of inhibitors as well as mutations of tau, and possible effects of post-translational modifications.

Chapter 6

Development of plasmon-enhanced fluorescence assays for spectral shift

The use of plasmonic effects of gold nanostructures to alter the emission properties of fluorophores has been widely documented [224, 225]. The process involves coupling of the electric dipole of a fluorophore with the enhanced localized electromagnetic field on a plasmonic metal surface [225]. This process, called localized surface plasmon resonance (LSPR), facilitates efficient and increased electron transfer within a fluorophore for improved spectral emissions. However, in most applications of LSPR, there are several factors that are judiciously controlled to allow efficient resonant energy transfer. Factors that affect fluorescence intensity address one or more of the following: an increase in the excitation decay rate; or an increase in the quantum yield that alters the ratio of radiative to non-radiative emission [226]. Most studies have looked predominantly at the effects of gold and silver nanoparticles and other nanostructures because the size, shape, and geometry of the metal affect their near- and far-field interactions with the fluorescent molecule. This is imperative since control of these factors affects whether enhancement or quenching occurs. Most importantly, many studies look at the effect of distance from the fluorophore, since too strong interactions cause electrons in the excited state to be extracted, even those required for radiative emission, resulting in quenching. However, an interaction that is too weak with the near-field does not enhance the dipole moment in the molecule [225]. In general, the fluorophore must be placed within wavelength scale distances from the metallic surface, for LSPR to occur [227]. Further optimization for enhancement includes the use of fluorophores that have spectral overlap with the plasmon resonant wavelength of the metal nanostructure [228]. As such, there is interest in using nanostructures whose dimensions and geometries optimize all of these factors. Much attention has been given, for example, to nanorods, which have been shown to have large enhancement factors for spectrally specific dyes, utilizing the increased near-field coupling of the longitudinal plasmonic wavelengths [229]. With the optimization of all of the factors mentioned, the development of a solution-based plasmonic enhancement strategy is possible.

Utilizing gold nanostructures as a coupling agent for fluorescent dyes is dependent on the creation of stable complexes which allow for controlled coupling of the dipoles, and thus far has been used in biosensing applications whereby immobilization of a fluorophore is

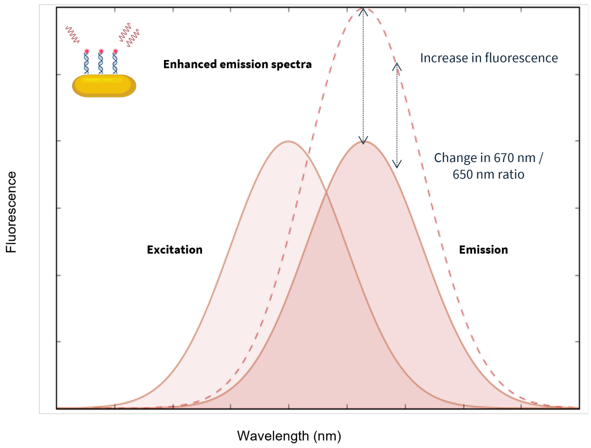

Figure 6.1: Fluorescence enhancement occurs upon the overlap of a plasmonic band of a nanorod to the emission peak of a fluorophore, which can be harnessed in spectral shift measurements.

performed through either adsorption or covalent coupling to a gold surface [230, 231]. It has also been documented that the plasmonic band of the gold surface is highly dependent on the properties of the functionalized molecule, such as length and density of coverage, with the absorbance spectra before and after functionalization exhibiting shifts [232]. The change in the plasmonic absorption band will therefore further affect the transfer to the fluorophore, introducing the possibility for observing quantifiable spectral changes not only in amplitude but peak position, for fluorophores on the surface of a gold nanostructure. With the propensity for increased fluorescence signal and spectral shift changes, there is an opportunity to achieve signal enhancement not only in the realm of increased signal-to-noise ratio values but in also achieving lower working concentrations for the spectral shift set-up currently used. This section of work aims to produce an aptamer-based gold nanorod system that is optimized for producing signal amplification in the detection of monomeric tau, using spectral shift assays.

This chapter will explore the use of three generations of oligonucleotide-AuNR conjugates, with the aim of producing amplified fluorescence spectral shift ratios. The first system, termed System A (Fig 6.2 **a)**) consists of the labeled aptamer ssDNA1 (Table 6.1), directly attached to the gold nanorod via a thiol linkage. The direct functionalization approach uses the single-stranded system to detect tau in solution. The second design, System B (6.2 **b)**) will instead use double-stranded system as the linker. In this design, the AuNR rod is instead directly functionalized with a Cy5 labeled ssDNA2 (Table 6.1) which is complementary to the aptamer. The unlabelled aptamer is then hybridized to the ssDNA2 to form a double-stranded complex. Finally, the third design, System C, as seen in Fig. 6.2 **c)** demonstrates the use of another dsDNA spacer, with a dangling aptamer, functioning as a DNA-nanoantenna. The AuNR is functionalized with a labeled spacer strand ssDNA4 (Table 6.1), which is then hybridized to ssDNA5 which consists of the aptamer and a complementary sequence to ssDNA4. The resulting plasmonic DNA-nanoantenna will then be used in spectral shift assays to detect tau in solution.

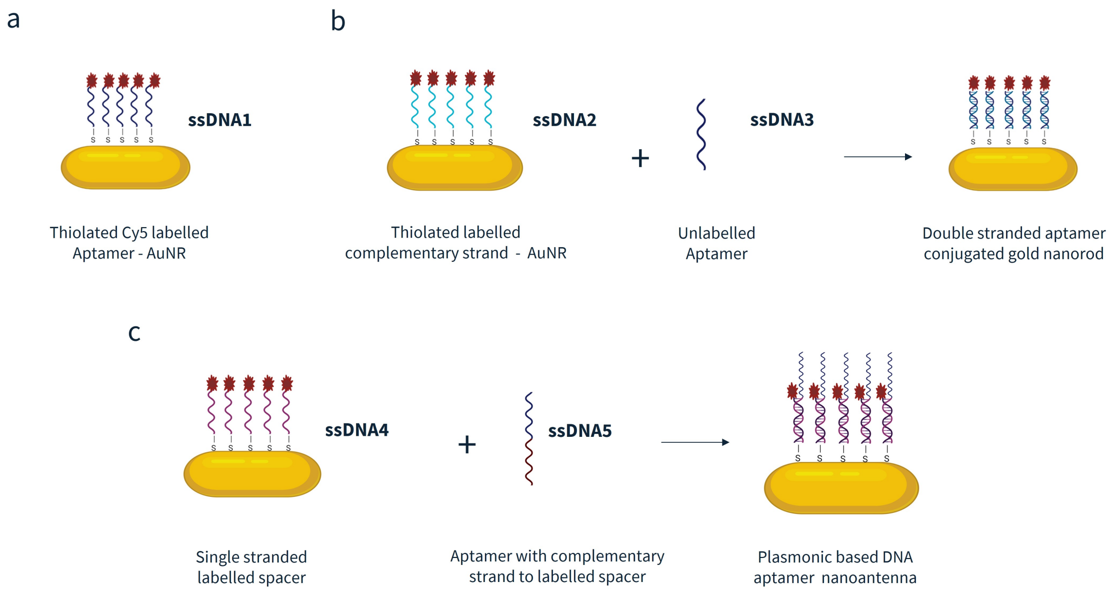

Figure 6.2: Three generations of DNA-AuNR conjugates are designed to explore signal amplification of fluorescence spectral shift assays. **a)** System A consists of the labeled aptamer conjugated to the AuNR via a thiol linkage **b)** System B uses a double-stranded DNA linker composed of an unlabelled aptamer and labelled complementary strand **c)** System C uses the dsDNA as a spacer, a dangling aptamer to create a DNA-nanoantenna.

Table 6.1: List of oligonucleotides used in plasmonic assays.

Oligonucleotide	Sequence (5’to 3’)
ssDNA1	Cy5 - TTGCGGAGCGTGGCAGGTT- SH
ssDNA2	SH-TTCCTTCCTCCGCAATAC - Cy5
ssDNA3	TTGCGGAGCGTGGCAGGTT- SH
ssDNA4	Cy5 - GTCCAGACTCTT - SH
ssDNA5	SH-TTGAGTCTGGACTTGCGGAGCGGGCAGG

6.1 Oligonucleotide functionalization of gold nanorods

Spectral shift optics record fluorescence emission at 650 and 670 nm of near-infrared dyes. Therefore, it was important to select a nanostructure that has a plasmonic absorbance peak with significant overlap with this range. Since most gold nanoparticles have plasmonic effects in the range of 450-550 nm, gold nanorods (AuNR) were instead chosen since the LSPR peaks can be tuned with the length of the nanorod. A nanorod of dimension 40 nm x 25 nm with an absorbance maximum of 660 nm was chosen. The chosen method for functionalizing gold nanorods with oligonucleotides requires the colloidal stability of the structure to be maintained during the ligand exchange process. The nanorods used in this experiment (Sigma Aldrich) were coated with cetyltrimethylammonium bromide (CTAB), which is a cationic surfactant that maintains the stability of the nanorods by electrostatic repulsion [233]. The displacement of this surfactant surface is most commonly performed using salt aging protocols, and depending on the covalent attachment method, it may also require several solvent exchange processes as described in round trip phase transfer protocols [234]. The salt aging step maintains stability by charge screening, by adding low millimolar increments of salt, over several hours, and requires the oligonucleotide to be present in great excess [235]. Instead, a pH-assisted functionalization method described in references [236, 237], was considered for an efficient and rapid ssDNA functionalization of the gold nanorod, which also required lower concentrations of oligonucleotides for loading. According to Shi *et al.* [237], functionalization can be performed at low pH, since CTAB-coated gold nanorods are more stable under acidic conditions than at neutral pH, even at high salt concentrations. They proposed that the surface becomes more positively charged, allowing for more efficient adsorption of negatively charged oligonucleotides. The study concluded that the more positively charged gold surface at low pH allows faster absorption of negatively charged oligonucleotides, resulting in a more efficient loading process. The approach has been used and adapted in several studies that vary in the use of surfactants and in the size and geometry of the gold nanostructure used [238, 239].

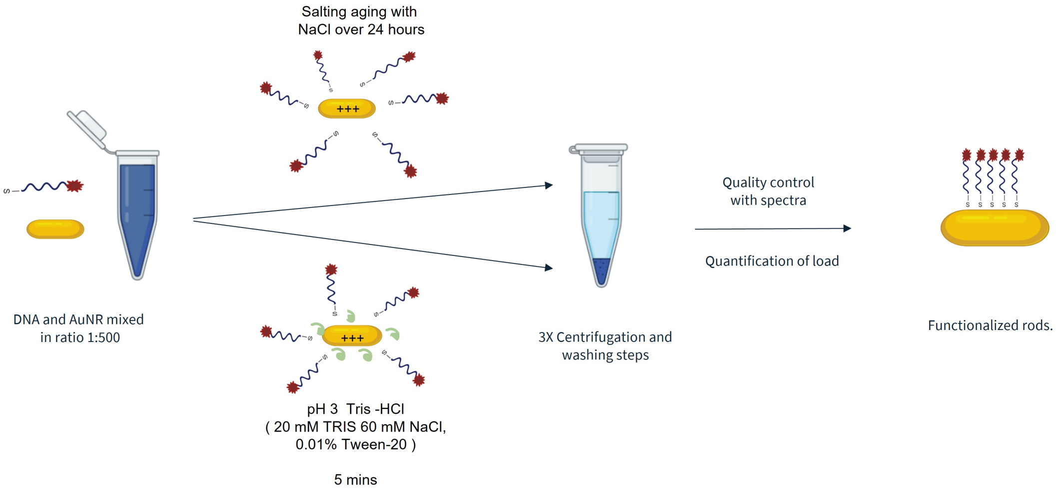

Figure 6.3: Schematic describing the two main routes for oligonucleotide functionalization of gold nanorods, through either pH-assisted DNA loading or the salt aging process.

Here, the methods described by [236, 237], were adapted for the functionalization of three different DNA-AuNR systems. The method described in Section 2.6.3, involves the reduction of thiolated oligonucleotides with TCEP, which is then removed prior to interaction with gold nanorods to prevent unwanted cleavage of thiol bonds. The activated oligonucleotides are added to the nanorods and dissolved in Tris buffer, which was then pH adjusted with the addition of HCl. The buffer was then supplemented with 30 mM NaCl to allow charge screening during the functionalization process. Although the use of a surfactant was not reported in the studies, the presence of Tween-20 was found to preserve the stability of the nanorods after the third washing step. The use of Tween-20 in interactions was also shown to be useful in eliminating the adsorption of nanorods to glass capillaries. After incubation, the complex was washed three times with repeated rounds of centrifugation and resuspended in Buffer A (20 mM TRIS, 100 mM NaCl, 1 mM EDTA, 0.01% Tween-20, pH 7.5). The resultant functionalized nanorods were characterized by evaluating the absorption spectra, as well as the size changes via dynamic light scattering.

6.2 Stability and interaction analyses of gold nanorod systems

The first system investigated, **System A**, involved the immobilization of the aptamer ssDNA1 6.1 directly on the surface of the gold nanorod. The aptamer was labeled at the 5′ end with a Cy5 fluorophore and at the 3′ end with a thiol linker, separated from the main sequence at either end with a polyT linker. System A was evaluated first to investigate the effect of the plasmonic surface on the binding of the aptamer to tau, as well as to determine whether fluorescence enhancement or quenching would be seen in this DNA-nanorod complex.

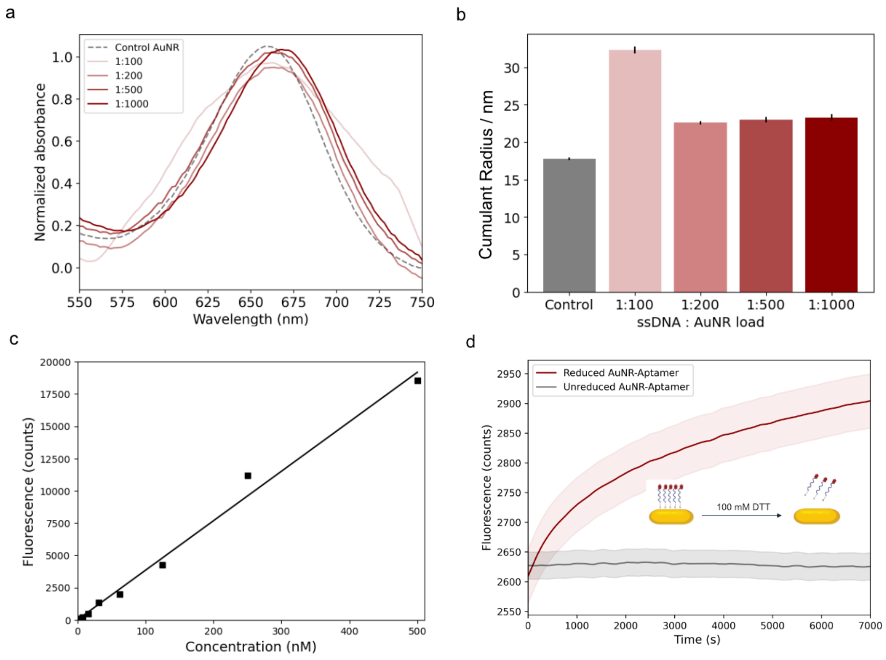

Figure 6.4: a) The minimum ssDNA load is determined by measuring the absorbance spectra at various loading ratios of AuNR : ssDNA. **b)** Dynamic light scattering performed in Prometheus Panta, in Buffer A reports of the size and stability of the ssDNA-AuNR complex, for each load ratio **c)** A calibration curve for free aptamer fluorescence at 10% excitation in the prototype Andromeda. **d)** To determine total DNA loading onto nanorods, the functionalized nanorods were reduced with 100 mM DTT causing aptamers to detach from the rod.

Table 6.2: Characterization of System A

AuNR : ssDNA	**FWHM (nm)**	**Emission Max (nm)**	**PDI**
Control	62	662	0.17
1:100	105	663.5	0.5
1:200	63.5	667	0.23
1:500	68	669	0.29
1:1000	72.5	671	0.30

The attachment load was optimized by mixing the gold nanorods with the aptamer in molar ratios of 1:100, 1:200, 1:500, and 1:1000. The optimum loading ratio was evaluated by monitoring the stability of the complex through two methods. The absorbance spectra were evaluated before and after functionalization, and a shift in the absorbance peak is seen after successful functionalization. Stability can be assessed by evaluating the broadening of the absorbance spectrum by calculating the full width at half maximum (FWHM) value (Table 6.2). As seen in Fig.6.4 **a)**, after adding 100 oligonucleotides per nanorod, the electrostatic stability of the complex is seen to be reduced with significant peak broadening and the appearance of a shoulder near the emission maximum at 662 nm. This abnormal shape is typical for colloidal instability and aggregation of nanorods [240]. The samples were also evaluated using dynamic light scattering, in which the size and polydispersity of the complexes are shown in Fig.6.4 **b)**. As such, the ratio of 1:500 was chosen to perform subsequent measurements. The fluorescence of the 1:500 aptamer-AuNR complex was compared with that of the free aptamer. It was shown that the fluorescence was quenched by 10%. The presence of quenching allowed quantification of the DNA load on the nanorod, by performing a ligand displacement protocol as described in reference [154], and detailed in Section 6.4. The functionalized nanorod is reduced in the presence of 100 mM DTT, after which the fluorescence is monitored over a period of 5 hours. The sample fluorescence increases because the DTT allows the quenched fluorophore to be released from the plasmonic near-field. The fluorescence after complete reduction is then compared against a calibration curve of free oligonucleotides, for which a linear relationship was derived. Similarly, the concentration of the gold nanorods after functionalization is determined by using the absorbance calibration curve. The loading efficiency was found to be 100 oligonucleotides on the surface of each nanorods (Fig. 6.4 **c)-d)**.

After the characterization of the aptamer-nanorod complex, the use of the quenched aptamer system in an interaction experiment with tau was evaluated. After determining the concentration of the labeled aptamer on each nanorod, 20 nM total aptamer was titrated against a dilution series of tau in buffer A. The dose response curve shows the presence of a low-affinity interaction as well as a high-affinity interaction (Fig. 6.5), and once again, a slow association of the aptamer to tau. Although the affinity of the aptamer on the gold nanorod to tau is around 1-2 μM in this system and buffer, the higher affinity interaction was suspected to be tau binding directly to the surface of the nanorod. This could be due to the presence of an available surface for binding, as a result of incomplete coverage of the oligonucleotides post-functionalization. This may be circumvented by increasing the DNA loading on the nanorod, but this was not pursued, since the change in the spectral shift ratio for the protein-aptamer interaction did not provide any signal amplification. Potentially, the single-stranded DNA system is unable to provide a structure that is rigid enough to provide control of the distance between the fluorophore and the gold surface. Therefore, a second system (**System B**) was developed, which used more rigid double-stranded DNA for functionalization.

System B used a complementary strand to the aptamer, ssDNA2 (Table 6.1), labeled with a Cy5 fluorophore, which was then hybridized to the aptamer to form a double-stranded DNA-AuNR complex as shown in Fig. 6.6 **a)**. Nanorod functionalization with ssDNA2 was performed in the same manner as described above and in Section 2.6.3. After quantification of the DNA load using the ligand displacement protocol, the complex was incubated for 30 minutes with varying known concentrations of the unlabeled aptamer. The

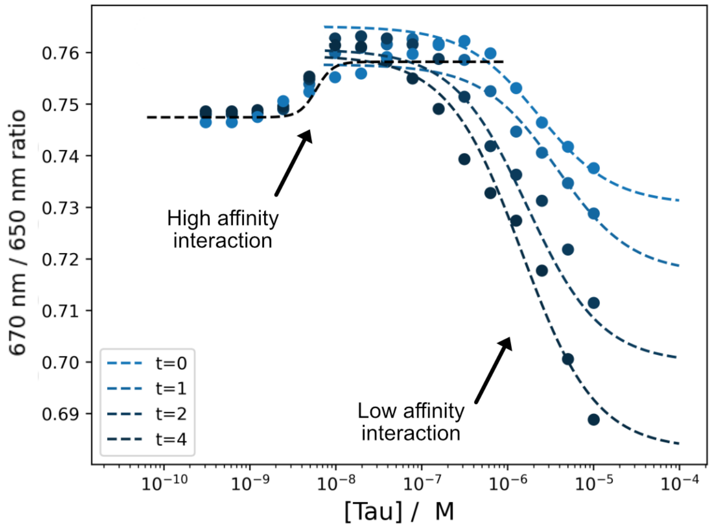

Figure 6.5: The spectral shift binding curves for system A and tau in Buffer A, over time shows slow association of the aptamer to tau, as well as the presence of a secondary high-affinity binding event.

fluorescence of the system increases dramatically once the ratio of AuNR-ssDNA complex to unlabeled aptamer reaches 1:1; in this case when the aptamer concentration has reached 20 nM. To quantify the degree of enhancement, the fluorescence of free ssDNA2 was compared with the AuNR complex, as seen in Fig.6.6 **d)**. The enhancement is approximately three fold, allowing the lowest concentration to be measured by the fluorescence detector in Monolith X to be $<$ 2 nM.

The presence of plasmonic fluorescence enhancement in system B is likely due to the upright structure of the duplexed system, which allowed for more rigid control of the distance of the fluorophore to the gold surface. To date in the literature, there has been a great dependence on the use of gold-composite structures, such as core-shell systems, which utilize a silica bilayer to allow isolation of the gold surface from the fluorophore [241–243]. Only a few reports of gold-nanorod systems that utilize DNA as linkers show fluorescence enhancement [244, 245]. In the study by Zhu *et al.*, the enhancement was achieved by using the hybridization of strands, each of which was attached to a different nanoparticle. The enhancement factor was 5 fold, with approximately 8.5 nm separation between the fluorophore and the gold surface, and involved the formation of an AuNP-dsDNA-AuNP composite [245]. The highest enhancement factor in the literature was reported in the study by Botequim *et al.*, which reported a novel method of directional functionalization of oligonucleotides on the tips of the nanorod. The enhancement factor observed here is more than 10 fold; this was explained by the presence of plasmonic hot spots at the tips of the nanorod, which allowed greater electromagnetic dipole coupling. In this work, the enhancement factor is only 2 fold but may be explained by the distribution of the oligonucleotides on the sides of the nanorod, which may not contribute to the overall enhancement factor or even potentially reduce it.

The functionality of the system was then further investigated by interacting the complex

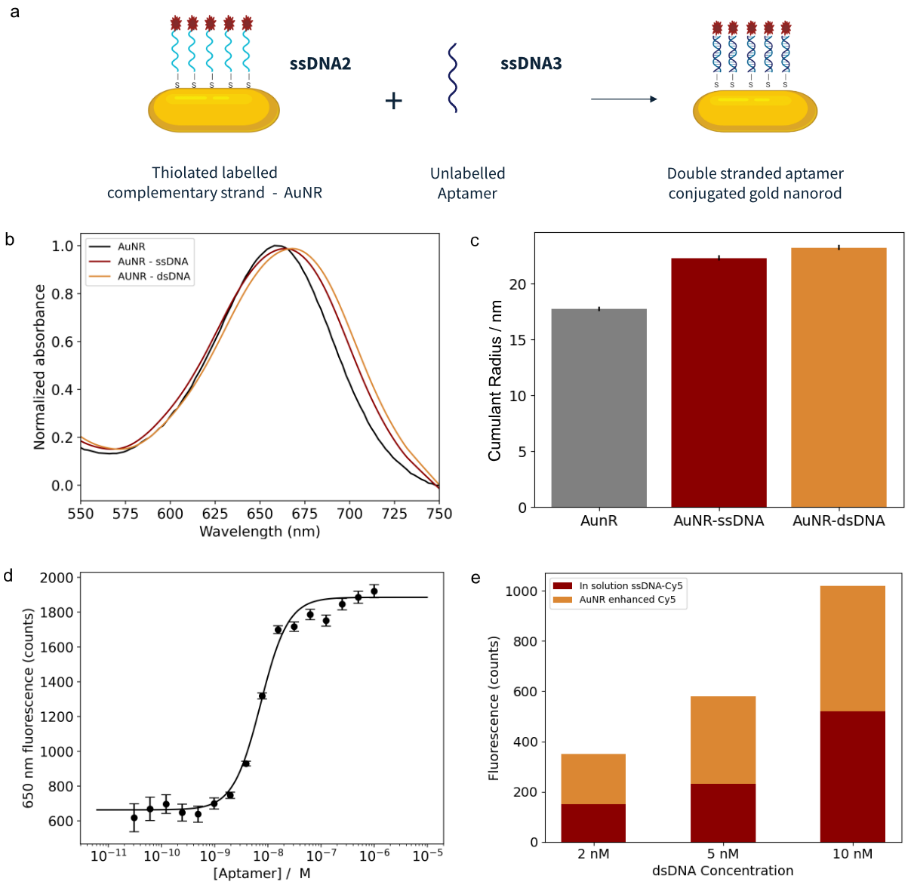

Figure 6.6: **a)** Schematic for System B, the formation of a double stranded DNA -AuNR complex **b)** the absorbance spectra are taken for the complex at each stage of functionalization, showing shifts in the attachment of the ssDNA (red) and subsequent hybridization to dsDNA (orange). **c)** Dynamic light scattering is used to monitor the change in the size of the AuNR before and after functionalization. **d)** The binding isotherm demonstrates the increase in fluorescence upon hybridization of the aptamer onto the ssDNA-AuNR system. **e)** Volume bar chart showing fluorescence of the dsDNA-AuNR system compared to the free oligonucleotides at different concentrations to show a fluorescence enhancement of 100%.

with tau. Interestingly, the presence of the secondary high-affinity interaction persists, even with the increased load of the now double-stranded functionalization (Fig. 6.7 **a)**). This hypothesis was then tested by performing a control titration of labeled tau against a dilution series of unfunctionalized gold nanorods. As shown in Fig. 6.7 **b)**, a hill fit of the dose-response curve shows a 4 nM nanomolar interaction between the tau and gold nanorods. Although this interaction could demonstrate an adsorption process, it is possible that the cysteines in the MTBR region of tau, which have been reduced in the presence of 2 mM DTT in the storage buffer, cause the activated thiols of the protein to interact with the surface of the gold.

6.2.1 Methods of passivation of oligonucleotide functionalized nanorods

In order to alleviate this effect, two approaches for surface passivation were considered. The first was to pegylate the surface of the gold nanorod prior to the functionalization process. Pegylation should maintain the stability of the system by providing steric stabilization and a protective layer to prevent the adsorption of charged biomolecules. There

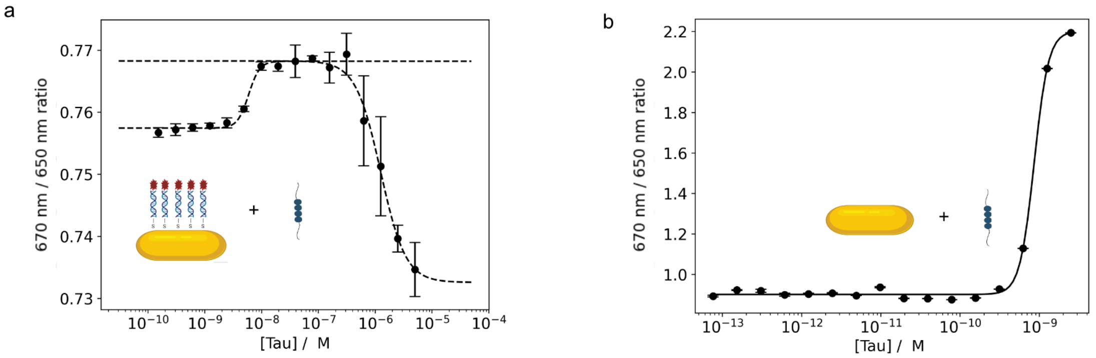

Figure 6.7: a) Spectral shift dose response curve of System B against tau in Buffer A, shows the presence of a high-affinity interaction and a lower-affinity interaction. **b)** Binding isotherm of labeled tau against gold nanorods shows a Langmuir isotherm describing the adsorption of tau onto the gold surface.

are several well-documented approaches to functionalizing nanostructures with PEG and oligonucleotides [155, 238, 246]. Li *et al.* developed an approach to rapidly functionalize gold nanorods in the presence of PEG and Tween-20, using low pH and a short salt aging process [155]. In this approach, pegylation is performed in the presence of Tween-20, which allows the displacement of CTAB while temporarily stabilizing the complex prior to the addition of oligonucleotides. This protocol was adapted as described in Section 2.6.3, using mPEG-SH (methoxy polyethylene glycol thiol). After pegylation and attachment of the oligonucleotide, pegylated System B was used again in an interaction against tau. However, mPEG-SH instead hindered tau interaction with the double-stranded oligonucleotide system as seen in Fig. 6.8 **a)**. Furthermore, the presence of fluorescence enhancement could no longer be observed, a finding which was also corroborated by Botequims *et al.* who performed a similar protocol in comparison to their site-directed approach [244].

The pegylation, therefore, reduced the number of available plasmonic hot spots, which were necessary to observe the 2-fold increase in fluorescence.

In order to circumvent the issue of the oligonucleotides competing with the passivation agent for the gold surface, a technique that allowed the passivation step post oligonucleotide functionalization was needed. This was achieved by using the ability of BSA to adsorb onto the surface of gold, which has been documented in several studies to occur with high affinity [247, 248]. To fully coat the surface of the AuNR complex, a 1000:1 BSA: dsDNA-AuNR molar ratio was used and the solution was incubated for an hour. The particles remained stable, prior to interaction with tau. As seen in Fig. 6.9 **a)**, the presence of the high-affinity binding site, before passivation (black), is reduced after passivation (dark red). However, over time, as the double-stranded complex became unstable, Fig. 6.9 **b)**. It is proposed that upon binding to the aptamer, the double-stranded system dissociates, and the electrostatic stability of the complex is reduced. The breakage of the duplex structure by tau was first identified in a study by Krylova and co- workers [210]. Therefore, if the aptamer does leave the surface of the nanorod post-tau interaction, then the AuNR complex becomes unstable.

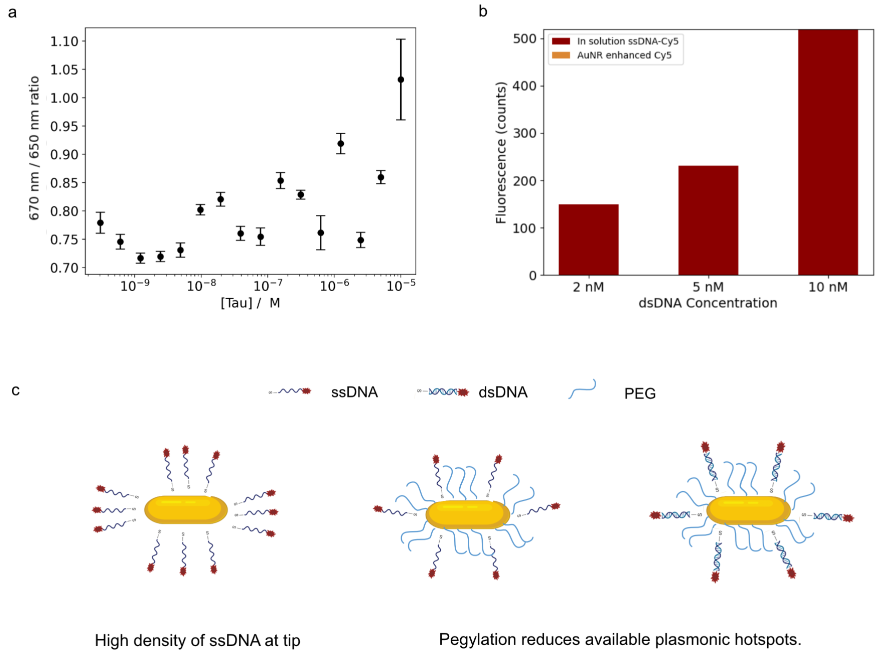

Figure 6.8: a) Spectral shift signal of mPEG-SH functionalized System B against tau in Buffer A, shows the steric hindrance of PEG on the interaction. **b)** The pegylated systems show no fluorescence enhancement using pegylation procedure. **c)** A schematic depicting the mechanism by which PEG influences the tau-aptamer interaction and aptamer-AuNR functionalization.

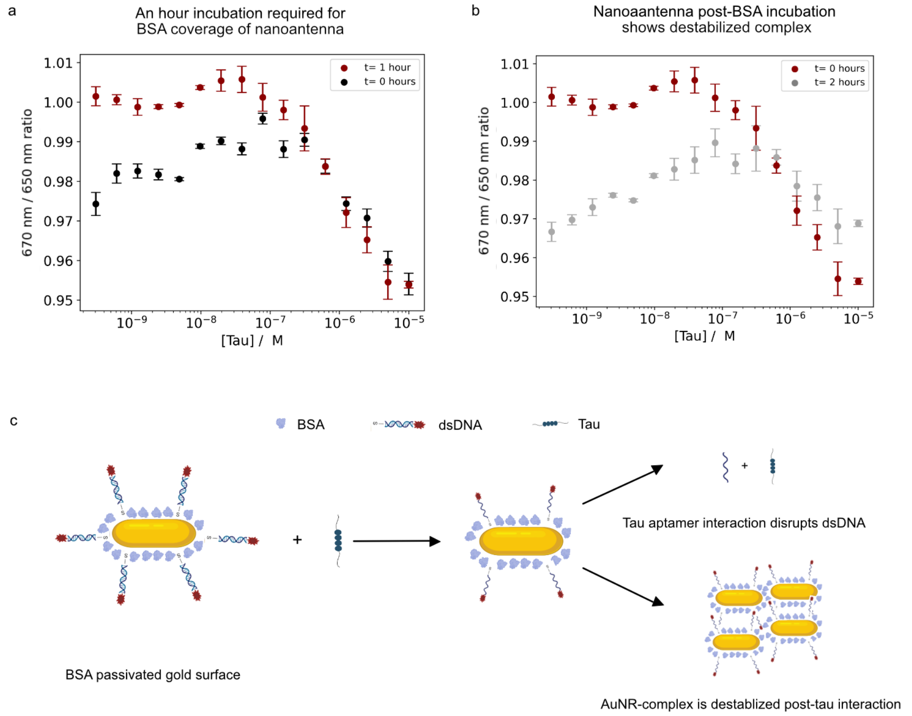

Figure 6.9: a) Spectral shift dose-response curve of System B against tau in Buffer A. BSA passivation reduces the appearance of the high-affinity binding of tau onto the AuNR surface. **b)** The complex begins to destabilize over time (gray). **c)** The proposed mechanism for the instability of System B after binding to tau is described in the schematic.

6.2.2 BSA - passivated DNA plasmonic nanoantenna

It is imperative to design an AuNR complex, which allows for stable tau-complex formation where the signal changes are due only to the tau-aptamer interaction. Therefore, a new system, **System C** was designed in which the AuNR complex functions as a DNA nanoantenna (Fig. 6.10 **a)**). The system is composed of a thiolated ssDNA4 (Table 6.1) with a fluorophore-conjugated after a polyT spacer. This strand was functionalized via the pH-assisted method as demonstrated with system A. The second strand ssDNA5, which consisted of the tau aptamer and a complementary sequence to ssDNA4, was then hybridized onto the AuNR system. This allows the fluorescence enhancement of the double-stranded system to complement the aptamer binding functionality of the AuNR complex. Since BSA passivation eliminated tau adsorption onto the surface of the gold, the same protocol was implemented in System C. As seen in Fig. 6.10 **b)** and **c)**, at each stage of functionalization, the system remains colloidally stable.

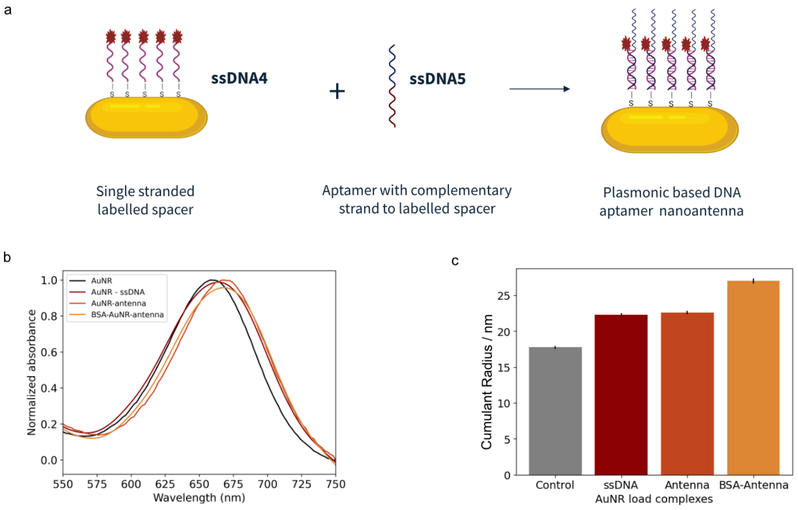

Figure 6.10: **a)** Schematic of System C, in which a dsDNA-AuNR complex is used to create a plasmonic DNA nanoantenna. **b)** The absorbance spectra for the functionalized AuNR system shows stable complex formation after the addition of each oligonucleotide and BSA passivation. **c)** Dynamic light scattering shows the increase in size of the complex after each functionalization step.

The functionality of a BSA passivated System C nanoantenna system could be tested in an interaction assay with tau. For this interaction, 25 nM of the labeled System C AuNR complex is titrated against tau, in Buffer A. As shown in Fig. 6.11, the nanoantenna interacts with tau, with a dose-response curve of amplitude greater than 0.5 (compared to labeled tau assay value of 0.25), indicating a significant amplified signal. The plasmonically coupled environmentally sensitive fluorophore is, therefore, able to detect changes in the binding of the aptamer to tau because of its proximity to the binding event, as well as to spectral shifts that are incurred due to changes in the plasmonic absorption band and the surface modification upon tau binding. The two effects amplify the spectral shift response, whilst allowing the investigation of a binding interaction in which either interaction partner is unlabeled. The dissociation constant for the process reported by this system is 550 nM, which is in the range of the value reported in the labeled tau assay.

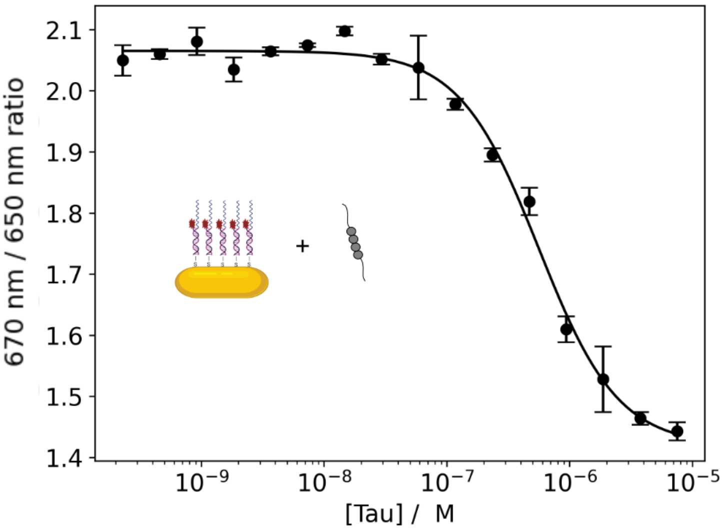

Figure 6.11: Spectral shift is used to obtain a dose-response curve of 25 nM BSA-passivated plasmonic DNA nanoantenna, titrated against tau in Buffer A. The K_d was determined to be 500 nM. LED excitation 20%

Although the system was able to provide an improved signal-to-noise ratio, the capability for kinetic measurements was also investigated to elucidate whether the system could also report fibrillization of tau.

The system was used to study heparin-induced fibrillization using a heparin : tau molar ratio of 1:1 as in Section 5.3, and using a lower concentration of System 3. The interaction was monitored over a 20-hour period, using spectral shift (Fig. 6.12 **a)**). However, it is seen that over time, the ratio of each data point decreases. The decrease is higher for lower tau concentrations and smaller for higher tau concentrations as seen in Fig. 6.12 **b)**. However, a decrease in amplitude is not expected for fibrillization detection using this system since bound states have lower ratio values. It is likely that the system is destabilized over time, due to the consistent irradiation by the LED. To test this, samples without tau were irradiated at two different LED excitation powers. The decrease in the recorded ratio was more significant for 60 % excitation, which was used for the fibrillization experiment, than it was for 20 % excitation. The irradiation of the nanorods could induce the plasmonic photothermal effect, in which near-IR light causes localized heating of the surface of the gold nanoparticle [249]. The localization of this effect was tested by shifting the capillaries after consistent excitation with LED. The ratio values returned approximately 80% of the original values as seen in Fig. 6.12 **c)**.

Therefore, it was determined that the constant measurement of the AuNR complex is likely not suitable for fibrillization measurements. However, since a correction factor was obtained for the change in ratio over time, the data could be corrected to see changes in the ratios for each concentration of tau. As expected, higher concentrations of tau showed an increase in the ratio over time (Fig. 6.12 **d)**). An exponential fit of the data allowed a k_{obs}, value of 0.16 $h^{-1}$to be determined, which aligned with the aptamer-based assay. In order to further validate the use of this assay, end-point measurements were also

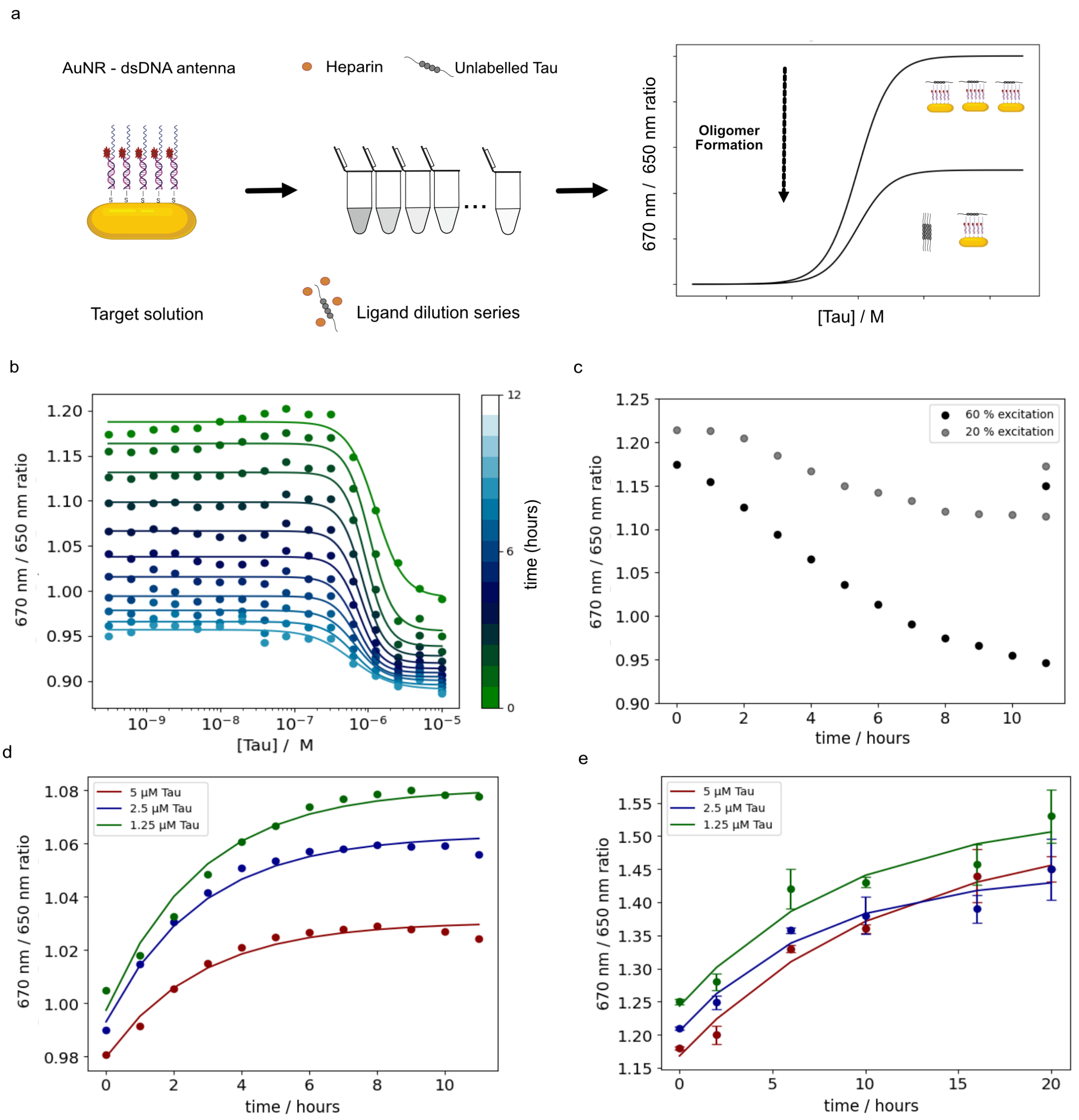

Figure 6.12: a) The dose-response curve of tau titrated against the plasmonic nanoantenna system in Buffer A. **b)** The effect of LED excitation on localized photothermal effect is seen in changes in ratios over time **c)** A corrected kinetic profile for the three highest concentrations of tau, which fibrillized in the presence of heparin. The apparent k_{obs}, is 0.16 h^{-1}. **d)** Endpoint measurements were performed in order to verify the efficacy of the assay. The apparent k_{obs}, is 0.12 h^{-1}.

performed in which a tau was fibrillized in the presence of heparin, aliquots of which were subsequently used to perform a series of dilutions at 6-time points. The AuNR complex was then mixed into the dilution series and the spectral shift ratios were obtained. Once again, the ratio values against time were fitted with a single exponential to derive a value for k_{obs}, which was calculated to be 0.12 h^{-1} (Fig. 6.12 **e)**). Although the plasmon-enhanced assay was not found to be ideal for real-time kinetics measurement using spectral shift, the endpoint assay in fact produced a maximum delta ratio change of more than 0.25 as compared to the real-time aptamer-based system reported in the previous section, which gave a signal change of 0.15. As such, the use of gold nanorod-coupled systems presents significant promise in the evaluation of interactions, with improved signal-to-noise ratios.

6.3 Conclusion

Oligonucleotide-gold nanorod systems were evaluated in the development of plasmon-enhanced spectral shift assays. It was shown that while single-stranded DNA-AuNR conjugates created a quenched fluorophore-coupled system, the use of double-stranded DNA systems allowed a fluorescence-enhanced system. The use of dsDNA as a linker allowed for a two-fold increase in fluorescence intensity. While several approaches to passivation were attempted, it was found that post-oligonucleotide functionalization passivation was necessary to maintain the stability of the AuNR complex, whilst allowing fluorescence enhancement. Whilst the double-stranded system produced enhancement, its stability post-tau interaction could not be maintained. As such a third design which involved the use of a DNA antenna, affixed the aptamer to the gold surface, post-interaction with tau. The novel BSA passivated DNA-gold nanorod plasmonic antenna system produced high signal-to-noise ratios in spectral shift assays. Whilst continuous real-time kinetics is hindered by the photothermal heating of the gold nanorods, the possibility of the use of plasmonics in spectral shift systems can be harnessed for interaction analyses, with the DNA antenna system offering the possibility of performing a measurement without placing a fluorophore on either interaction partner.

Chapter 7

Conclusion and overview

Neurodegenerative disease research has experienced significant advances in the last 20 years. The three main advances, discussed at the beginning of this thesis: the neurotoxic effects of tau oligomers as opposed to their fibrillar forms, the discovery of the heterogeneous nature of fibrillar aggregates of different pathologies, and the propensity for tau to form biomolecular condensates, have each significantly influenced the directions of therapeutic approaches to neurodegenerative diseases. These advances in our understanding of tau-based disease specifically highlight the need for multi-faceted therapeutic approaches, which can target different assembly states of tau. This thesis has highlighted the importance of monitoring processes implicated at the early stages of tau assembly, through in-solution, fluorescence-based methods at pathologically relevant concentrations. The motivation was to push forward the state of the art of *in vitro* approaches to monitoring both tau oligomerization and phase separation, to platforms that facilitate high data resolution and even high-throughput measurements of conditions surrounding these processes.

The driving forces behind the liquid-liquid phase separation of tau have been widely documented, with its pathological relevance being investigated. Whilst there may be an overlap in the conditions governing fibrillization and phase separation, it is still yet uncertain if these two aberrant processes occur concomitantly. The method developed in this work highlights the need to expand the biophysical toolbox used to study phase separation *in vitro*, such that large-scale screenings can be implemented to not only monitor conditions promoting LLPS but to allow for inhibitor library screens that facilitate a dual-therapeutic approach to NDs. It was shown that intrinsic and extrinsic fluorescence can be used as reliable reporters for detecting these temperature-dependent phase transitions. Thus far, such a large-scale study has not been conducted, holding the potential to test the effects of post-translational modifications and mutations on LLPS. Furthermore, the use of both intrinsic and extrinsic fluorescence allows the possibility of a large number of small molecule inhibitors to be tested, regardless of their spectral properties.

With the capacity for producing large amounts of data in high-throughput approaches, the need to develop analysis methods to sort through relevant data becomes increasingly important. The methods presented in this thesis represent an application of common approaches for analyzing trends in these large datasets of LLPS data. Dimension reduction techniques, such as PCA, can be applied to traces to derive shape parameters describing phase transitions for both protein and nucleic acid systems. In this work, the use of such algorithms was able to accurately represent the propensity for phase separation of a system, by showing relationships between a given PCA component and a varied physical parameter. This form of analysis offers a unique way of identifying the main variances in a set of traces and creating classifications that allow the user to visualize the effect of experimental variables. The work conducted in the thesis introduces the concept of using shape parameters as a foundation for feature selection in traces. This idea can be developed in various avenues as discussed in Chapter 3. For instance, for a tau-PEG system, the UCST behavior has been well characterized using the fluorescence approaches described in this thesis. This can be used to develop an approach to classify traces by comparing them to a standardized trace. Whether through Procustes analyses or through correlations, there exists a whole realm of approaches that may extend the qualitative value of large datasets.

High-throughput characterization of biomolecular condensates is becoming of particular interest in the world of drug discovery. Condensate-targeting drugs are now being proposed as a paradigm-shifting approach to therapeutics in cancer, neuromuscular diseases, neurodegenerative diseases, and even virology. The premise behind this approach is that biomolecular condensates hold druggable candidates that have been challenging to target. It was discovered by Brangywnne and coworkers for instance that certain cancer-targeting drugs become more localized in condensates with a transcriptional cofactor, allowing it to localize with its target [250]. However, another drug was expelled from condensates holding its target when a specific mutation was present in the protein. Since this discovery, several studies, as well as industrial collaborations have aimed to characterize not just the behavior of target proteins, but the behavior and constituents of disease-mediating condensates. The experimental techniques and approaches to data handling presented in this thesis hold remarkable potential for accelerating research in condensate modifying therapies.

The other avenue of biophysical characterization developed in this thesis was quantitative, in-solution, real-time detection aptamer assay. Oligomers of tau are being considered a relevant druggable target, with current high-throughput *in vitro* assays being evaluated with thioflavin t assays, monitoring mature fibril formation. The concept of the affinity-based assay relied on quantitatively studying the early oligomerization of tau, and developing a method to detect the processes usually missed in the lag phase of an assay. The aptamer detection system was used to study the effect of inducer concentration on oligomerization, as well as several small molecule inhibitors. This assay can be further applied to various other tau constructs, as well as to other factors affecting the fibrillization process such as pathological modifications, or mutations commonly observed in ND patients. The concept can even be extended to other intrinsically disordered proteins, involved in neurodegenerative diseases, such as α-synuclein, TDP-43, and amyloid-β for which relevant aptamers have been identified. Furthermore, if the known oligomeric species can be used in the aptamer selection process, the assay can inform on the time scale for small oligomer formation.

The versatility of aptamer-based detection was also shown to lend itself to the adaptation of a novel in-solution plasmonic nanoantenna assay. The gold nanorod-DNA conjugate assay was capable of providing signal amplification to fluorescence spectral shift assays. This system was able to produce a 2 fold fluorescence increase, using double-stranded DNA as a linker to control the distance between the gold surface and fluorophore. Whilst the continuous, long-term localized heating of the nanorods renders them unreliable for kinetic measurements, these assays can prove useful in evaluating interactions at lower concentrations than is possible with the current setup, without the need for labeling an interaction partner. This assay can be further optimized by using core-shell, or even silica-coated nanostructures, to achieve the spacing requirement for plasmonic enhancement. If this is done, then different surface functionalizations can allow the use of this in-solution plasmonic system to be used with proteins.

It is hoped that the methods developed in this thesis can be used to push forward the understanding of neurodegenerative diseases. However, the applicability of each of the experimental and data analysis techniques is far-reaching and can be used as a framework for assay and method development in various other forms of biophysical and biochemical analyses.

Appendix A

LLPS Data Analysis

The following are Python scripts implemented in Jupyter Notebook which document the various data analysis techniques used in monitoring phase separation processes of tau. Each script lists the dependencies required to run the script, and in-line comments to describe the steps in each stage of the analysis.

A.1 Smoothing Algorithm

This script documents the smoothing algorithm used on the fluorescence-temperature traces. The LOWESS filter, performs local moving averages, for neighboring points along the trace, to decrease noise on the sample. The smoothing algorithm is performed before performing calculations of onset and inflections points as well as prior to applying the PCA algorithm.

```python
#!/usr/bin/env python
# coding: utf-8

# In[ ]:


import pandas as pd
import numpy as np
import matplotlib.pyplot as plt


def lowess(x, y, f = 2.0 / 3.0, derive = True):
    """Lowess smoother: Robust locally weighted regression.
    """
    if isinstance(x, (list, np.ndarray)) and isinstance(y, (list, np.ndarray)):
        x = np.array(x) if isinstance(x, list) else x
        y = np.array(y) if isinstance(y, list) else y
    else:
        raise TypeError

    n = len(x)
    r = int(np.ceil(f * n))

```

```
    if n != len(y):
        raise ValueError('Length of x and y differ')
    if n == 0:
        return np.ndarray([])
    if r >= n or r <= 2:
        if derive:
            return np.insert(np.diff(y), 0, 0)
        return y

    x_mat = np.abs(x - x.reshape((n, 1)))
    h = np.sort(x_mat, axis=1, kind='mergesort')[:, r]

    w = np.transpose(x_mat) / h
    w.clip(0.0, 1.0, out=w)
    w = 1 - w * w * w
    w = w * w * w
    if derive:
        w = np.ceil(w)

    w_y = w * y[:, None]
    w_x = w * x[:, None]
    w_xy = w_x * y[:, None]
    w_xx = w_x * x[:, None]

    sum_w_y = np.sum(w_y, axis=0)
    sum_w_x = np.sum(w_x, axis=0)

    sum_w_xy = np.sum(w_xy, axis=0)
    sum_w_xx = np.sum(w_xx, axis=0)
    sum_w = np.sum(w, axis=0)

    slope = (sum_w_xy * sum_w - sum_w_x * sum_w_y) / (
        sum_w_xx * sum_w - sum_w_x * sum_w_x
    )
    if derive:
        return slope

    yest = slope * x + (sum_w_y - sum_w_x * slope) / sum_w
    return yest
```

A.2 Image Analysis

The image processing pipeline used to determine the size of droplets relied on the OpenCV python library. The script documents the process of segmentation and contour mapping to identify droplets in the image. The output of the script is the number and average size of the particles.

```python
#!/usr/bin/env python
# coding: utf-8

# In[9]:


import pandas as pd
import numpy as np
import seaborn as sns
import matplotlib.pyplot as plt
import cv2
import numpy as np
import pylab

# Kmeans
def kmeans_color_quantization(image, clusters=8, rounds=1):
    h, w = image.shape[:2]
    samples = np.zeros([h*w,3], dtype=np.float32)
    count = 0

    for x in range(h):
        for y in range(w):
            samples[count] = image[x][y]
            count += 1

    compactness, labels, centers = cv2.kmeans(samples,
            clusters,
            None,
            (cv2.TERM_CRITERIA_EPS + cv2.TERM_CRITERIA_MAX_ITER, 10000,
    0.0001),
            rounds,
            cv2.KMEANS_RANDOM_CENTERS)

    centers = np.uint8(centers)
    res = centers[labels.flatten()]
    return res.reshape((image.shape))


# In[15]:


# Load image
image = cv2.imread('pythontestr1.jpg')
original = image.copy()
h, w, c = image.shape
```

```
print("Dimensions of the image is:nnHeight:", h, "pixelsnWidth:", w, "
    pixelsnNumber of Channels:", c)


# In[16]:



# Perform kmeans color segmentation, grayscale, Otsu's threshold
kmeans = kmeans_color_quantization(image, clusters=2)
gray = cv2.cvtColor(kmeans, cv2.COLOR_BGR2GRAY)
thresh = cv2.threshold(gray, 0, 255, cv2.THRESH_BINARY + cv2.THRESH_OTSU)
    [1]

# Find contours, remove tiny specs using contour area filtering, gather
    points
points_list = []
size_list = []
cnts, _ = cv2.findContours(thresh, cv2.RETR_EXTERNAL, cv2.
    CHAIN_APPROX_SIMPLE)[-2:]
AREA_THRESHOLD = 2
for c in cnts:
    area = cv2.contourArea(c)
    if area < AREA_THRESHOLD:
        cv2.drawContours(thresh, [c], -1, 0, -1)
    else:
        (x, y), radius = cv2.minEnclosingCircle(c)
        points_list.append((int(x), int(y)))
        size_list.append(area)

# Apply mask onto original image
result = cv2.bitwise_and(original, original, mask=thresh)
result[thresh==255] = (36,255,12)

# Overlay on original
original[thresh==255] = (36,255,12)

print("Number of particles: {}".format(len(points_list)))
print("Average particle size: {:.3f}".format(sum(size_list)/len(size_list))
    )

# Display
plt.imshow(kmeans)
```

Appendix B

Interaction Analyses

B.1 Hill and Langmuir Fits for Monolith X

```python
#!/usr/bin/env python
# coding: utf-8

# In[ ]:


import pandas as pd
import numpy as np
import seaborn as sns
import matplotlib.pyplot as plt
import scipy.optimize
from scipy.optimize import curve_fit
import matplotlib as mpl


# In[ ]:


#Define functions needed for Langmuir and Hill fits.

def kd_function(x, unb, b, kd, target, r=1.0):
    fb = (x + target + kd - np.sqrt((x + target + kd) ** 2 - 4 * x * target)) / 2 / target
    return (unb + fb * (b * r - unb)) / (1 + fb * (r - 1))


def hill_function(x, unb, b, ec50, n, r=1.0):
    fb = 1 / (1 + (ec50 / x) ** n)
    return (unb + fb * (b * r - unb)) / (1 + fb * (r - 1))


def langmuir_fit(x1, x2, target, r=1.0):
    x1 = x1 * 1e9  # avoid floating point errors from very low concentrations

    mid = (x1[0] * x1[-1]) ** 0.5
    if not target:
        p0 = (x2[0], x2[-1], mid, 1)  # best guess
```

```
        try:
            (unbound, bound, Kd, target), pcov = curve_fit(lambda x, unb, b, kd, tar: kd_function(x, unb, b, kd, tar, r), x1, x2, p0,
                                                           bounds=((0, 0, 1e-3, 1e-2), (np.inf, np.inf, 1e9, 1e4)))
        except Exception as ex:
            print(ex)
            target = 1e-2
    else:
        target = target * 1e9

    p0 = (x2[0], x2[-1], mid)
    try:
        (unbound, bound, Kd), pcov = curve_fit(lambda x, unb, b, kd: kd_function(x, unb, b, kd, target, r), x1, x2, p0,
                                               bounds=((0, 0, 1e-3), (np.inf, np.inf, 1e9)))
    except Exception as ex:
        print(ex)
        return None, None
    else:
        popt = unbound, bound, Kd, target, r
        residuals = get_residuals(x1, x2, kd_function, popt)
        s_to_n = calculate_s_to_n(residuals, popt, len(x1))
        return (unbound, bound, Kd * 1e-9, target * 1e-9, r), s_to_n


def hill_fit(x1, x2, r=1.0):
    x1 = x1 * 1e9  # avoid floating point errors from very low concentrations

    mid = (x1[0] * x1[-1]) ** 0.5
    p0 = (x2[0], x2[-1], mid, 1.8)
    try:
        (unbound, bound, EC50, N), pcov = curve_fit(lambda x, unb, b, ec50, n: hill_function(x, unb, b, ec50, n, r), x1, x2, p0,
                                                    bounds=((0, 0, 1e-2, 0.2), (np.inf, np.inf, 1e9, 20)))
        popt = unbound, bound, EC50, N, r
        residuals = get_residuals(x1, x2, hill_function, popt)
        s_to_n = calculate_s_to_n(residuals, popt, len(x1))
        return (unbound, bound, EC50 * 1e-9, N), s_to_n
    except Exception as ex:
        print(ex)
        return None, None


def get_residuals(x1, x2, function, popt):
    return sum([(x2 - function(x1, *popt)) ** 2 for x1, x2 in zip(x1, x2)])


def calculate_s_to_n(residuals, popt, n):
    return round(abs(popt[0] - popt[1]) / (residuals / (n - 1)) ** 0.5, 1)

```

```python

# In[ ]:


#Load exported Monlith X raw data file. Define numpy arrays for concentration and ratio values.

Sample =pd.read_excel("heparincontrol.xlsx",sheet_name='Sheet1')
err=np.array(Sample.error)
y=np.array(Sample.ratio)
x=np.array(Sample.concentration)


# In[ ]:


target = 20e-9 #Define target concentration in nanomolar units, when needed for fit.

#Select if a hill or langmuir fit is needed.
popt, s_to_n = langmuir_fit(x, y, target, 1)
popt, s_to_n = hill_fit(x, y, 1)

xx = np.logspace(np.log10(x[0] / 1), np.log10(x[-1] * 1), num=100)  # evenly spaced x-values
yy = [hill_function(c, *popt) for c in xx]

#Plot the raw data points
plt.scatter(x, y, color='k')
#Plot fit of data.
plt.plot(xx, yy, color='black')
#Plot error bars
plt.errorbar(x,y, yerr=err, fmt='o', capsize=5,color='black')

plt.xlabel('Concentration /  M',fontsize=14)
plt.ylabel('650 nm / 670 nm ratio',fontsize=14)
plt.xscale('log')
plt.tick_params(axis ='x',labelsize=14)
plt.tick_params(axis ='y',labelsize=14)

plt.show()
```

B.2 Kinetic Analyses

```python
#!/usr/bin/env python
# coding: utf-8

# In[ ]:


import pandas as pd
import numpy as np
import seaborn as sns
import matplotlib.pyplot as plt
import scipy.optimize
from scipy.optimize import least_squares
from scipy.optimize import curve_fit


# In[ ]:


# Read input datafile for Monolith X
dff =pd.read_excel("dataaptamer.xlsx", sheet_name='dataaptamer');

#Sort data by concentration, and populate into new dataframes
num_columns = len(dff) //48

# Create a new DataFrame
new_dff = pd.DataFrame()
new_df=pd.DataFrame()

# Iterate over the rows in chunks of 48
for i in range(0, len(dff), 48):
    column_name = f'Column_{i // 48 + 1}'
    new_dff[column_name] = dff['ratio'].iloc[i:i+48].reset_index(drop=True)
    new_df[column_name] = dff['peptide'].iloc[i:i+48].reset_index(drop=True
    )

x=dff['time'].iloc[0:0+48]
x=np.array(x)

#Creation of dataframes for plotting dose repsonse curves
ratios= new_dff.T
concs=new_df.T
x=concs.iloc[:,0]


# In[ ]:


y1=np.array(new_dff.iloc[:,0])
y2=np.array(new_dff.iloc[:,1])
y3=np.array(new_dff.iloc[:,2])
y4=np.array(new_dff.iloc[:,3])
y5=np.array(new_dff.iloc[:,4])
y6=np.array(new_dff.iloc[:,5])
```

```python
y7=np.array(new_dff.iloc[:,6])

x=dff['time'].iloc[0:0+48]
x=np.array(x)


# In[ ]:


# Define the exponential function
def exponential(x, A, k, t0):
    return A * (1 - np.exp(-k * x)) + t0

# Combine all curves into a single array
y_combined = np.concatenate([y1, y2, y3, y4,y5,y6,y7])

# Define the global fit function
def global_fit(x, A1, A2, A3, A4,A5,A6,A7, k, t01, t02, t03, t04,t05,t06, t07):
    y1_fit = exponential(x, A1, k, t01)
    y2_fit = exponential(x, A2, k, t02)
    y3_fit = exponential(x, A3, k, t03)
    y4_fit = exponential(x, A4, k, t04)
    y5_fit = exponential(x, A5, k, t05)
    y6_fit = exponential(x, A6, k, t06)
    y7_fit = exponential(x, A7, k, t07)
    return np.concatenate([y1_fit, y2_fit, y3_fit, y4_fit,y5_fit,y6_fit, y7_fit])

# Perform the global fit
p0 = [10,10,10,10,10,10,10, 0.65, 0.9,0.9, 0.9, 0.9, 0.9, 0.9, 0.9]  # Initial guess for parameters
params, pcov = curve_fit(global_fit, x, y_combined, p0)

# Separate the optimized parameters for each curve
A_opt = params[:7]
k_opt = params[7]
t0_opt = params[8:]


# Obtain the standard errors for the optimized parameters from the diagonal elements of the covariance matrix
A_std = np.sqrt(np.diag(pcov)[:7])
k_std = np.sqrt(pcov[7, 7])
t0_std = np.sqrt(np.diag(pcov)[8:])

# Print the optimized parameters and their standard errors for each curve
for i in range(7):
    print(f'Optimized Parameters for Curve {i+1}:')
    print('A:', A_opt[i], '+/-', A_std[i])
    print('k:', k_opt, '+/-', k_std)
    print('t0:', t0_opt[i], '+/-', t0_std[i])
    print()

```

```python
# Plot the data and fitted curves
plt.figure(figsize=(8, 6))
plt.plot(x, y1, 'o',color='#440154', label='Curve 1')
plt.plot(x, exponential(x, A_opt[0], k_opt, t0_opt[0]), '#440154', label='Fit 1')
plt.plot(x, y2, 'o', color='#414487',label='Curve 2')
plt.plot(x, exponential(x, A_opt[1], k_opt, t0_opt[1]),color='#414487', label='Fit 2')
plt.plot(x, y3, 'o', color='#2a788e',label='Curve 3')
plt.plot(x, exponential(x, A_opt[2], k_opt, t0_opt[2]), color='#2a788e', label='Fit 3')
plt.plot(x, y4, 'o', color='#22a884',label='Curve 4')
plt.plot(x, exponential(x, A_opt[3], k_opt, t0_opt[3]), color='#22a884', label='Fit 4')
plt.plot(x, y5, 'o', color='#5ec962',label='Curve 5')
plt.plot(x, exponential(x, A_opt[4], k_opt, t0_opt[4]), color='#5ec962', label='Fit 5')
plt.plot(x, y6, 'o', color='#2a788e',label='Curve 6')
plt.plot(x, exponential(x, A_opt[5], k_opt, t0_opt[5]), color='#2a788e', label='Fit 6')
plt.plot(x, y7, 'o', color='#fde725',label='Curve 7')
plt.plot(x, exponential(x, A_opt[6], k_opt, t0_opt[6]), color='#fde725', label='Fit 7')
plt.legend()
plt.ylabel('ratio')
plt.xlabel('time (seconds)')
plt.title('Global Fit with Shared Parameter (k_obs)')
plt.show()

# Print the optimized parameters for each curve
for i in range(4):
    print(f'Optimized Parameters for Curve {i+1}:')
    print('A:', A_opt[i])
    print('k:', k_opt)
    print('t0:', t0_opt[i])
    print()
```

Bibliography

(1) Soto, C.; Pritzkow, S. *Nature Neuroscience 2018 21:10* **2018**, *21*, doi: 10.1038/s41593-018-0235-9, 1332–1340.

(2) *Alzheimer's Dementia* **2022**, *18*, 700–789.

(3) Iljina, M.; Dear, A. J.; Garcia, G. A.; De, S.; Tosatto, L.; Flagmeier, P.; Whiten, D. R.; Michaels, T. C. T.; Frenkel, D.; Dobson, C. M.; Knowles, T. P. J.; Klenerman, D. *ACS Nano* **2018**, *12*, doi: 10.1021/acsnano.8b03575, 10855–10866.

(4) Ittner, L. M.; Götz, J. *Nature Reviews Neuroscience* **2011**, *12*, doi :10.1038/nrn2967, 67–72.

(5) Park, S. Y.; Ferreira, A. *The Journal of neuroscience : the official journal of the Society for Neuroscience* **2005**, *25*, doi: 10.1523/JNEUROSCI.1125-05.2005, 5365–5375.

(6) Small, S. A.; Duff, K. *Neuron* **2008**, *60*, doi: 10.1016/J.NEURON.2008.11.007, 534–542.

(7) King, M. E.; Kan, H. M.; Baas, P. W.; Erisir, A.; Glabe, C. G.; Bloom, G. S. *The Journal of cell biology* **2006**, *175*, doi: 10.1083/JCB.200605187, 541–546.

(8) Tripathi, T.; Khan, H. *Biochemistry* **2020**, *59*, doi: 10.1021/acs.biochem.9b01087, 341–342.

(9) Wang, Y.; Mandelkow, E. *Nature Reviews Neuroscience* **2016**, *17*, doi: 10.1038/nrn.2015.1, 22–35.

(10) Stelzmann, R. A.; Schnitzlein, H. N.; Murtagh, F. R. *Clinical Anatomy* **1995**, *8*, doi: 10.1002/CA.980080612, 429–431.

(11) Goedert, M.; Crowther, R. A.; Spillantini, M. G. *Neuron* **1998**, *21*, doi: 10.1016/S0896-6273(00)80615-7, 955–958.

(12) Goedert, M; Jakes, R; Spillantini, M. G.; Hasegawa, M; Smith, M. J.; Crowther, R. A. *Nature* **1996**, *383*, 550–553.

(13) Hernández, F.; Avila, J. *Cellular and Molecular Life Sciences* **2007**, *64*, doi: 10.1007/S00 018-007-7220-X/METRICS, 2219–2233.

(14) Mylonas, E.; Hascher, A.; Bernadó, P.; Blackledge, M.; Mandelkow, E.; Svergun, D. I. *Biochemistry* **2008**, *47*, doi: 10.1021/bi800900d, 10345–10353.

(15) Maeda, S.; Sahara, N.; Saito, Y.; Murayama, S.; Ikai, A.; Takashima, A. *Neuroscience research* **2006**, *54*, doi: 10.1016/J.NEURES.2005.11.009, 197–201.

(16) Lövestam, S.; Koh, F. A.; van Knippenberg, B.; Kotecha, A.; Murzin, A. G.; Goedert, M.; Scheres, S. H. *eLife* **2022**, *11*, doi: 10.7554/ELIFE.76494.

(17) Wang, B.; Zhang, L.; Dai, T.; Qin, Z.; Lu, H.; Zhang, L.; Zhou, F. *Signal Transduction and Targeted Therapy* **2021**, *6*, doi: 10.1038/s41392-021-00678-1, 290.

(18) Andreadis, A.; Brown, W. M.; Kosik, K. S. *Biochemistry* **1992**, *31*, doi: 10.1021/bi0015-8a027, 10626–10633.

(19) Lee, J.; Cho, H.; Kwon, I. *Experimental Molecular Medicine* **2022**, *54*, doi: 10.1038/s12276-022-00857-2, 1412–1422.

(20) Chong, F. P.; Ng, K. Y.; Koh, R. Y.; Chye, S. M. *Cellular and Molecular Neurobiology* **2018**, *38*, doi: 10.1007/s10571-017-0574-1, 965–980.

(21) Uversky, V. N. *Current Opinion in Structural Biology* **2017**, *44*, doi: https://doi.org/10.1016/j.sbi.2016.10.015, 18–30.

(22) Lee, G; Newman, S. T.; Gard, D. L.; Band, H; Panchamoorthy, G *Journal of Cell Science* **1998**, *111*, doi: 10.1242/jcs.111.21.3167, 3167–3177.

(23) Humphrey, S. J.; James, D. E.; Mann, M. *Trends in Endocrinology Metabolism* **2015**, *26*, doi: 10.1016/J.TEM.2015.09.013, 676–687.

(24) Hanger, D. P.; Anderton, B. H.; Noble, W. *Trends in molecular medicine* **2009**, *15*, doi: 10.1016/J.MOLMED.2009.01.003, 112–119.

(25) Wang, D.; Huang, X.; Yan, L.; Zhou, L.; Yan, C.; Wu, J.; Su, Z.; Huang, Y. *The Protein Journal* **2021**, *40*, doi: 10.1007/s10930-021-10017-6, 656–668.

(26) Kametani, F.; Yoshida, M.; Matsubara, T.; Murayama, S.; Saito, Y.; Kawakami, I.; Onaya, M.; Tanaka, H.; Kakita, A.; Robinson, A. C.; Mann, D. M. A.; Hasegawa, M. *Frontiers in neuroscience* **2020**, *14*, doi: 10.3389/fnins.2020.581936, 581936.

(27) Min, S. W.; Cho, S. H.; Zhou, Y.; Schroeder, S.; Haroutunian, V.; Seeley, W. W.; Huang, E. J.; Shen, Y.; Masliah, E.; Mukherjee, C.; Meyers, D.; Cole, P. A.; Ott, M.; Gan, L. *Neuron* **2010**, *67*, doi: 10.1016/J.NEURON.2010.08.044, 953–966.

(28) Min, S. W. et al. *Nature medicine* **2015**, *21*, doi: 10.1038/NM.3951, 1154.

(29) Thomas, S. N.; Funk, K. E.; Wan, Y.; Liao, Z.; Davies, P.; Kuret, J.; Yang, A. J. *Acta neuropathologica* **2012**, *123*, doi: 10.1007/S00401-011-0893-0, 105–117.

(30) Takahashi, M.; Tsujioka, Y.; Yamada, T.; Tsuboi, Y.; Okada, H.; Yamamoto, T.; Liposits, Z. *Acta neuropathologica* **1999**, *97*, doi: 10.1007/S004010051040, 635–641.

(31) Wang, J. Z.; Grundke-Iqbal, I.; Iqbal, K. *Nature medicine* **1996**, *2*, doi: 10.1038/NM0896-871, 871–875.

(32) Martin, L.; Latypova, X.; Terro, F. *Neurochemistry International* **2011**, *58*, doi: 10.1016/J.NEUINT.2010.12.023, 458–471.

(33) Necula, M.; Kuret, J. *Journal of Biological Chemistry* **2004**, *279*, doi: 10.1074/jbc.M405527200, 49694–49703.

(34) Morishima-Kawashima, M.; Hasegawa, M.; Takio, K.; Suzuki, M.; Titani, K.; Ihara, Y. *Neuron* **1993**, *10*, doi: 10.1016/0896-6273(93)90063-W, 1151–1160.

(35) Riederer, I. M.; Schiffrin, M.; Kövari, E.; Bouras, C.; Riederer, B. M. *Brain research bulletin* **2009**, *80*, doi: 10.1016/J.BRAINRESBULL.2009.04.018, 233–241.

(36) Alquezar, C.; Arya, S.; Kao, A. W. *Frontiers in Neurology* **2021**, *11*, doi: 10.3389/FNEUR.2020.595532/BIBTEX, 1826.

(37) Bancher, C.; Grundke-Iqbal, I.; Iqbal, K.; Fried, V. A.; Smith, H. T.; Wisniewski, H. M. *Brain research* **1991**, *539*, doi: 10.1016/0006-8993(91)90681-K, 11–18.

(38) Dickey, C. A. et al. *The Journal of neuroscience : the official journal of the Society for Neuroscience* **2006**, *26*, doi: 10.1523/JNEUROSCI.0746-06.2006, 6985–6996.

(39) Petrucelli, L. et al. *Human molecular genetics* **2004**, *13*, doi: 10.1093/HMG/DDH083, 703–714.

(40) Cleveland, D. W.; Hwo, S.-Y.; Kirschner, M. W. *Journal of Molecular Biology* **1977**, *116*, doi: 10.1016/0022-2836(77)90214-5, 227–247.

(41) Barghorn, S; Mandelkow, E *Biochemistry* **2002**, *41*, doi: 10.1021/bi026469j, 14885–14896.

(42) Lee, G.; Cowan, N.; Kirschner, M. *Science* **1988**, *239*, doi: 10.1126/science.3122323, 285–288.

(43) Jeganathan, S.; von Bergen, M.; Brutlach, H.; Steinhoff, H.-J.; Mandelkow, E. *Biochemistry* **2006**, *45*, doi: 10.1021/bi0521543, 2283–2293.

(44) Mukrasch, M. D.; Bibow, S.; Korukottu, J.; Jeganathan, S.; Biernat, J.; Griesinger, C.; Mandelkow, E.; Zweckstetter, M. *PLoS biology* **2009**, *7*, doi: 0.1371/journal.pbio.100 0034, e34–e34.

(45) Mukrasch, M. D.; Markwick, P.; Biernat, J.; von Bergen, M.; Bernadó, P.; Griesinger, C.; Mandelkow, E.; Zweckstetter, M.; Blackledge, M. *Journal of the American Chemical Society* **2007**, *129*, doi: 10.1021/ja0690159, 5235–5243.

(46) Nath, A.; Sammalkorpi, M.; DeWitt, D. C.; Trexler, A. J.; Elbaum-Garfinkle, S.; O'Hern, C. S.; Rhoades, E. *Biophysical journal* **2012**, *103*, doi: 10.1016/j.bpj.2012.09.032, 1940–1949.

(47) Mroczko, B.; Groblewska, M.; Litman-Zawadzka, A. *International journal of molecular sciences* **2019**, *20*, doi: 10.3390/ijms20194661, 4661.

(48) Fichou, Y.; Al-Hilaly, Y. K.; Devred, F.; Smet-Nocca, C.; Tsvetkov, P. O.; Verelst, J.; Winderickx, J.; Geukens, N.; Vanmechelen, E.; Perrotin, A.; Serpell, L.; Hanseeuw, B. J.; Medina, M.; Buée, L.; Landrieu, I. *Acta Neuropathologica Communications* **2019**, *7*, doi: 10.1186/s40478-019-0682-x, 31.

(49) Eschmann, N. A.; Georgieva, E. R.; Ganguly, P.; Borbat, P. P.; Rappaport, M. D.; Akdogan, Y.; Freed, J. H.; Shea, J.-E.; Han, S. *Scientific Reports* **2017**, *7*, doi: 10.1038/srep44739, 44739.

(50) Ward, S. M.; Himmelstein, D. S.; Lancia, J. K.; Binder, L. I. *Biochemical Society transactions* **2012**, *40*, doi: 10.1042/BST20120134, 667–671.

(51) Lasagna-Reeves, C. A.; Castillo-Carranza, D. L.; Guerrero-Muñoz, M. J.; Jackson, G. R.; Kayed, R. *Biochemistry* **2010**, *49*, doi: 10.1021/bi1016233, 10039–10041.

(52) Andorfer, C.; Acker, C. M.; Kress, Y.; Hof, P. R.; Duff, K.; Davies, P. *The Journal of neuroscience : the official journal of the Society for Neuroscience* **2005**, *25*, doi: 10.1523/JNEUROSCI.4637-04.2005, 5446–5454.

(53) SantaCruz, K et al. *Science* **2005**, *309*, doi: 10.1126/science.1113694, 476–481.

(54) Wittmann, C. W.; Wszolek, M. F.; Shulman, J. M.; Salvaterra, P. M.; Lewis, J.; Hutton, M.; Feany, M. B. *Science* **2001**, *293*, doi: 10.1126/science.1062382, 711–714.

(55) Lasagna-Reeves, C. A.; Castillo-Carranza, D. L.; Sengupta, U.; Sarmiento, J.; Troncoso, J.; Jackson, G. R.; Kayed, R. *FASEB journal : official publication of the Federation of American Societies for Experimental Biology* **2012**, *26*, doi: 0.1096/FJ.11-199851, 1946–1959.

(56) Lasagna-Reeves, C. A.; Castillo-Carranza, D. L.; Sengupta, U.; Clos, A. L.; Jackson, G. R.; Kayed, R. *Molecular neurodegeneration* **2011**, *6*, doi: 10.1186/1750-1326-6-39, DOI: `10.1186/1750-1326-6-39`.

(57) Friedhoff, P; Bergen, M. V.; Mandelkow, E.-M; Davies, P; Mandelkow, E *Neurobiology* **1998**, *95*, 15712–15717.

(58) Congdon, E. E.; Kim, S.; Bonchak, J.; Songrug, T.; Matzavinos, A.; Kuret, J. **2008**, doi: 10.1074/jbc.M800247200.

(59) Ramachandran, G.; Udgaonkar, J. B. *Journal of Molecular Biology* **2012**, *421*, doi: 10.1016/J.JMB.2012.01.007, 296–314.

(60) Kim, D.; Lim, S.; Haque, M. M.; Ryoo, N.; Hong, H. S.; Rhim, H.; Lee, D.-E.; Chang, Y.-T.; Lee, J.-S.; Cheong, E.; Kim, D. J.; Kim, Y. K. *Scientific reports* **2015**, *5*, doi: 10.1038/srep15231, 15231.

(61) Al-Hilaly, Y. K.; Pollack, S. J.; Vadukul, D. M.; Citossi, F.; Rickard, J. E.; Simpson, M.; Storey, J. M. D.; Harrington, C. R.; Wischik, C. M.; Serpell, L. C. *Journal of Molecular Biology* **2017**, *429*, doi: https://doi.org/10.1016/j.jmb.2017.09.007, 3650–3665.

(62) Sahara, N.; Maeda, S.; Murayama, M.; Suzuki, T.; Dohmae, N.; Yen, S.-H.; Takashima, A. *European Journal of Neuroscience* **2007**, *25*, doi: https://doi.org/10.1111/j.1460-9568.2007.05555.x, 3020–3029.

(63) Rosenberg, K. J.; Ross, J. L.; Feinstein, H. E.; Feinstein, S. C.; Israelachvili, J. *Proceedings of the National Academy of Sciences of the United States of America* **2008**, *105*, doi: 10.1073/pnas.0802036105, 7445–7450.

(64) Feinstein, H. E.; Benbow, S. J.; LaPointe, N. E.; Patel, N.; Ramachandran, S.; Do, T. D.; Gaylord, M. R.; Huskey, N. E.; Dressler, N.; Korff, M.; Quon, B.; Cantrell, K. L.; Bowers, M. T.; Lal, R.; Feinstein, S. C. *Journal of Neurochemistry* **2016**, *137*, doi: https://doi.org/10.1111/jnc.13604, 939–954.

(65) Kuret, J.; Chirita, C. N.; Congdon, E. E.; Kannanayakal, T.; Li, G.; Necula, M.; Yin, H.; Zhong, Q. *Biochimica et Biophysica Acta (BBA) - Molecular Basis of Disease* **2005**, *1739*, 167–178.

(66) Fitzpatrick, A. W. P.; Falcon, B.; He, S.; Murzin, A. G.; Murshudov, G.; Garringer, H. J.; Crowther, R. A.; Ghetti, B.; Goedert, M.; Scheres, S. H. W. *Nature* **2017**, *547*, 185–190.

(67) Yang, Y. et al. *Science (New York, N.Y.)* **2022**, *375*, 167–172.

(68) Crowther, R. A. *Proceedings of the National Academy of Sciences* **1991**, *88*, 2288–2292.

(69) Wischik, C. M.; Novak, M; Edwards, P. C.; Klug, A; Tichelaar, W; Crowther, R. A. *Proceedings of the National Academy of Sciences* **1988**, *85*, 4884–4888.

(70) Limorenko, G.; Lashuel, H. A. *Chem. Soc. Rev.* **2022**, *51*, 513–565.

(71) Fichou, Y.; Lin, Y.; Rauch, J. N.; Vigers, M.; Zeng, Z.; Srivastava, M.; Keller, T. J.; Freed, J. H.; Kosik, K. S.; Han, S. *Proceedings of the National Academy of Sciences of the United States of America* **2018**, *115*, 13234–13239.

(72) Zhang, W.; Falcon, B.; Murzin, A. G.; Fan, J.; Crowther, R. A.; Goedert, M.; Scheres, S. H. W. *eLife* **2019**, *8*, ed. by Grigorieff, N.; Wolberger, C.; Grigorieff, N.; Stahlberg, H.; Fändrich, M., e43584.

(73) Vaquer-Alicea, J.; Diamond, M. I.; Joachimiak, L. A. *Acta Neuropathologica* **2021**, *142*, 57–71.

(74) Rai, S. K.; Savastano, A.; Singh, P.; Mukhopadhyay, S.; Zweckstetter, M. *Protein Science* **2021**, *30*, doi: https://doi.org/10.1002/pro.4093, 1294–1314.

(75) Lin, Y.; Fichou, Y.; Longhini, A. P.; Llanes, L. C.; Yin, P.; Bazan, G. C.; Kosik, K. S.; Han, S. *Journal of Molecular Biology* **2021**, *433*, doi: 10.1016/J.JMB.2020.166731, 166731.

(76) Boyko, S.; Qi, X.; Chen, T.-H.; Surewicz, K.; Surewicz, W. K. *Journal of Biological Chemistry* **2019**, *294*, doi: 10.1074/jbc.AC119.009198, 11054–11059.

(77) Wen, J.; Hong, L.; Krainer, G.; Yao, Q.-Q.; Knowles, T. P. J.; Wu, S.; Perrett, S. *Journal of the American Chemical Society* **2021**, *143*, doi: 10.1021/jacs.1c03078, 13056–13064.

(78) Zhang, X.; Lin, Y.; Eschmann, N. A.; Zhou, H.; Rauch, J. N.; Hernandez, I.; Guzman, E.; Kosik, K. S.; Han, S. *PLoS biology* **2017**, *15*, doi: 10.1371/journal.pbio.2002183, e2002183–e2002183.

(79) Lin, Y.; Fichou, Y.; Zeng, Z.; Hu, N. Y.; Han, S. *ACS Chemical Neuroscience* **2020**, *11*, doi: 10.1021/acschemneuro.9b00627, 615–627.

(80) A., S.; Adrian, F. E. V.-C.; Leavitt, *Characterization of Protein-Protein Interactions by Isothermal Titration Calorimetry*; Fu, H., Ed., doi: 10.1385/1-59259-762-9:035; Humana Press: 2004, pp 35–54.

(81) Doyle, M. L. *Current Opinion in Biotechnology* **1997**, *8*, doi: https://doi.org/10.1016/S0958-1669(97)80154-1, 31–35.

(82) Kumar, V.; Sami, N.; Kashav, T.; Islam, A.; Ahmad, F.; Hassan, M. I. *European Journal of Medicinal Chemistry* **2016**, *124*, doi: 10.1016/j.ejmech.2016.07.054, 1105–1120.

(83) Kim, A. C.; Lim, S.; Kim, Y. K. *International Journal of Molecular Sciences* **2018**, *19*, doi: 10.3390/ijms19010128, 1–15.

(84) Li, X.; Du, X.; Ni, J. *International Journal of Molecular Sciences* **2019**, *20*, doi: 10.3390/ijms20030487, 1–16.

(85) Douzi, B., *Protein–Protein Interactions: Surface Plasmon Resonance*; Laure, E. J., Cascales, Eds., doi: 10.1007/978-1-4939-7033-$9_2$1; Springer New York: 2017, pp 257–275.

(86) Vagrys, D.; Davidson, J.; Chen, I.; Hubbard, R. E.; Davis, B. *International journal of molecular sciences* **2020**, *21*, doi: 10.3390/ijms21155257, 5257.

(87) Dunning, C. J.; McGauran, G.; Willén, K.; Gouras, G. K.; O'Connell, D. J.; Linse, S. *ACS Chemical Neuroscience* **2016**, *7*, doi: 10.1021/acschemneuro.5b00262, 161–170.

(88) Paynter, S.; Russell, D. A. *Analytical Biochemistry* **2002**, *309*, doi: https://doi.org/10.1016/S0003-2697(02)00255-5, 85–95.

(89) Gestwicki, J. E.; Hsieh, H. V.; Pitner, J. B. *Analytical Chemistry* **2001**, *73*, doi: 10.1021/ac0105888, 5732–5737.

(90) Jerabek-Willemsen, M.; André, T.; Wanner, R.; Roth, H. M.; Duhr, S.; Baaske, P.; Breitsprecher, D. *Journal of Molecular Structure* **2014**, *1077*, 101–113.

(91) Wolff, M.; Mittag, J. J.; Herling, T. W.; Genst, E. D.; Dobson, C. M.; Knowles, T. P. J.; Braun, D.; Buell, A. K. *Scientific Reports* **2016**, *6*, doi: 10.1038/srep22829, 22829.

(92) Kiss, R.; Csizmadia, G.; Solti, K.; Keresztes, A.; Zhu, M.; Pickhardt, M.; Mandelkow, E.; Tóth, G. *ACS Chemical Neuroscience* **2018**, *9*, doi: 10.1021/acschemneuro.8b00182, 2997–3006.

(93) Fisher, E.; Zhao, Y.; Richardson, R.; Janik, M.; Buell, A. K.; Aigbirhio, F. I.; Tóth, G. *ACS Chemical Neuroscience* **2017**, *8*, doi: 10.1021/acschemneuro.7b00228, 2088–2095.

(94) Gabr, M. T.; Barbault, F. *Chem. Commun.* **2020**, *56*, doi: 10.1039/D0CC04249H, 9695–9698.

(95) Guyot, A.-C. et al. *Scientific Reports* **2020**, *10*, doi: 10.1038/s41598-020-57560-3, 1143.

(96) Malmos, K. G.; Blancas-Mejia, L. M.; Weber, B.; Buchner, J.; Ramirez-Alvarado, M.; Naiki, H.; Otzen, D. *http://dx.doi.org/10.1080/13506129.2017.1304905* **2017**, *24*, 1–16.

(97) Almeida, Z. L.; Brito, R. M. M. *Molecules* **2020**, *25*, doi: 10.3390/molecules25051195.

(98) Younan, N. D.; Viles, J. H. *Biochemistry* **2015**, *54*, doi: 10.1021/acs.biochem.5b00309, 4297–4306.

(99) Bulic, B.; Pickhardt, M.; Mandelkow, E.-M.; Mandelkow, E. *Neuropharmacology* **2010**, *59*, https://doi.org/10.1016/j.neuropharm.2010.01.016, 276–289.

(100) Von Bergen, M; Friedhoff, P; Biernat, J; Heberle, J; Mandelkow, E. M.; Mandelkow, E *Proceedings of the National Academy of Sciences of the United States of America* **2000**, *97*, doi: 10.1073/pnas.97.10.5129, 5129–5134.

(101) Alonso, A; Zaidi, T; Novak, M; Grundke-Iqbal, I; Iqbal, K *Proceedings of the National Academy of Sciences of the United States of America* **2001**, *98*, doi: 10.1073/p-nas.121119298, 6923–6928.

(102) Rolinski, O. J.; Amaro, M.; Birch, D. J. S. *Biosensors and Bioelectronics* **2010**, *25*, doi: https://doi.org/10.1016/j.bios.2010.03.005, 2249–2252.

(103) Chan, F. T. S.; Pinotsi, D.; Gabriele, S; Schierle, K.; Kaminski, C. F., *Chapter 13 - Structure-Specific Intrinsic Fluorescence of Protein Amyloids Used to Study their Kinetics of Aggregation*; Uversky, V. N., Lyubchenko, Y. L., Eds., doi: https://doi.org/10.1016/B978-0-12-394431-3.00013-4; Academic Press: 2014, pp 147–155.

(104) Dusa, A.; Kaylor, J.; Edridge, S.; Bodner, N.; Hong, D.-P.; Fink, A. L. *Biochemistry* **2006**, *45*, doi: 10.1021/bi051426z, 2752–2760.

(105) Van Rooijen, B. D.; van Leijenhorst-Groener, K. A.; Claessens, M.; Subramaniam, V *Journal of Molecular Biology* **2009**, *394*, doi: https://doi.org/10.1016/j.jmb.2009.10.021, 826–833.

(106) Amaro, M.; Birch, D. J. S.; Rolinski, O. J. *Phys. Chem. Chem. Phys.* **2011**, *13*, doi: 10.1039/C0CP02652B, 6434–6441.

(107) MAGNUS, J. H.; STENSTAD, T; KOLSET, S. O.; HUSBY, G *Scandinavian Journal of Immunology* **1991**, *34*, doi: https://doi.org/10.1111/j.1365-3083.1991.tb01521.x, 63–69.

(108) DeWitt, D. A.; Silver, J.; Canning, D. R.; Perry, G. *Experimental Neurology* **1993**, *121*, doi: https://doi.org/10.1006/exnr.1993.1081, 149–152.

(109) Ramachandran, G.; Udgaonkar, J. B. *The Journal of biological chemistry* **2011**, *286*, 38948–38959.

(110) Elbaum-Garfinkle, S.; Rhoades, E. *Journal of the American Chemical Society* **2012**, *134*, 16607–16613.

(111) Chirita, C. N.; Necula, M.; Kuret, J. *Journal of Biological Chemistry* **2003**, *278*, doi: 10.1074/jbc.M301663200, 25644–25650.

(112) Shammas, S. L.; Garcia, G. A.; Kumar, S.; Kjaergaard, M.; Horrocks, M. H.; Shivji, N.; Mandelkow, E.; Knowles, T. P. J.; Mandelkow, E.; Klenerman, D. *Nature Communications* **2015**, *6*, doi: 10.1038/ncomms8025, 7025.

(113) Goedert, M; Wischik, C. M.; Crowther, R. A.; Walker, J. E.; Klug, A *Proceedings of the National Academy of Sciences* **1988**, *85*, doi: 10.1073/pnas.85.11.4051, 4051–4055.

(114) Carlson, S. W.; Branden, M.; Voss, K.; Sun, Q.; Rankin, C. A.; Gamblin, T. C. *Biochemistry* **2007**, *46*, doi: 10.1021/bi700403a, 8838–8849.

(115) Kepp, K. P. *Chemical Reviews* **2012**, *112*, doi: 10.1021/cr300009x, 5193–5239.

(116) Maher, P. *Free Radical Biology and Medicine* **2018**, *115*, doi: https://doi.org/10.1016/j.freeradbiomed.2017.11.015, 92–104.

(117) Acevedo, K.; Masaldan, S.; Opazo, C. M.; Bush, A. I. *JBIC Journal of Biological Inorganic Chemistry* **2019**, *24*, doi: 10.1007/s00775-019-01731-9, 1141–1157.

(118) Lin, Y.; McCarty, J.; Rauch, J. N.; Delaney, K. T.; Kosik, K. S.; Fredrickson, G. H.; Shea, J.-E.; Han, S. *eLife* **2019**, *8*, ed. by Shan, Y.; Barkai, N.; Castaneda, C., doi: 10.7554/eLife.42571, e42571.

(119) Liu, W.; Samanta, A.; Deng, J.; Akintayo, C. O.; Walther, A. *Angewandte Chemie International Edition* **2022**, *61*, doi: https://doi.org/10.1002/anie.202208951, e202208951.

(120) DeGrado, T. R.; Kemp, B. J.; Pandey, M. K.; Jiang, H.; Gunderson, T. M.; Linscheid, L. R.; Woodwick, A. R.; McConnell, D. M.; Fletcher, J. G.; Johnson, G. B.; Petersen, R. C.; Knopman, D. S.; Lowe, V. J. *Molecular Imaging* **2016**, *15*, doi: 10.1177/1536012116673793, 1536012116673793.

(121) Bader, B.; Nübling, G.; Mehle, A.; Nobile, S.; Kretzschmar, H.; Giese, A. *Biochemical and Biophysical Research Communications* **2011**, *411*, 190–196.

(122) Perl, D. P.; Brody, A. R. *Science* **1980**, *208*, doi: 10.1126/science.7367858, 297–299.

(123) Huang, Y.; Wu, Z.; Cao, Y.; Lang, M.; Lu, B.; Zhou, B. *Cell Reports* **2014**, *8*, doi: 10.1016/j.celrep.2014.06.047, 831–842.

(124) Mo, Z. Y.; Zhu, Y. Z.; Zhu, H. L.; Fan, J. B.; Chen, J.; Liang, Y. *Journal of Biological Chemistry* **2009**, *284*, doi: 10.1074/jbc.M109.058883, 34648–34657.

(125) Moreira, G. G.; Cristóvão, J. S.; Torres, V. M.; Carapeto, A. P.; Rodrigues, M. S.; Landrieu, I.; Cordeiro, C.; Gomes, C. M. *International Journal of Molecular Sciences* **2019**, *20*, doi: 10.3390/ijms20235979, 1–13.

(126) Hu, J. Y.; Zhang, D. L.; Liu, X. L.; Li, X. S.; Cheng, X. Q.; Chen, J.; Du, H. N.; Liang, Y. *Biochimica et Biophysica Acta - Molecular Basis of Disease* **2017**, *1863*, doi: 10.1016/j.bbadis.2016.11.022, 414–427.

(127) Pickhardt, M.; Neumann, T.; Schwizer, D.; Callaway, K.; Vendruscolo, M.; Schenk, D.; George-Hyslop, S. P.; Mandelkow, E. M.; Dobson, C. M.; McConlogue, L.; Mandelkow, E.; Tóth, G. *Current Alzheimer research* **2015**, *12*, 814.

(128) Taniguchi, S.; Suzuki, N.; Masuda, M.; ichi Hisanaga, S.; Iwatsubo, T.; Goedert, M.; Hasegawa, M. *Journal of Biological Chemistry* **2005**, *280*, doi: 10.1074/jbc. M408714200, 7614–7623.

(129) Akoury, E.; Pickhardt, M.; Gajda, M.; Biernat, J.; Mandelkow, E.; Zweckstetter, M. *Angewandte Chemie (International ed. in English)* **2013**, *52*, 3511–3515.

(130) Jadhav, S.; Avila, J.; Schöll, M.; Kovacs, G. G.; Kövari, E.; Skrabana, R.; Evans, L. D.; Kontsekova, E.; Malawska, B.; de Silva, R.; Buee, L.; Zilka, N. *Acta Neuropathologica Communications 2019 7:1* **2019**, *7*, 1–31.

(131) Maqbool, M.; Mobashir, M.; Hoda, N. *European Journal of Medicinal Chemistry* **2016**, *107*, 63–81.

(132) Hampel, H.; Lista, S.; Mango, D.; Nisticò, R.; Perry, G.; Avila, J.; Hernandez, F.; Geerts, H.; Vergallo, A. *Journal of Alzheimer's Disease* **2019**, *69*, 615–629.

(133) Wischik, C. M.; Edwards, P. C.; Lai, R. Y.; Roth, M.; Harrington, C. R. *Proceedings of the National Academy of Sciences of the United States of America* **1996**, *93*, 11213–11218.

(134) Hamaguchi, T.; Ono, K.; Yamada, M. *CNS Neuroscience Therapeutics* **2010**, *16*, doi: https://doi.org/10.1111/j.1755-5949.2010.00147.x, 285–297.

(135) Congdon, E. E.; Sigurdsson, E. M. *Nature Reviews Neurology* **2018**, *14*, doi: 10.1038/s41582-018-0013-z, 399–415.

(136) Belkacemi, A.; Doggui, S.; Dao, L.; Ramassamy, C. *Expert Reviews in Molecular Medicine* **2011**, *13*, doi: 10.1017/S1462399411002055, e34.

(137) Tang, M.; Taghibiglou, C. *Journal of Alzheimer's Disease* **2017**, *58*, doi: 10.3233/JAD-170188, 1003–1016.

(138) Okuda, M.; Hijikuro, I.; Fujita, Y.; Teruya, T.; Kawakami, H.; Takahashi, T.; Sugimoto, H. *Bioorganic Medicinal Chemistry Letters* **2016**, *26*, 5024–5028.

(139) Sonawane, S. K.; Chidambaram, H.; Boral, D.; Gorantla, N. V.; Balmik, A. A.; Dangi, A.; Ramasamy, S.; Marelli, U. K.; Chinnathambi, S. *Scientific Reports* **2020**, *10*, doi: 10.1038/s41598-020-69429-6, 12579.

(140) Wobst, H. J.; Sharma, A.; Diamond, M. I.; Wanker, E. E.; Bieschke, J. *FEBS Letters* **2015**, *589*, doi: https://doi.org/10.1016/j.febslet.2014.11.026, 77–83.

(141) Cornejo, A.; Sandoval, F. A.; Caballero, L.; Machuca, L.; Muñoz, P.; Caballero, J.; Perry, G.; Ardiles, A.; Areche, C.; Melo, F. *Journal of Enzyme Inhibition and Medicinal Chemistry* **2017**, *32*, doi: 10.1080/14756366.2017.1347783, 945–953.

(142) Crowe, A.; James, M. J.; Virginia, M. Y.; Smith, A. B.; Trojanowski, J. Q.; Ballatore, C.; Brunden, K. R. *The Journal of biological chemistry* **2013**, *288*, 11024–11037.

(143) Ballatore, C.; Brunden, K. R.; Piscitelli, F.; James, M. J.; Crowe, A.; Yao, Y.; Hyde, E.; Trojanowski, J. Q.; Lee, V. M.-Y.; Smith, A. B. I. I. I. *Journal of Medicinal Chemistry* **2010**, *53*, doi: 10.1021/jm100138f, 3739–3747.

(144) Yang, G. J.; Liu, H.; Ma, D. L.; Leung, C. H. *JBIC Journal of Biological Inorganic Chemistry 2019 24:8* **2019**, *24*, 1159–1170.

(145) Chaudhari, V.; Bagwe-Parab, S.; Harpal, Buttar, S; Gupta, S.; Vora, A.; Kaur, G. *Neurotoxicity Research 2023* **2023**, *1*, 1–18.

(146) Rogers, J. T. et al. *Journal of Biological Chemistry* **2002**, *277*, 45518–45528.

(147) Ayton, S.; Bush, A. I. *The Lancet Neurology* **2019**, *18*, 616–617.

(148) Lei, P.; Ayton, S.; Bush, A. I. *Journal of Biological Chemistry* **2021**, *296*, doi: 10.1074/JBC.REV120.008207.

(149) Ghisaidoobe, A. B. T.; Chung, S. J. *International Journal of Molecular Sciences* **2014**, *15*, 22518–22538.

(150) Langer, A.; Lüdecke, A.; Bartoschik, T.; Cehlar, O.; Duhr, S.; Baaske, P.; Streicher, W. *ASSAY and Drug Development Technologies* **2022**, *20*, doi: 10.1089/adt.2021.133, 83–94.

(151) Expasy - ProtParam tool, url=https://web.expasy.org/protparam/.

(152) Hermanson, G. T., *Bioconjugate Techniques*; Elsevier Science: 2010.

(153) Bradski, G. *Dr. Dobb's Journal of Software Tools* **2000**.

(154) Hurst, S. J.; Lytton-Jean, A. K. R.; Mirkin, C. A. *Analytical Chemistry* **2006**, *78*, doi: 10.1021/ac0613582, 8313–8318.

(155) Li, J.; Zhu, B.; Zhu, Z.; Zhang, Y.; Yao, X.; Tu, S.; Liu, R.; Jia, S.; Yang, C. J. *Langmuir* **2015**, *31*, doi: 10.1021/acs.langmuir.5b01680, 7869–7876.

(156) Bro, R.; Smilde, A. K. *Anal. Methods* **2014**, *6*, doi: 10.1039/C3AY41907J, 2812–2831.

(157) Cleveland, W. S. *Journal of the American Statistical Association* **1979**, *74*, 829–836.

(158) Jolliffe, I. Principal Component Analysis, Major Reference Works, 2014.

(159) Jolliffe, I. T.; Cadima, J. *Philosophical Transactions of the Royal Society A: Mathematical, Physical and Engineering Sciences* **2016**, *374*, doi: 10.1098/rsta.2015.0202, 20150202.

(160) Pedregosa, F. et al. *Journal of Machine Learning Research* **2011**, *12*, 2825–2830.

(161) Lever, J.; Krzywinski, M.; Altman, N. *Nature Methods* **2017**, *14*, doi: 10.1038/nmeth.4346, 641–642.

(162) Adams, M. J., *Chemometrics in analytical spectroscopy*; 8; Royal Society of Chemistry: 2004.

(163) Kitao, A. *J* **2022**, *5*, doi: 10.3390/j5020021, 298–317.

(164) Gower, J. C. *Psychometrika* **1975**, *40*, 33–51.

(165) Fontela, Y. C.; Kadavath, H.; Biernat, J.; Riedel, D.; Mandelkow, E.; Zweckstetter, M. *Nature Communications* **2017**, *8*, doi: 10.1038/s41467-017-02230-8, 1981.

(166) Qi, H.; Cantrelle, F.-X.; Benhelli-Mokrani, H.; Smet-Nocca, C.; Buée, L.; Lippens, G.; Bonnefoy, E.; Galas, M.-C.; Landrieu, I. *Biochemistry* **2015**, *54*, doi: 10.1021/bi501 4613, 1525–1533.

(167) Guo, T.; Noble, W.; Hanger, D. P. *Acta Neuropathologica* **2017**, *133*, doi: 10.1007/s00401-017-1707-9, 665–704.

(168) Goedert, M.; Spillantini, M. G. Ordered Assembly of Tau Protein and Neurodegeneration, ed. by Takashima, A.; Wolozin, B.; Buee, L., 2019.

(169) Ukmar-Godec, T.; Wegmann, S.; Zweckstetter, M. *Seminars in Cell Developmental Biology* **2020**, *99*, SI: Protein-protein interactions in health and disease, 202–214.

(170) Brangwynne, C.; Eckmann, C.; Courson, D. S.; Rybarska, A.; Hoege, C.; Gharakhani, J.; Jülicher, F.; Hyman, A. A. *Science* **2009**, *324*, doi: 10.1126/science. 1172046, 1729–1732.

(171) Banani, S. F.; Lee, H. O.; Hyman, A. A.; Rosen, M. K. *Nature reviews. Molecular cell biology* **2017**, *18*, doi: 10.1038/nrm.2017.7, 285–298.

(172) Altmeyer, M.; Neelsen, K. J.; Teloni, F.; Pozdnyakova, I.; Pellegrino, S.; Grøfte, M.; Rask, M.-B. D.; Streicher, W.; Jungmichel, S.; Nielsen, M. L.; Lukas, J. *Nature Communications* **2015**, *6*, doi: 10.1038/ncomms9088, 8088.

(173) Patel, A. et al. *Cell* **2015**, *162*, doi: 10.1016/j.cell.2015.07.047, 1066–1077.

(174) Tatomer, D. C.; Terzo, E.; Curry, K. P.; Salzler, H.; Sabath, I.; Zapotoczny, G.; McKay, D. J.; Dominski, Z.; Marzluff, W. F.; Duronio, R. J. *Journal of Cell Biology* **2016**, *213*, doi: 10.1083/jcb.201504043, 557–570.

(175) Good, M. C.; Zalatan, J. G.; Lim, W. A. *Science* **2011**, *332*, doi: 10.1126/science. 1198701, 680–686.

(176) Ambadipudi, S.; Biernat, J.; Riedel, D.; Mandelkow, E.; Zweckstetter, M. *Nature Communications* **2017**, *8*, doi: 10.1038/s41467-017-00480-0, 275.

(177) Nedelsky, N. B.; Taylor, J. P. *Nature Reviews Neurology* **2019**, *15*, doi: 10.1038/s41582-019-0157-5, 272–286.

(178) Vacic, V.; Markwick, P. R. L.; Oldfield, C. J.; Zhao, X.; Haynes, C.; Uversky, V. N.; Iakoucheva, L. M. *PLOS Computational Biology* **2012**, *8*, e1002709–.

(179) Uversky, V. N.; Davé, V.; Iakoucheva, L. M.; Malaney, P.; Metallo, S. J.; Pathak, R. R.; Joerger, A. C. *Chemical Reviews* **2014**, *114*, doi: 10.1021/cr400713r, 6844–6879.

(180) Thandapani, P.; O'Connor, T. R.; Bailey, T.; Richard, S. *Molecular Cell* **2013**, *50*, doi: 10.1016/j.molcel.2013.05.021, 613–623.

(181) Dignon, G. L.; Best, R. B.; Mittal, J. *Annual Review of Physical Chemistry* **2020**, *71*, doi: 10.1146/annurev-physchem-071819-113553, 53–75.

(182) Gomes, E.; Shorter, J. *Journal of Biological Chemistry* **2019**, *294*, 10.1074/jbc.TM118.001192, 7115–7127.

(183) Ukmar-Godec, T.; Hutten, S.; Grieshop, M. P.; Rezaei-Ghaleh, N.; Cima-Omori, M.-S. *Nature Communications* **2019**, *10*, doi: 10.1038/s41467-019-10792-y, 2909.

(184) Ambadipudi, S.; Reddy, J. G.; Biernat, J.; Mandelkow, E.; Zweckstetter, M. *Chem. Sci.* **2019**, *10*, doi: 10.1039/C9SC00531E, 6503–6507.

(185) Holehouse, A. S.; Das, R. K.; Ahad, J. N.; Richardson, M. O. G.; Pappu, R. V. *Biophysical Journal* **2017**, *112*, doi: 10.1016/j.bpj.2016.11.3200, 16–21.

(186) Hofmeister, F. *Archiv für experimentelle Pathologie und Pharmakologie* **1888**, *24*, doi: 10.1007/BF01918191, 247–260.

(187) Wegmann, S. et al. *The EMBO Journal* **2018**, *37*, soi: https://doi.org/10.15252, e98049.

(188) Majumdar, A.; Dogra, P.; Maity, S.; Mukhopadhyay, S. *The Journal of Physical Chemistry Letters* **2019**, *10*, doi: 10.1021/acs.jpclett.9b01731, 3929–3936.

(189) Najafi, S.; Lin, Y.; Longhini, A. P.; Zhang, X.; Delaney, K. T.; Kosik, K. S.; Fredrickson, G. H.; Shea, J.-E.; Han, S. *Protein Science* **2021**, *30*, doi: https://doi.org/10.1002/pro.4101, 1393–1407.

(190) Dong, X.; Bera, S.; Qiao, Q.; Tang, Y.; Lao, Z.; Luo, Y.; Gazit, E.; Wei, G. *The Journal of Physical Chemistry Letters* **2021**, *12*, doi: 10.1021/acs.jpclett.1c00208, 2576–2586.

(191) Kanaan, N. M.; Hamel, C.; Grabinski, T.; Combs, B. *Nature Communications* **2020**, *11*, doi: 10.1038/s41467-020-16580-3, 2809.

(192) Halfmann, R. *Current opinion in structural biology* **2016**, *38*, doi: 10.1016/j.sbi.2016.05.002, 18—25.

(193) Tejedor, A. R.; Sanchez-Burgos, I.; Estevez-Espinosa, M.; Garaizar, A.; Guevara, R. C.; Ramirez, J.; Espinosa, J. R. *Nature Communications* **2022**, *13*, doi: 10.1038/s41467-022-32874-0, 5717.

(194) Wei, M.-T.; Elbaum-Garfinkle, S.; Holehouse, A. S.; Chen, C. C.-H.; Feric, M.; Arnold, C. B.; Priestley, R. D.; Pappu, R. V.; Brangwynne, C. P. *Nature Chemistry* **2017**, *9*, doi: 10.1038/nchem.2803, 1118–1125.

(195) Hernández-Vega, A.; Braun, M.; Scharrel, L.; Jahnel, M.; Wegmann, S.; Hyman, B. T.; Alberti, S.; Diez, S.; Hyman, A. A. *Cell Reports* **2017**, *20*, doi: https://doi.org/10.1016/j.celrep.2017.08.042, 2304–2312.

(196) Kroschwald, S.; Maharana, S.; Simon, A. *Matters* **2017**, *3*, doi: 10.19185/matters.201702000010, e201702000010.

(197) Chen, J.; Ma, W.; Yu, J.; Wang, X.; Qian, H.; Li, P.; Ye, H.; Han, Y.; Su, Z.; Gao, M.; Huang, Y. *Journal of Agricultural and Food Chemistry* **2023**, *71*, doi: 10.1021/acs.jafc.2c07799, 1982–1993.

(198) Seidler, P. M.; Murray, K. A.; Boyer, D. R.; Ge, P.; Sawaya, M. R.; Hu, C. J.; Cheng, X.; Abskharon, R.; Pan, H.; DeTure, M. A.; Williams, C. K.; Dickson, D. W.; Vinters, H. V.; Eisenberg, D. S. *Nature Communications* **2022**, *13*, doi: 10.1038/s41467-022-32951-4, 5451.

(199) Pradhan, A.; Mishra, S.; Surolia, A.; Panda, D. *ACS Chemical Neuroscience* **2021**, *12*, doi: 10.1021/acschemneuro.1c00098, 1989–2002.

(200) Ellis, M. J.; Lekka, C.; Tulmin, H.; O'Brien, D. P.; Dhayal, S.; Zeissler, M.-L.; Knudsen, J. G.; Kessler, B. M.; Morgan, N. G.; Todd, J. A.; Richardson, S. J.; Stefana, M. I. *bioRxiv* **2023**, doi: 10.1101/2023.04.13.536711, 2023.04.13.536711.

(201) Robertson, D. L.; Joyce, G. F. *Nature* **1990**, *344*, doi: 10.1038/344467a0, 467–468.

(202) Ellington, A. D.; Szostak, J. W. *Nature* **1992**, *355*, doi: 10.1038/355850a0, 850–852.

(203) Murakami, K.; Izuo, N.; Bitan, G. *Journal of Biological Chemistry* **2022**, *298*, doi: https://doi.org/10.1016/j.jbc.2021.101478, 101478.

(204) Iliuk, A. B.; Hu, L.; Tao, W. A. *Analytical Chemistry* **2011**, *83*, doi: 10.1021/ac201057w, 4440–4452.

(205) Röthlisberger, P.; Gasse, C.; Hollenstein, M. *International Journal of Molecular Sciences* **2017**, *18*, doi: 10.3390/ijms18112430, DOI: `10.3390/ijms18112430`.

(206) Ziu, I.; Laryea, E. T.; Alashkar, F.; Wu, C. G.; Martic, S. *Analytical and Bioanalytical Chemistry* **2020**, *412*, doi: 10.1007/S00216-019-02350-8/TABLES/1, 1193–1201.

(207) Kim, J. H.; Kim, E.; Choi, W. H.; Lee, J.; Lee, J. H.; Lee, H.; Kim, D.-E.; Suh, Y. H.; Lee, M. J. *Molecular Pharmaceutics* **2016**, *13*, doi: 10.1021/acs.molpharmaceut.6b00165, 2039–2048.

(208) Teng, I.-T.; Li, X.; Yadikar, H. A.; Yang, Z.; Li, L.; Lyu, Y.; Pan, X.; Wang, K. K.; Tan, W. *Journal of the American Chemical Society* **2018**, *140*, doi: 10.1021/jacs.8b08645, 14314–14323.

(209) Lisi, S.; Fiore, E.; Scarano, S.; Pascale, E.; Boehman, Y.; Ducongé, F.; Chierici, S.; Minunni, M.; Peyrin, E.; Ravelet, C. *Analytica Chimica Acta* **2018**, *1038*, doi: https://doi.org/10.1016/j.aca.2018.07.029, 173–181.

(210) Krylova, S. M.; Musheev, M.; Nutiu, R.; Li, Y.; Lee, G.; Krylov, S. N. *FEBS Letters* **2005**, *579*, doi: https://doi.org/10.1016/j.febslet.2005.01.032, 1371–1375.

(211) Tao, D.; Shui, B.; Gu, Y.; Cheng, J.; Zhang, W.; Jaffrezic-Renault, N.; Song, S.; Guo, Z. *Biosensors* **2019**, *9*, doi: 10.3390/bios9030084.

(212) Hun, X.; Kong, X. *Journal of Pharmaceutical and Biomedical Analysis* **2021**, *192*, doi: https://doi.org/10.1016/j.jpba.2020.113666, 113666.

(213) Zadeh, J. N.; Steenberg, C. D.; Bois, J. S.; Wolfe, B. R.; Pierce, M. B.; Khan, A. R.; Dirks, R. M.; Pierce, N. A. *Journal of Computational Chemistry* **2011**, *32*, doi: https://doi.org/10.1002/jcc.21596, 170–173.

(214) Oakley, S. S.; Maina, M. B.; Marshall, K. E.; Al-Hilaly, Y. K.; Harrington, C. R.; Wischik, C. M.; Serpell, L. C. *Frontiers in Neurology* **2020**, *11*, doi: 10.3389/fneur.2020.590754, DOI: `10.3389/fneur.2020.590754`.

(215) Zilka, N.; Kovacech, B.; Barath, P.; Kontsekova, E.; Novák, M. *Biochemical Society Transactions* **2012**, *40*, doi: 10.1042/BST20120015, 681–686.

(216) Al-Hilaly, Y. K.; Pollack, S. J.; Rickard, J. E.; Simpson, M.; Raulin, A.-C.; Baddeley, T.; Schellenberger, P.; Storey, J. M. D.; Harrington, C. R.; Wischik, C. M.; Serpell, L. C. *Journal of Molecular Biology* **2018**, *430*, doi: https://doi.org/10.1016/j.jmb.2018.08.010, 4119–4131.

(217) Crowe, A. et al. *Biochemistry* **2009**, *48*, doi: 10.1021/bi9006435, 7732–7745.

(218) Sibille, N.; Sillen, A.; Leroy, A.; Wieruszeski, J.-M.; Mulloy, B.; Landrieu, I.; Lippens, G. *Biochemistry* **2006**, *45*, doi: 10.1021/bi060964o, 12560–12572.

(219) Von Bergen, M.; Barghorn, S.; Müller, S. A.; Pickhardt, M.; Biernat, J.; Mandelkow, E.-M.; Davies, P.; Aebi, U.; Mandelkow, E. *Biochemistry* **2006**, *45*, doi: 10.1021/bi052530j, 6446–6457.

(220) Spillantini, M. G.; Tolnay, M; Love, S; Goedert, M *Acta Neuropathologica* **1999**, *97*, 585–594.

(221) Rane, J. S.; Bhaumik, P.; Panda, D. *Journal of Alzheimer's Disease* **2017**, *60*, doi: 10.3233/JAD-170351, 999–1014.

(222) Ma, Q.-L.; Zuo, X.; Yang, F.; Ubeda, O. J.; Gant, D. J.; Alaverdyan, M.; Teng, E.; Hu, S.; Chen, P.-P.; Maiti, P.; Teter, B.; Cole, G. M.; Frautschy, S. A. *Journal of Biological Chemistry* **2013**, *288*, doi: 10.1074/jbc.M112.393751, 4056–4065.

(223) Ballatore, C.; Crowe, A.; Piscitelli, F.; James, M.; Lou, K.; Rossidivito, G.; Yao, Y.; Trojanowski, J. Q.; Lee, V. M.-Y.; Brunden, K. R.; Smith, A. B. *Bioorganic Medicinal Chemistry* **2012**, *20*, doi: https://doi.org/10.1016/j.bmc.2012.05.027, 4451–4461.

(224) Li, J.-F.; Li, C.-Y.; Aroca, R. F. *Chemical Society Reviews* **2017**, *46*, doi: 10.1039/C7CS00169J, 3962–3979.

(225) Lakowicz, J. R. *Analytical Biochemistry* **2005**, *337*, doi: 10.1016/j.ab.2004.11.026, 171–194.

(226) Asian, K.; Lakowicz, J. R.; Szmacinski, H.; Geddes, C. D. *Journal of Fluorescence* **2004**, *14*, doi: 10.1023/B:JOFL.0000047217.74943.5c, 677–679.

(227) Härtling, T.; Reichenbach, P.; Eng, L. M. *Optics Express* **2007**, *15*, doi: 10.1364/oe.15.012806, 12806.

(228) Chen, Y.; Munechika, K.; Ginger, D. S. *Nano Letters* **2007**, *7*, doi: 10.1021/nl062795z, 690–696.

(229) Habteyes, T. G. *The Journal of Physical Chemistry C* **2014**, *118*, doi: 10.1021/jp501007a, 9119–9127.

(230) Miranda, B.; Chu, K.-Y.; Maffettone, P. L.; Shen, A. Q.; Funari, R. *ACS Applied Nano Materials* **2020**, *3*, doi: 10.1021/acsanm.0c02388, 10470–10478.

(231) Bauch, M.; Toma, K.; Toma, M.; Zhang, Q.; Dostalek, J. *Plasmonics* **2014**, *9*, doi: 10.1007/s11468-013-9660-5, 781–799.

(232) Paulo, P. M. R.; Zijlstra, P.; Orrit, M.; Garcia-Fernandez, E.; Pace, T. C. S.; Viana, A. S.; Costa, S. M. B. *Langmuir* **2017**, *33*, doi: 10.1021/acs.langmuir.7b00422, 6503–6510.

(233) Schulz, F; Friedrich, W; Hoppe, K; Vossmeyer, T; Weller, H; Lange, H *Nanoscale* **2016**, *8*, doi: 10.1039/C6NR00607H, 7296–7308.

(234) Wei, G.; Yu, J.; Wang, J.; Gu, P.; Birch, D. J.; Chen, Y. *Journal of Biomedical Optics* **2016**, *21*, doi: 10.1117/1.JBO.21.9.097001, 097001.

(235) Pal, S.; Deng, Z.; Wang, H.; Zou, S.; Liu, Y.; Yan, H. *Journal of the American Chemical Society* **2011**, *133*, doi: 10.1021/ja207898r, 17606–17609.

(236) Zhang, X.; Servos, M. R.; Liu, J. *Journal of the American Chemical Society* **2012**, *134*, doi: 10.1021/ja3014055, 7266–7269.

(237) Shi, D.; Song, C.; Jiang, Q.; Wang, Z.-G.; Ding, B. *Chemical Communications* **2013**, *49*, doi: 10.1039/C3CC39093D, 2533–2535.

(238) Du, X.; Lin, W.-C.; Shou, Q.; Liang, X.; Liu, H. *Colloid and Polymer Science* **2019**, *297*, doi: 10.1007/s00396-019-04511-8, 891–902.

(239) Shi, X.; Perry, H. L.; Wilton-Ely, J. D. E. T. *Nanotheranostics* **2021**, *5*, doi: 10.7150/ntno.56432, 155–165.

(240) Scarabelli, L.; Sánchez-Iglesias, A.; Pérez-Juste, J.; Liz-Marzán, L. M. *The Journal of Physical Chemistry Letters* **2015**, *6*, doi: 10.1021/acs.jpclett.5b02123, 4270–4279.

(241) He, J.; He, Y.; Wu, X.; Zhang, X.; Hu, R.; Tang, B. Z.; Xu, Q.-H. *ACS Applied Bio Materials* **2023**, doi: 10.1021/acsabm.3c00132, DOI: `10.1021/acsabm.3c00132`.

(242) Ke, X.; Wang, D.; Chen, C.; Yang, A.; Han, Y.; Ren, L.; Li, D.; Wang, H. *Nanoscale Research Letters* **2014**, *9*, doi: 10.1186/1556-276X-9-666, 666.

(243) Wang, G.; Akiyama, Y.; Kanayama, N.; Takarada, T.; Maeda, M. *Small* **2017**, *13*, doi: https://doi.org/10.1002/smll.201702137, 1702137.

(244) Botequim, D.; Silva, I. I. R.; Serra, S. G.; Melo, E. P.; Prazeres, D. M. F.; Costa, S. M. B.; Paulo, P. M. R. *Nanoscale* **2020**, *12*, doi: 10.1039/D0NR00267D, 6334–6345.

(245) Zhu, Z.; Yuan, P.; Li, S.; Garai, M.; Hong, M.; Xu, Q.-H. *ACS Applied Bio Materials* **2018**, *1*, doi: 10.1021/acsabm.8b00032, 118–124.

(246) Zhang, Z.; Lin, M. *RSC Advances* **2014**, *4*, doi: 10.1039/C3RA48061E, 17760–17767.

(247) Shi, X.; Li, D.; Xie, J.; Wang, S.; Wu, Z.; Chen, H. *Chinese Science Bulletin* **2012**, *57*, doi: 10.1007/s11434-011-4741-3, 1109–1115.

(248) Dominguez-Medina, S.; McDonough, S.; Swanglap, P.; Landes, C. F.; Link, S. *Langmuir* **2012**, *28*, doi: 10.1021/la3005213, 9131–9139.

(249) Tong, L.; Wei, Q.; Wei, A.; Cheng, J.-X. *Photochemistry and Photobiology* **2009**, *85*, doi: https://doi.org/10.1111/j.1751-1097.2008.00507.x, 21–32.

(250) Klein, I. A. et al. *Science* **2020**, *368*, doi: 10.1126/science.aaz4427, 1386–1392.